

MEMS Energy Harvesters with a Wide Bandwidth for Low Frequency Vibrations

A Dissertation Presented to
The Faculty of the Graduate School
At the University of Missouri

by

Nuh Sadi YUKSEK

Dr. Mahmoud Almasri, Dissertation Supervisor

May 2015

The undersigned, appointed by the dean of the Graduate School,
have examined the dissertation entitled

MEMS ENERGY HARVESTERS WITH A WIDE BANDWIDTH FOR LOW
FREQUENCY VIBRATIONS

Presented by Nuh Sadi Yuksek

A candidate for the degree of

Doctor of Philosophy

And hereby certify that, in their opinion, it is worthy of acceptance.

Dr. Mahmoud Almasri

Dr. Zaichun Feng

Dr. Satish Nair

Dr. Naz Islam

To Zuleyha Yüksek

my wife, my love

To “kuzum” Burak Sami and “kızım” Pelin Nazlı

To my mother Akkız Yüksek and my father Sami Yüksek

and

To my grandmother Fahriye...

ACKNOWLEDGEMENTS

I'd like to thank my PhD advisor, Dr. Mahmoud Almasri, for giving me the opportunity to work in his research group, and for providing me with continuous guidance, constructive feedback, support and encouragement to complete this dissertation. I am grateful to Dr. Zaichun Feng for sharing his ideas with me and his technical help. I would like to extend my thanks to my colleagues Jie Lin, Jianxiong Zhu, Muhammad Hai and Shibajyoti Gosh Dastider for their help during my research. I would specially like to thank Cevher Ak, Dr. Ali Yildiz and Dr. Kemal Izci for their help and support during this research.

I take this opportunity to thank my committee members Dr. Mahmoud Almasri, Dr. Zaichun Feng, Dr. Satish Nair and Dr. Naz Islam for their time and consideration in reading my dissertation and for their help in defining and completing my dissertation.

I specially want to thank my wife Zuleyha Yuksek for her continuous support and encouragement and for the sacrifices she made and the unconditional love. I would not be able to finish my dissertation without her.

Lastly I would like to thank my father and my mother and my extended family for their encouragement, advice, love and support throughout my life.

TABLE OF CONTENTS

ACKNOWLEDGEMENTS.....	ii
LIST OF FIGURES	v
LIST OF TABLES.....	xiii
ABSTRACT.....	xiv
CHAPTER 1 INTRODUCTION	1
1.1 Vibration Energy Harvesters.....	1
1.2 Broadband Vibration Energy Harvesters	12
1.3 Low Frequency Vibration Energy Harvesters	16
CHAPTER 2 DEVICE DESIGN AND MODELING	19
2.1 Parallel Plate Power Harvester Design and Modeling.....	19
2.2 Finite Element Modeling of the Movable Capacitive Plate.....	23
2.2.1 Frequency Analysis.....	23
2.2.2 Capacitance Analysis	26
2.2.3 Squeeze Film Damping.....	28
2.3 Broadband Electrostatic MEMS Power Harvester Design	29
2.3.1 Device Design	31
2.3.2 Device Modeling.....	32
2.3.3 Simulation Results	34
2.4 Dual-Cavity for Power Harvesting	36
2.4.1 Device Design	36
2.4.2 Lumped Element Model.....	38
2.4.3 Numerical Solutions.....	40
2.5 Broadband Electromagnetic MEMS Power Harvester Design.....	42

2.5.1 Theory	42
2.5.2 Device Design	44
2.5.3 Device Modeling.....	46
2.5.4 Simulation Results	48
CHAPTER 3 DEVICE FABRICATION	50
3.1 Fabrication Procedures and Materials.....	50
3.1.1 Microfabrication	50
3.1.2 Materials	60
3.2 Fabrication Process of MEMS Capacitors	62
3.2.1 Mask Fabrication	62
3.2.2 Device Fabrication.....	65
3.2.3 Mask Fabrication for Glass Substrate	76
3.2.4 Device Fabrication on Glass Substrate	78
CHAPTER 4 DEVICE CHARACTERIZATION AND DISCUSSIONS	87
4.1 Mechanical Testing of the Fabricated Single Cavity Power Harvester	87
4.2 Electrical Testing of the Fabricated Single Cavity Power Harvester	89
4.2.1 MEMS Power Harvesting Device Characterization	89
4.2.2 Broadband Low Frequency Electrostatic Device Characterization	96
4.2.3 Broadband Low Frequency Electromagnetic Device Characterization.....	101
CHAPTER 5 CONCLUSION	105
REFERENCES	108
LIST OF PUBLICATIONS	116
VITA.....	118

LIST OF FIGURES

Figure 1.1. Autonomous wireless sensor networks provide better structural health monitoring smart structures and buildings (image from “ http://www.economist.com/node/17647603 ”).....	2
Figure 1.2. Schematics of a piezoelectric power harvester.....	3
Figure 1.3. Schematics of an electromagnetic power harvester.....	4
Figure 1.4. Schematics of three different electrostatic power harvester designs; a) in plane overlapping area, b) in plane closing gap and c) out-of-plane closing gap.....	4
Figure 1.5. Circuit design of the electrostatic power harvester from a living body [19].	5
Figure 1.6. Fundamental structure (a) and stacking method (b) of the honeycomb variable capacitor [19].	6
Figure 1.7. The cross section and dimensions of the micro engineered capacitor for power generation [20].	7
Figure 1.8. The working principle of the voltage converter [21]. The capacitor is charged when the plate separation is maximum and it is discharged when the capacitance is minimum.	7
Figure 1.9. 3-D model of the proposed energy harvester with a) comb configuration and b) proof mass configuration [22]. The overlapping area changes between the electrodes.	8
Figure 1.10. SEM images of vibration to electricity converter for in plane vibrations [23].	9
Figure 1.11. Magnified view of the transducer structure mentioned in [26]. The inset shows detailed view of the fingers.....	10
Figure 1.12. Close-up view of the spring design, the capacitor and the impact area in the fabricated device [27] for wideband excitation with power-extracting end-stops.....	11
Figure 1.13 Global schematics top view of the structure and detail of the multi-gap geometrical interface between moving and fixed comb fingers [38].	11
Figure 1.14. Schematic of the resonance frequency tunable energy harvesting device [43]	13

Figure 1.15. Photograph of a wide-band electromagnetic generator with multiple cantilever beams to cover a wider frequency range discussed in [47].....	13
Figure 1.16. 3-D diagram of the piezoelectric wide-bandwidth micro-generator described in [53].	14
Figure 1.17. 3D model of the electromagnetic power harvesting device with rotary magnetic springs in order to achieve a nonlinear structure. [54].....	15
Figure 1.18. Impact vibration energy harvester with separated driving beam and generating beams [72].....	17
Figure 1.19. Schematic view of proposed non-impact device and expected output characteristics [78].....	17
Figure 2.1 Design of the variable MEMS capacitor with variable gap. The capacitance of the device increases when the plate moves down.	20
Figure 2.2 A charge-voltage relation of the variable capacitor for energy harvesting showing the charge-constrained and voltage constrained cycles [5].....	20
Figure 2.3. 3D model of the variable MEMS capacitor with metallic moving plate and Au fixed plate on the substrate. The movable plate, suspension beams and anchors are made of electroplated Ni. The fixed electrodes and traces along with contact pads are designed as Au thin film. Stoppers on the fixed electrodes are coated with SiO ₂	21
Figure 2.4. Finalized 2D model of the moving plate with release holes along with the suspension beams and anchor areas. The plate and suspension beams along with the anchors were designed to be electroplated in a single step to reduce the overall cost of fabrication.....	22
Figure 2.5. Meshed 3D structure with almost 100,000 mesh elements to show the accuracy of the model solved by COMSOL tool.	24
Figure 2.6. Fundamental vibration mode calculations results for different number of mesh elements in FEM model for three different plate and beam thicknesses. The consistency of results can be obtained for more than 4000 mesh elements in the model.	24

Figure 2.7. Fundamental mode of oscillations for 10 μm thick plate and beams. The motion of the plate in the fundamental mode is perpendicular to the plate.....	25
Figure 2.8. Second order (a) and third order (b) vibration modes for a 10 μm thick plate with 10 μm thick suspension beams. Rocking motion is observed at these frequencies.	25
Figure 2.9. Resonance frequency change with respect to plate thickness for different beam thicknesses.	26
Figure 2.10. FEM model for capacitance calculations for two $2 \times 2 \text{ mm}^2$ metallic plates with an air gap.	27
Figure 2.11. FEM results compared with the parallel plate (PP) approximation for different plate separation. Fringe effects can be neglected in this geometry.....	27
Figure 2.12. Air flow during the motion of the movable plate of the variable capacitor.....	28
Figure 2.13 Frequency response of MEMS capacitor for different ambient pressure values. For higher pressures, the damping effect is larger and also resonance frequency shifts toward higher frequencies.	29
Figure 2.14 A photo of the macro-scale wideband electrostatic power harvester	30
Figure 2.15 The physical model of a low frequency oscillator in intermittent contact with a cantilever supporting a power harvesting device at the edge.....	32
Figure 2.16. Simulation of a micro-power harvester using single impact oscillator at 25 Hz.....	35
Figure 2.17. Design of the two-cavity MEMS capacitor. Both cavities form capacitors with variable gap. When the plate moves one direction, the capacitance increases for one capacitor and decreases for the other.	36
Figure 2.18. Timeline of the two-cavity device for small external forces.	37
Figure 2.19. 3D model of two-cavity MEMS capacitor for microfabrication. The movable plate, suspension beams and anchors are made of electroplated Ni. The fixed electrodes and traces along with contact pads are designed as Au thin film. Stoppers on the fixed electrodes are coated with SiO_2	38

Figure 2.20. Model of the variable two cavity MEMS capacitor with all forces acting on the plate.	39
Figure 2.21. Circuit model for power harvesting from a two cavity MEMS capacitor.	39
Figure 2.22. Numerical solution of the power harvesting circuit for transient behavior of the metallic plate and the corresponding output voltage and capacitance values.	41
Figure 2.23. Average current harvested from a variable cavity harvester versus external vibration for single and dual cavity devices.	41
Figure 2.24. Magnetic field profile near a rectangular permanent magnet.	43
Figure 2.25. A photo of the electromagnetic power harvester.	45
Figure 2.26. The physical model of a low frequency oscillator in intermittent contact with a cantilever supporting a coil at the edge.	46
Figure 2.27. Simulation of a macro-power harvester using single impact oscillator at 15 Hz. The average power was 15.28 μ W at 210 Hz and 1 g excitation.	49
Figure 3.1. Schematics showing the photolithography processes for positive and negative photoresist.	51
Figure 3.2. Circuit and details of a DC Sputtering system.	52
Figure 3.3. The sputtering deposition system and schematics of the chamber and gun locations.	53
Figure 3.4. RF magnetron sputtering chamber geometry and main components: 1-water cooling line, 2-substrate heater, 3-substrate, 4-target, 5-permanent magnets, 6-shield, 7-insulator, 8- RF cable, 9-thermocouple, 10-gas inlet and 11-vacuum system [85].	54
Figure 3.5. The RF sputtering deposition system and schematics of the chamber and gun locations.	55
Figure 3.6. Ni electroplating setup in a Nickel Sulfamate solution.	56
Figure 3.7. Schematics of general process of electroplating.	56
Figure 3.8. Schematics of general process of etching.	57

Figure 3.9. Circuit and schematics of the RIE chamber. The substrate holder is water cooled.....	58
Figure 3.10. Oxford Plasmalab 80 Plus Reactive Ion Etching (RIE) system.....	58
Figure 3.11. Schematics of general process of lift-off. A photoresist layer is spin coated and patterned on the substrate and then the thin film is deposited on the substrate. When the photoresist is removed in a solvent, the unwanted thin film is lifted off by the solution.	60
Figure 3.12. AZ P4620 photoresist film thickness vs. spin speed curve [86].....	61
Figure 3.13. a) The layout of Mask I for stoppers and anchor bases of the bottom cavity b) the layout of Mask II for bottom electrodes, bonding pads and anchor bases. c) The layout of Mask III for anchor holes, d) the layout of Mask IV for the capacitive plates and suspension beams....	63
Figure 3.14. Schematics of the variable capacitor fabrication process on Si substrate by surface micromachining.	66
Figure 3.15. Magnified view of the substrate after oxidation.	68
Figure 3.16. Magnified view of the substrate after gold patterning.....	68
Figure 3.17. An optical image of the photoresist mold for the anchors before hard baking.....	69
Figure 3.18. An optical image of the photoresist mold for the anchors after hard baking.....	70
Figure 3.19. An optical image of the second photoresist mold patterned on the second seed layer.	71
Figure 3.20. An optical image of the device a) after removing the second photoresist mold and b) after removing the Au layer. Cr layer is still noticeable under the Ni structure.	71
Figure 3.21. a) A Photo of the full wafer after fabrication and b) an optical microscope image of the device after removing the photoresist sacrificial layer.....	72
Figure 3.22. The SEM micrographs of MEMS capacitor with the lower cavity part, a) full device, b) magnified view of the movable plate side, c) anchor and suspension beams.	73
Figure 3.23. Side view schematics of the top cavity fabrication process for Si substrate.	74

Figure 3.24. Photo of the experimental setup to bond the two substrates together to form the two cavity MEMS device.....	75
Figure 3.25. A Schematic of the bonding process to form the two cavity MEMS power harvester.	76
Figure 3.26. An SEM micrograph of two cavity device after bonding. Isometric view SEM micrographs is taken to show the two cavities. The inset shows the front view of the device.	76
Figure 3.27. a) The layout of Mask I for bottom electrodes, bonding pads and anchor bases, b) The layout of Mask II for dielectric layer. c) the layout of Mask III for anchor holes, d) the layout of Mask IV for plates and suspension beams.....	77
Figure 3.28. Schematics of the MEMS variable capacitor fabrication process on a glass substrate.	79
Figure 3.29. An optical image of the substrate a) after developing photoresist b) after gold etching.	80
Figure 3.30. An optical image of the substrate after etching Cr and Au layers.	80
Figure 3.31. An optical image and 3D drawing of the substrate after developing NR-9 3000 PY photoresist layer. Photoresist is everywhere except the plate area.	81
Figure 3.32. An optical image of the device area after lift-off process and 3D drawing of the device at this stage.	82
Figure 3.33. An optical image of the photoresist mold for the anchors and 3D drawing of the device at this stage.	82
Figure 3.34. An optical image with a magnified view of the anchor area after Cr/Au deposition on the cured first mold and 3D drawing of the device at this stage.	83
Figure 3.35 An optical image of the second mold on top of the second seed layer defining suspension beams, plate with holes and anchors and 3D drawing of the device at this stage.	83
Figure 3.36. Optical image of the magnified view of the electroplated Ni into the device mold on top of the second seed layer and 3D drawing of the device at this stage.	84

Figure 3.37. Optical image of the magnified view of the device a) after removing Au layer, after this step, Cr layer is still covering the photoresist mold b) device after removing the Cr layer. After this step, bottom electrode and trace lines can be seen through transparent photoresist layer.	84
Figure 3.38. SEM micrographs of MEMS capacitor fabricated on glass substrate, a) full device, b) magnified view of the movable plate side, and c) anchor and suspension beams.	85
Figure 3.39. Optical images of one die with four suspended capacitive plates after dicing the substrate.	85
Figure 4.1. Mechanical testing setup: MEMS capacitor was placed on the shaker driven by a sine wave generator. The shaker was placed under a large working distance microscope. Digital camera on the microscope was connected to a PC.....	88
Figure 4.2. Overlay image of the moving plate side view under different excitation frequencies a) far from b) near the resonance frequency of the suspended plate. Plate motion can be clearly observed on the overlay images for different amplitudes.	88
Figure 4.3. Plate displacement values for different excitation frequencies.	89
Figure 4.4. Electrical testing setup: MEMS capacitor was placed on the shaker driven by a sine wave generator. The electrodes were connected to the testing circuit. The oscilloscope and spectrum analyzer were connected to a PC via GPIB ports.....	90
Figure 4.5. Measured capacitance values for different gaps. The solid curve represents theoretical fit for parallel plate approximation with a parasitic capacitance of 1.78 pF.....	90
Figure 4.6. The resulting electrical circuit after combining the parasitic capacitance and load resistor for output voltage measurements.	91
Figure 4.7. Frequency response of the moving plate measured in the electrical domain.	92
Figure 4.8. Transient behavior of the output voltage for different bias voltages from the variable capacitor for a constant shaking force.....	93
Figure 4.9. The RMS output power from the broadband electrostatic power harvester versus load resistor under 8V, 16V and 20V bias voltages.....	93

Figure 4.10. Frequency response of the moving plate measured in the electrical domain for different excitation accelerations.	95
Figure 4.11. Frequency response of the MEMS device for different bias voltages.	95
Figure 4.12. Output power for different excitation amplitudes at the resonance frequency	96
Figure 4.13. The RMS output power from the broadband electrostatic power harvester versus load resistor under 8V, 16V and 20V bias voltages.	97
Figure 4.14. Typical spectra of the output power at the resonance frequency of the high frequency cantilever.	98
Figure 4.15. Time domain plot of the output voltage across the load resistor.	99
Figure 4.16. Time domain plot of the high frequency signal decay.	99
Figure 4.17. The RMS output power as a function of frequency for 0.5 g, 1 g and 2 g excitation accelerations.	100
Figure 4.18. The RMS output power of the low frequency power harvesting device versus load resistance. Maximum power can be harvested from the device across a load resistor of 20Ω.	101
Figure 4.19. Typical spectra of the output power at the resonance frequency of the high frequency cantilever measured across the load resistor using a spectrum analyzer.	102
Figure 4.20. Typical spectra of output voltage in time domain measured across the load resistor using an oscilloscope. The time interval between impacts can be observed clearly while the high frequency signal is decaying between consecutive impacts.	103
Figure 4.21. The RMS output power as a function of frequency for different excitation amplitude. The device covers the frequency range from 11 to 62 Hz at 1 g acceleration.	104
.....	

LIST OF TABLES

Table 1. Material properties of Ni used in the FEM model and calculated results a 10 μm thickness.....	23
Table 2. Dimensions and corresponding frequencies for the cantilevers used in electrostatic power harvesting device	30
Table 3. Dimensions and corresponding frequencies for the cantilevers used in electromagnetic power harvesting device	45
Table 4. The masks set used in the fabrication process of MEMS variable capacitors on Si substrate.	65
Table 5. The masks set used in the fabrication process of MEMS variable capacitors on Si substrate.	78

ABSTRACT

We have designed and built wideband electrostatic and electromagnetic power harvesters for low frequency vibrations. The harvested power, though very small, can have a profound effect on the usage of microsensors. First, the self-powered sensors will no longer require regular battery maintenance. Second, the harvested power will remain fixed even with an unstable structure or system vibration frequency. Third, the self-powered chip is a liberating technology. For example, on a circuit board, it can simplify the connection. On a commercial jet, the sensors can greatly reduce and possibly eliminate cabling.

Initially, MEMS capacitive plates for power harvesting have been designed, modeled, fabricated, and characterized. The device is an electrostatic charge-pump utilizing inertial forces from unwanted ambient vibrations. It is designed with a $2 \times 2 \text{ mm}^2$ movable metallic plate with a thickness of $10 \text{ }\mu\text{m}$ and suspended above a fixed electrode with an air gap of $10 \text{ }\mu\text{m}$ to form a variable capacitor. The suspended movable plates are supported by four straight springs that are attached to the address lines on a substrate only at the anchors' points which is made of electroplated nickel. The suspension beams are made with a width, thickness and length of $20 \text{ }\mu\text{m}$, $10 \text{ }\mu\text{m}$ and $1500 \text{ }\mu\text{m}$, respectively.

The transient behavior of the MEMS capacitive plates was numerically solved for power harvesting calculations. The approximate stiffness values and resonant frequencies of the device for different thicknesses were determined using finite element modeling. Effect of squeeze film damping on the frequency response of the device was also modeled by finite element analysis. Mechanical and electrical measurements were

performed under different frequencies of excitations. The amplitude measurements for different frequency ranges showed a good resonance behavior at atmospheric pressures. The transient analysis of the device was investigated for power harvesting purposes. Dynamical behavior of the device was analyzed in time and frequency domain for different excitation and biasing conditions. Resonance behavior of the moving plate was observed by mechanical and electrical measurements. The measured natural frequencies of several devices were between 600 to 640 Hz. These values were consistent with the finite element modeling estimations. An optimum value for the load resistor that is connected in series with the power harvester was determined to be 100 k Ω . The output power was measured across the optimum load resistor. It was found that the single cavity device can harvest almost 186 nW peak power across a 100 k Ω load resistor at 5 g acceleration. The harvested power was dependent on excitation amplitude, excitation frequency and supplied DC voltage.

The MEMS capacitive plate energy harvester was integrated with two impact oscillators for transferring energy from low frequency structural vibration with varying mechanical spectra to a vibration of a high resonance frequency cantilever. The use of the two impact oscillators not only harvested energy at low frequencies but also had demonstrated exceptionally sufficient and optimum dynamic responses to a broad frequency bandwidth between 10 Hz and 60 Hz, the bandwidth covering most residual vibrations in structures and systems, without reduction in output power.

The wideband macro-scale power harvesting device was designed with a single-cavity MEMS capacitor fixed at the free end of an aluminum (Al) cantilever clamped at one side, with a high resonance frequency of 605 Hz matched with the single-cavity

capacitor, and two cantilevers made of Al sheet with low resonance frequencies of 18 Hz and 25 Hz, each with a thick impact mass attached at its unclamped end. The low-frequency cantilevers and the high frequency cantilever were attached on the same position.

When the power harvester was subjected to a low frequency vibration, the two low frequency cantilevers responded by vibrating at low frequencies with at least one of them vibrating close to its resonance frequency, and thus their thick metallic masses made impacts with the high resonance frequency cantilever repeatedly at two different locations exciting nonlinear oscillations. This has caused the high frequency cantilever along with the MEMS capacitor to oscillate at its resonance frequency with decaying amplitude. After each impact, the absorbed energy by the two low-frequency cantilevers were transferred to the high resonance frequency cantilever and to the single-cavity MEMS capacitor, and then to the electrical domain. The devices were first characterized by sweeping the excitation frequency from 5 Hz to 50 Hz under sinusoidal excitations with a constant acceleration (0.5 g, 1g and 2 g), while the output power was measured for each excitation frequency across the load resistor. The results demonstrate that the device was able to harvest power on a wide range from 13 Hz to 39 Hz at 1g excitation. The maximum harvested power was 96.2 nW across a 100 k Ω load resistor.

We also studied a macro-scale electromagnetic power harvester with multi-impact oscillations to achieve a broad bandwidth at low frequency vibrations. The device consists of three cantilever beams with low excitation frequencies, each with an impact mass attached at its free edge and a high frequency cantilever beam with a pick-up coil fixed at the tip. The three low frequency cantilevers are designed to resonate at 12 Hz, 19

Hz and 40 Hz within the range of ambient vibration frequency. When three low-frequency cantilevers oscillate at low frequencies, their metallic masses hit the high frequency cantilever repeatedly at three locations causing it to oscillate along with the pick-up coil, relative to the permanent magnet, with a decaying amplitude at its resonance frequency. This results in a wide bandwidth response from 11-62 Hz at 1 g. A maximum output power of 23.5 μ W can be harvested at 33 Hz oscillations with 1 g acceleration across an optimum load resistor of 22 Ω .

CHAPTER 1

INTRODUCTION

This chapter presents a brief history and evolution of Microelectromechanical systems (MEMS) power harvesting devices and voltage converters. The advantages and disadvantages of different vibration power harvesting mechanisms will be discussed and compared to other energy sources.

1.1 Vibration Energy Harvesters

Batteries are used for powering most portable and wireless sensors and electronics. They become the bottleneck to take the full advantage offered by the latest innovations in electronics since they have limited energy capacity and life span, heavy, and require periodic recharging and maintenance or replacement. Research in energy harvesting from environmental mechanical vibration becomes the popular choice among other renewable sources since it is widely available.

Inertial forces are widely used in MEMS power harvesters, charge pumps and voltage step-up converters for energy conversion from unwanted ambient vibrations into electrical energy with high enough voltage level to power up wireless sensors used in construction, security, aviation and biometry. Autonomous wireless sensor networks can be achieved with vibration power harvesters for structural health monitoring in smart buildings and structures (Figure 1.1). Vibration of smart structures can be used to power the wireless sensor networks for diagnosis and earthquake response. Harvesting power is accomplished by moving a proof mass suspended within a frame using piezoelectric

[1,2], electromagnetic [3,4], or electrostatic [5,6]. Yeatman and colleagues have compared the normalized power of many inertial energy scavengers reported in literature and found that the power results do not show clear differences between the three transducer types in terms of normalized power [7]. The advantages and disadvantages of these mechanisms were comprehensively studied based upon existing prototypes reported in the literature [8-10].

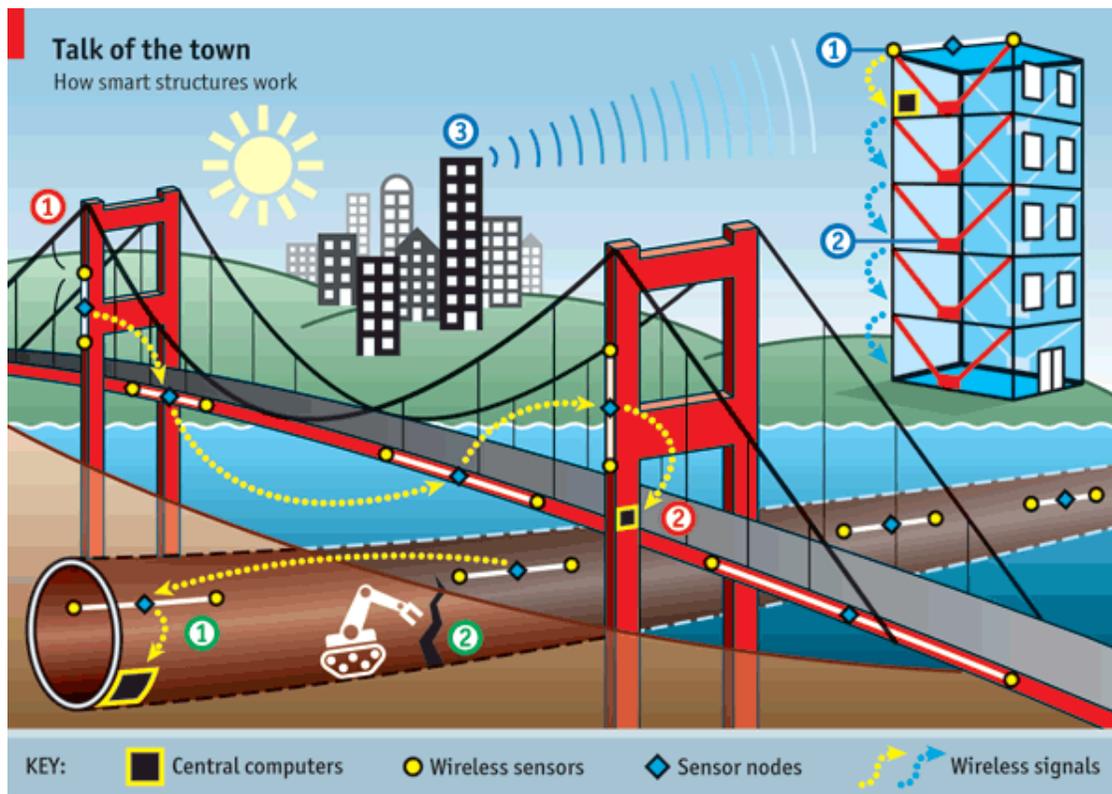


Figure 1.1. Autonomous wireless sensor networks provide better structural health monitoring smart structures and buildings (image from “<http://www.economist.com/node/17647603>”).

The piezoelectric mechanism utilizes strains caused by mechanical deflection in a piezoelectric material inducing a charge separation across the material, therefore producing a voltage (Figure 1.2). The material is usually a ceramic such as PZT in monolith or thin film form. The latter can be incorporated into a MEMS device [10].

Many of the reported piezoelectric harvesters have overcome the limitation to low frequencies applications, and have achieved reasonable high voltage levels [11-13]. However, the output impedance of the piezo element is dominated by its impedance, which is due to its small size cannot be tuned out with a realistic inductance at the frequencies of interest [10, 14].

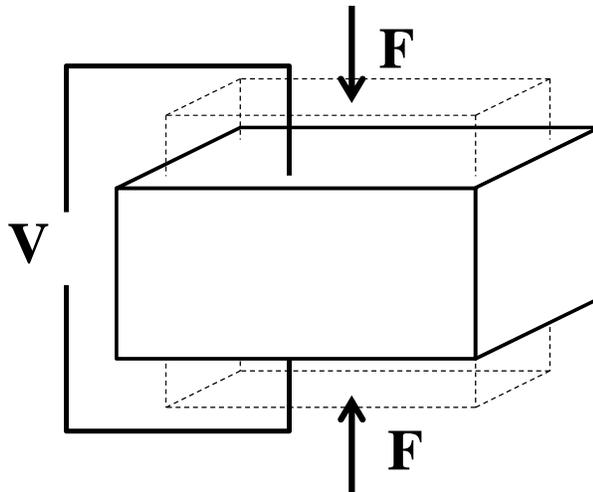


Figure 1.2. Schematics of a piezoelectric power harvester.

The electromagnetic mechanism employs a magnet moving through a coil, or a coil on a proof mass moving through the magnetic flux from a permanent magnet (Figure 1.3) [4,15,16]. Either the coil or the magnet is fixed to a frame while the other one is attached to the proof mass. The relative displacement due to the vibrations generates voltage across the coil, which is considered as electromotive force. As an example, Wang et al. reported a prototype of the energy harvester with a volume of 37.9 cm^3 , and an output peak-to-peak voltage of nearly 20 mV in average at the frequency of about 62 Hz. The generated instantaneous power across the matched load was $1.77 \text{ }\mu\text{W}$ [17]. The electromagnetic energy harvesters have high current level with low voltages. Some recent approaches have combined the piezoelectric and EM mechanisms [3,18].

The electrostatic energy harvesters are variable capacitors with one fixed and one movable by an external force. While the plate is moving, the capacitance varies between minimum and maximum values. If the charge on the plates is fixed, the voltage across the

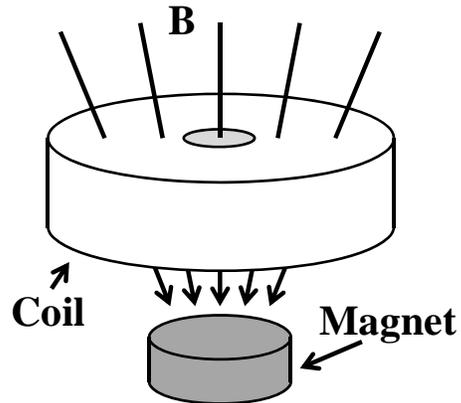


Figure 1.3. Schematics of an electromagnetic power harvester.

plates increases while the capacitance decreases. Then after certain voltage, the capacitor can be discharged to a load resistor or a charge storage device. This causes a conversion from mechanical to electrical energy. Since MEMS variable capacitors can be fabricated

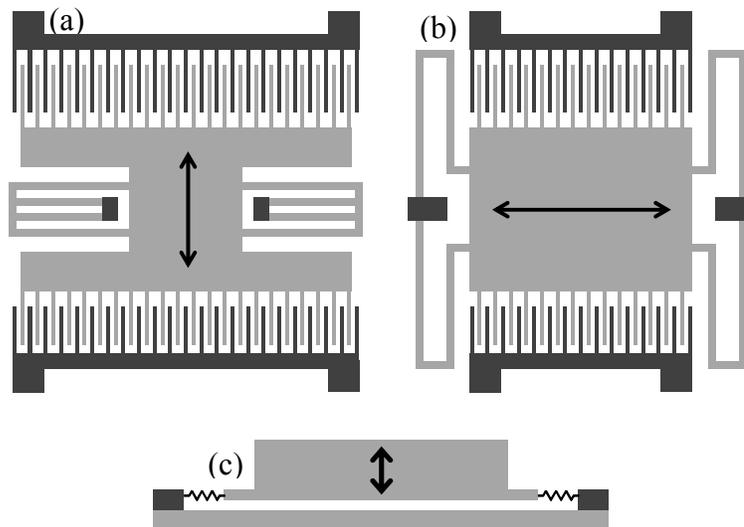


Figure 1.4. Schematics of three different electrostatic power harvester designs; a) in plane overlapping area, b) in plane closing gap and c) out-of-plane closing gap.

in a variety of dimensions, electrostatic power harvesters are good candidates for miniaturization of sources. There are three main designs of electrostatic power harvesters (Figure 1.4). Their fabrication is relatively simple and does not require installation of any external permanent magnet or any crystalline structure to generate power. It is all CMOS compatible which allows the integration of driving electronic circuits and MEMS parts on the same chip. This integration leads to the production of low cost MEMS arrays of energy sources.

In 2000, Tsuchiya's group introduced a technique to harvest power from vibration sources by using variable capacitors. The system consists of an initial charge supply, a variable capacitor, a storage capacitor and rectifying diodes to limit the current in one direction only (Figure 1.5). The proposed system was intended to be used to generate power from any motion of a living body [19]. The variable capacitor mentioned in this design was formed by folding an aluminum-evaporated polyester film repeatedly on itself.

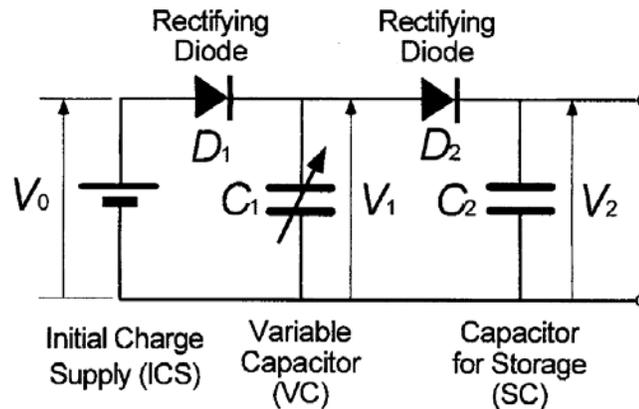


Figure 1.5. Circuit design of the electrostatic power harvester from a living body [19].

The capacitor structure is made of a 5 m long 30 mm wide polyester film with 5 μ m thickness. After folding the sheet, one layer had 20 unit capacitors (Figure 1.6). With 50 layers, 1000 unit capacitors were constructed in the structure. From the whole structure

they were able to achieve a maximum capacitance value of 200 nF. When connected to the circuit in Figure 1.5, the device was able to generate 58 μ W for a 1 M Ω load resistor from the oscillations at 4.76 Hz for the initial charge of 24 V [19].

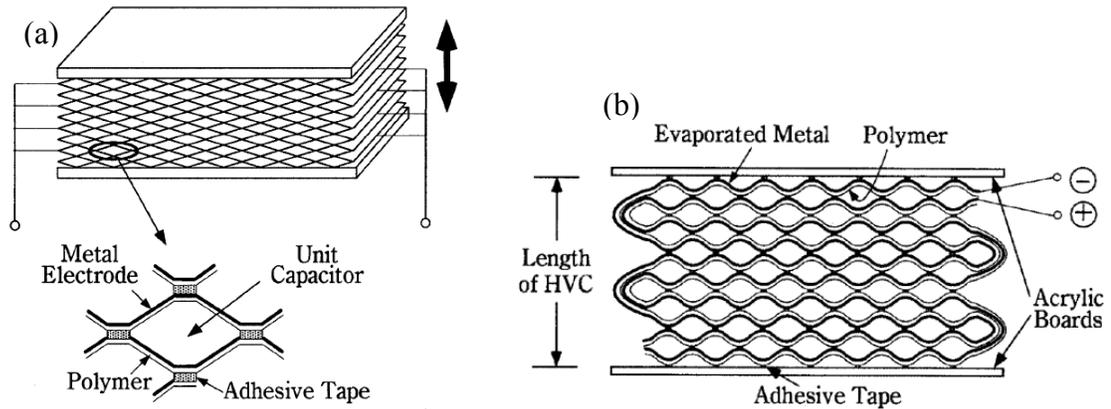


Figure 1.6. Fundamental structure (a) and stacking method (b) of the honeycomb variable capacitor [19].

Meninger et al. proposed a system to convert mechanical vibration energy to electrical energy by utilizing a variable capacitor [5]. The proposed device can be fabricated by MEMS technology. The device may consist of a $1.5 \times 0.5 \text{ cm}^2$ silicon structure etched by deep reactive ion etching (DRIE) process in a wafer of 500 μ m thickness. The whole device can fit inside a 1.5 by 1.5 mm^2 square including springs.

Miao et al. introduced the first surface micro-machined variable capacitors for power harvesting in 2003 (Figure 1.7) [20]. The device is made of a polyimide supporting membrane as a spring and a large proof mass made of Au electroplating. Thin copper (Cu) films on the substrate and on the membrane form the electrodes of the capacitor. The device is fixed inside a cavity formed by bonding a quartz substrate onto a silicon cavity. The harvested power is collected by the contacts on the Si structure at the highest point of the gap.

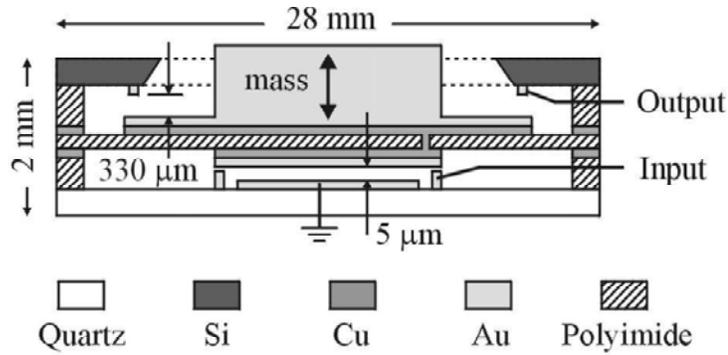


Figure 1.7. The cross section and dimensions of the micro engineered capacitor for power generation [20]

Haas et al. [21] studied the principle of a voltage converter by a micro-machined variable parallel plate capacitor combined with an electrostatic actuator (Figure 1.8). The device uses the same principle of electrostatic work done by the mechanical forces. When the capacitor is brought into the position of maximum capacitance C_{\max} it is charged to the input voltage.

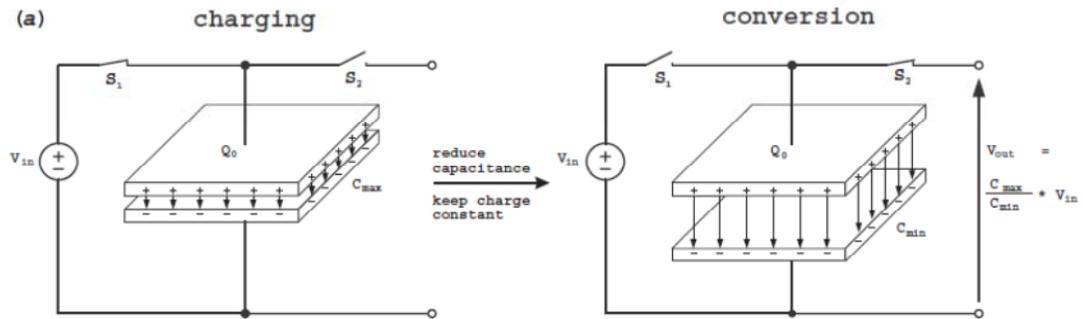


Figure 1.8. The working principle of the voltage converter [21]. The capacitor is charged when the plate separation is maximum and it is discharged when the capacitance is minimum.

To keep all the charges on both plates constant, the input switch S_1 is opened. Then, the capacitor plates are moved in the opposite direction by the actuator and the spring forces in order to decrease the capacitance from C_{\max} to C_{\min} . Since the charge on the capacitor is fixed, the voltage over the capacitor electrodes increases by the voltage

multiplication factor $M = C_{\max}/C_{\min}$ and the increased voltage can be accessed at the output via the second switch S_2 .

Lim et al. [[22]] proposed a resonant electrostatic vibration-to-electricity converter using in-plane motion with overlapping area topology (Figure 1.9). In another theoretical work, they showed that with lossless electronic components at an input voltage of 5 V, a power density as high as $59 \mu\text{W}/\text{cm}^3$ is achievable at the mechanical resonance frequency of 290 Hz [23]. In this case, they assumed that a high capacitance density, due to very small vertical gap of $1.5 \mu\text{m}$ between the top and bottom electrodes, can provide high energy conversion (Figure 1.10). The device dimensions without the bonding pads are $11 \times 6.5 \times 0.88 \text{ mm}^3$. The maximum and minimum capacitance values were reported as 181 and 47 pF respectively. The silicon substrate on the proof mass was partially removed in order to reduce the parasitic capacitance.

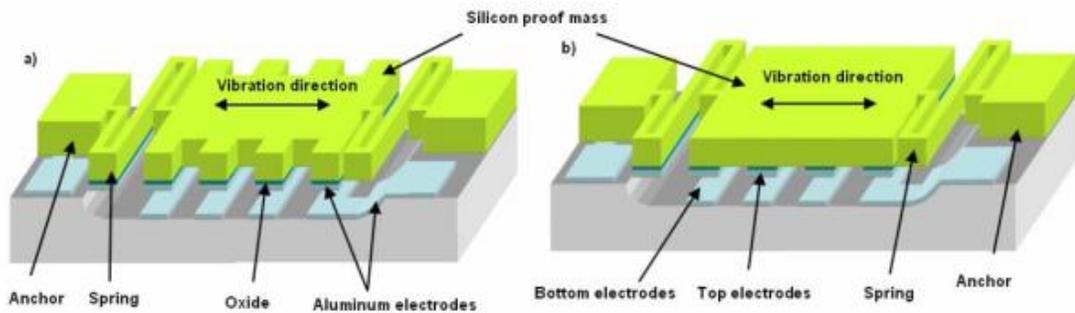


Figure 1.9. 3-D model of the proposed energy harvester with a) comb configuration and b) proof mass configuration [22]. The overlapping area changes between the electrodes.

In another work, Bourouina and colleagues demonstrated a net power conversion between 60 nW and 100 nW was generated [24] under in-plane mechanical vibrations of 250 Hz with a maximum acceleration of 0.25 g. The proof mass was measured to be displaced by $50 \mu\text{m}$ resulting in a capacitance change from 73 to 144 pF.

A macro device of variable capacitor for power harvesting from vibrations has been reported [25]. The moving plate of the variable capacitor with an area of 43.56 cm^2 is supported by eight cantilever beams with a length of 8 mm and a width of 7 mm. To complete the capacitor, a solid block of aluminum was used as the base and a piece of Mylar tape acted as a spacer to define the nominal gap between the plates. The variable macro scale capacitor provided a capacitance value of 650 pF and the structural natural frequency was found to be 1560 Hz. The experimental measurements of $1.8 \mu\text{W}$ power to a $20 \text{ M}\Omega$ resistive load at a steady-state voltage of 6 V have been demonstrated.

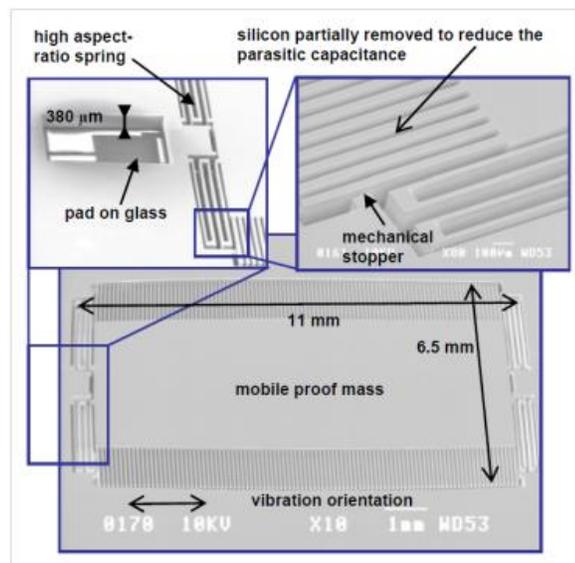


Figure 1.10. SEM images of vibration to electricity converter for in plane vibrations [23].

Hoffmann et al. [26] successfully fabricated electrostatic micro-generators with a chip size of $5 \times 6 \text{ mm}^2$ in silicon using standard MEMS fabrication processes. The fabricated micro-generator devices showed resonance frequencies between 1300 Hz and 1500 Hz. A maximum voltage of $V_{\text{rms}} = 1 \text{ V}$ and a current of $I_{\text{rms}} = 1.8 \mu\text{A}$ were generated using a bias voltage of 50 V for a 13g of harmonic excitation at resonance. A total output power of $P_{\text{rms}} = 3.5 \mu\text{W}_{\text{rms}}$ was generated through a $1.12 \text{ M}\Omega$ load. The fixed and

movable comb fingers were designed with a gap of $2.5 \mu\text{m}$ and an initial overlap of $20 \mu\text{m}$ (Figure 1.11). The active device layer was $50 \mu\text{m}$ thick and the estimated maximum variation of capacitance was 13.3 pF for each capacitor with 936 finger pairs.

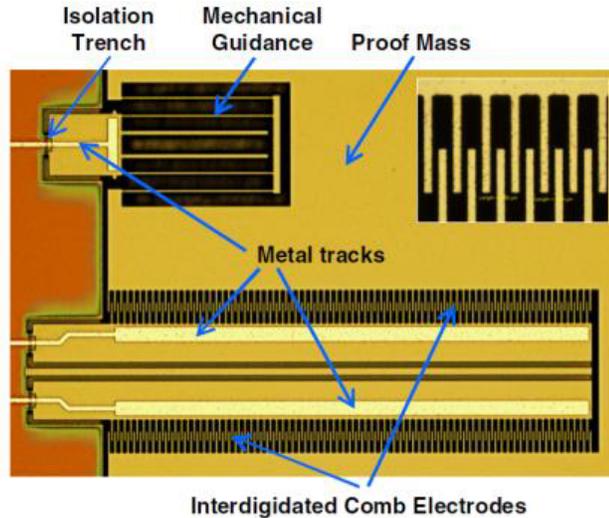


Figure 1.11. Magnified view of the transducer structure mentioned in [26]. The inset shows detailed view of the fingers.

An electrostatic energy harvester with two-stage transduction was introduced for enhancement of bandwidth and dynamic range [27]. The harvester includes a primary proof mass with two main transducers and end-stops for the proof mass functioning as secondary transducers (Figure 1.12). The device was fabricated using the SOIMUMPs process and has a total active area of $4 \times 5 \text{ mm}^2$. In comparison with a reference device made with the same die dimensions, the two-stage device showed an improvement when the maximum mass displacements of both devices reach the same limit.

Another power generator was developed by Miao et al. [28]. The device was designed to work in out-of-plane vibrations. The Si proof mass of the device had the dimensions of $\sim 11 \text{ mm}$, $\sim 11 \text{ mm}$ and 0.4 mm and it was prepared by DRIE. The device was defined with a minimum gap of about $6 \mu\text{m}$, providing a theoretical maximum

capacitance of ~ 180 pF. Since the device was a non resonant device, it was able to work on a wide frequency range.

The electrostatic mechanism has also been studied extensively using various designs that include interdigitated comb fingers microstructure [29] and suspended proof mass within a frame above the substrate [30, 31] for energy scavenging and voltage step-up conversion [32-35]. As an example, Suzuki et al. showed a power of $1.5 \mu\text{W}$ between 16-28 Hz using a suspended mass of $10.2 \times 11.6 \text{ mm}^2$ at 0.5 g [36, 37].

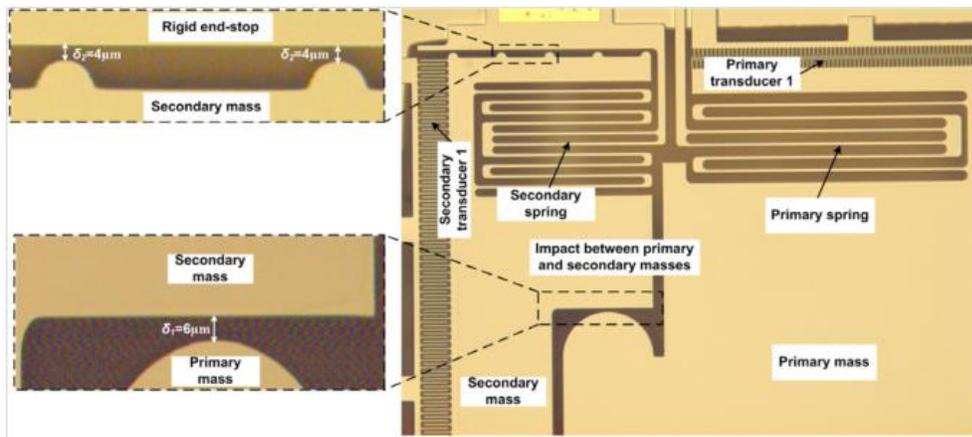


Figure 1.12. Close-up view of the spring design, the capacitor and the impact area in the fabricated device [27] for wideband excitation with power-extracting end-stops

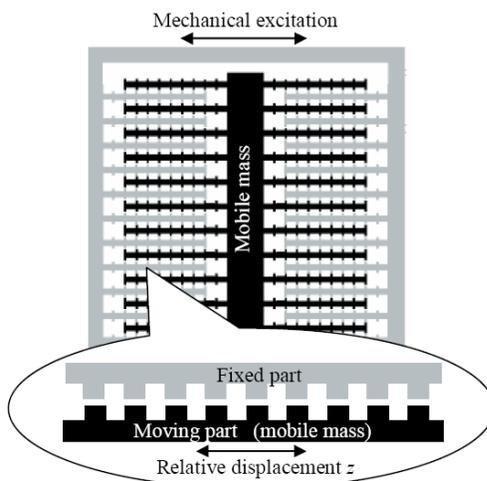


Figure 1.13 Global schematics top view of the structure and detail of the multi-gap geometrical interface between moving and fixed comb fingers [38].

Despesse et al. designed a multi gap comb finger microstructure for power harvesting (Figure 1.13). The design was able to achieve repeatable capacitance change. The calculated total capacitance was found to be varying from 48 pF to 85 pF, corresponding to an amplification factor equal to 1.8 [38]

1.2 Broadband Vibration Energy Harvesters

The majority of MEMS energy harvesters are designed to operate at resonance with narrow bandwidth [39, 40]. However, in the real environment, the vibration frequency varies with time, resulting in significant power reduction for resonance operations. Nonlinear energy harvesting devices have been shown to be capable of operating in a broader frequency range and harvesting more power than resonant devices, making them more appropriate for real life applications. To enhance the operational frequency range, researchers have employed solutions by tuning the resonance frequency to match the ambient vibration or broadening the operational bandwidth of the energy harvester [41, 42]. The resonance frequency was tuned by adjusting the stiffness of suspension beams, changing the size of the proof mass [41, 43] or by bidirectional tuning [43]. Challa et al. [43] reported a piezoelectric micro-generator, with a frequency range of 22 to 32Hz while the resonant frequency is 26Hz. The alteration was obtained by applying a magnetic force perpendicular to the cantilever beam as shown in Figure 1.14. By changing the distance between the two sets of magnets on the beam and the stationary magnets, the resonance frequency of the generator can be tuned. However, it is hard to achieve automatic tuning without using external controls, which always involve more complicated systems, require extra power to operate, and becomes unsuitable for micro device applications [44-46].

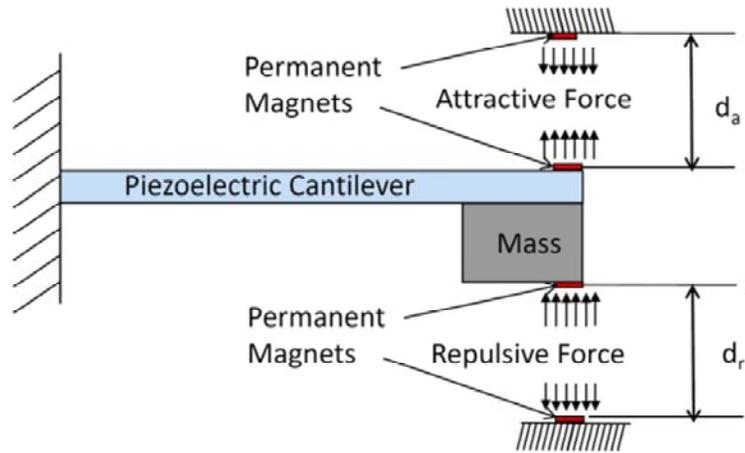


Figure 1.14. Schematic of the resonance frequency tunable energy harvesting device [43]

The bandwidth of the power harvesting devices in the literature was broadened using various techniques. Several groups have used an array of resonators with various resonant frequencies (Figure 1.15). The harvester covers a wide band of external vibration frequency by employing a number of cantilevers in different lengths resulting in an array of cantilevers with different natural frequencies. The device generates $0.4 \mu\text{W}$ of

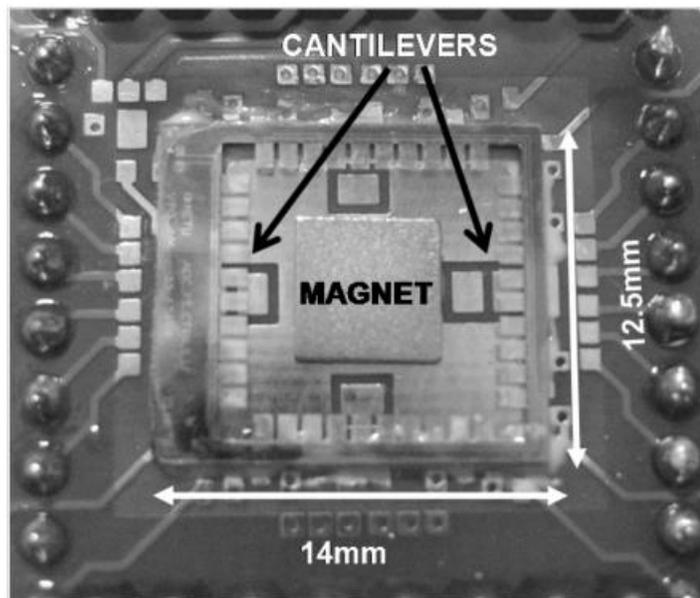


Figure 1.15. Photograph of a wide-band electromagnetic generator with multiple cantilever beams to cover a wider frequency range discussed in [47]

continuous power with 10mV voltage in an external vibration frequency range of 4.2-5 kHz, covering a band of 800 Hz. However, such an array has resulted in lower average power density than a single device because not all cantilevers respond to a specific frequency at the same time [47, 48, 55].

One group has considered two types of non-linear stiffness, a non-linear bi-stable snap-through mechanism and a hardening spring, which has the effect of shifting the resonance frequency [49]. Arrieta et al. proposed to utilize the nonlinear behavior of a bistable composite plate with bonded piezoelectric patches for broadband nonlinear energy harvesting and to enhance the performance of vibration-based energy harvesters. [50]. One group has proposed a new method based on the use of stochastic nonlinear oscillators method by applying it to piezoelectric energy harvesting from ambient vibration. [51]. Another group has constructed a bistable electromagnetic SOI energy harvester prototype [52]. A micromachined piezoelectric generator was designed to harvest mechanical energy in a wide vibration bandwidth. The size of the device is 3mm

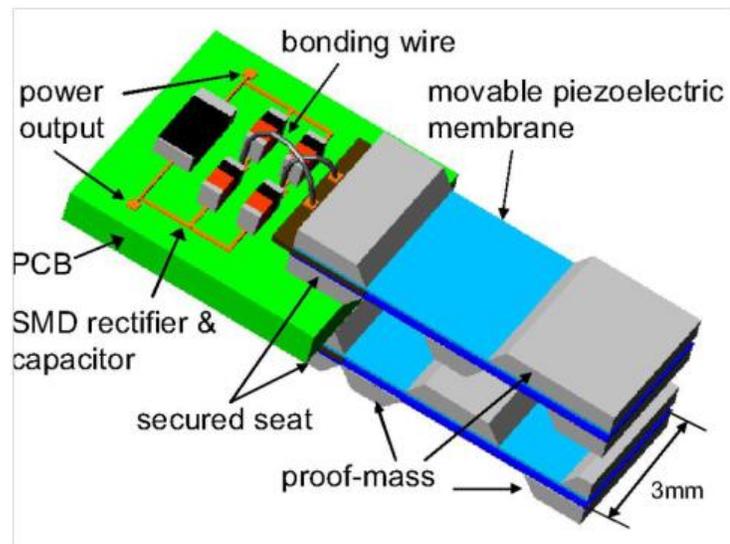


Figure 1.16. 3-D diagram of the piezoelectric wide-bandwidth micro-generator described in [53].

x 3mm x 5mm and it is composed of four connected-in-parallel cantilever structures (Figure 1.16). The designed generator was targeted at producing the power in a reasonable wide mechanical vibration range (e.g. 300-800 Hz) [53].

Spreemann et al [54] reported a tunable electromagnetic energy harvester using magnetic springs instead of a conventional spring and combined a tuning mechanism with the non-linear structure. This device was realized by a rotating suspension (Figure 1.17). The magnetic spring magnets gave rise to a nonlinear restoring force providing low resonance frequencies within a small generator volume.

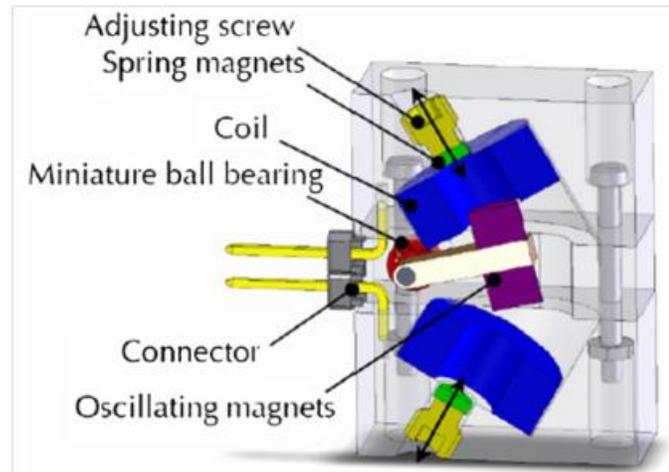


Figure 1.17. 3D model of the electromagnetic power harvesting device with rotary magnetic springs in order to achieve a nonlinear structure. [54]

Bi-stable springs have been used to harden or soften the suspensions to increase the bandwidth of the wideband MEMS electrostatic energy harvester utilizing nonlinear springs [55], electromagnetic induction energy harvesters [56], a bistable piezoelectric inertial generator [57], a wideband micro-electromechanical energy harvesters [58], a so called Smart Sand platform [59] and wideband adaptive system by employing mechanical nonlinear strain stiffening [60]

Other groups have used various impact mechanisms to broaden the bandwidth [61-63]. Moss et al. developed a device that consists of an oscillator with double-sided, symmetrical, piezoelectric bimorph-stops. The device operates in the range 100-113 Hz with 5.3 mW at 0.45 g [6]. Energy harvesting device uses magnetic levitation to produce an oscillator with a tunable resonance [63]. Piecewise linear harvesters were also investigated [64], e.g., by changing the length of a beam [65]. However, there is a possibility that the micro beam may wear out under continuous engagement with a sliding stopper.

Non-resonant energy harvesters have also been demonstrated [66]. One group reported a device that employs a spherical, unidirectional permanent magnet ball that is allowed to move arbitrarily in a spherical cavity wrapped with copper coil windings. The results showed that the device responded to a low frequency with a wideband content of human motion [67].

1.3 Low Frequency Vibration Energy Harvesters

Most energy harvesters operate at optimum near their resonance frequencies which are well above 60 Hz [68,69,[47]. The generated power drops significantly at the low frequencies. Therefore, it is necessary to investigate a device that can generate power at low frequencies from ambient vibration. To resolve this issue and increase the power harvester's efficiency, several groups have used frequency-up conversion technologies which can be divided into impact [70-77] and non-impact [78-80] techniques. A low frequency piezoelectric energy harvester based on impact vibration, presented by Gu [72], has the ability to restrict the large displacement of the driving beam by two additional

piezoelectric beam (Figure 1.18) and achieve low frequency operation. The impact vibration energy harvester achieved significant improvement of output power and power density compared to the conventional counterpart.

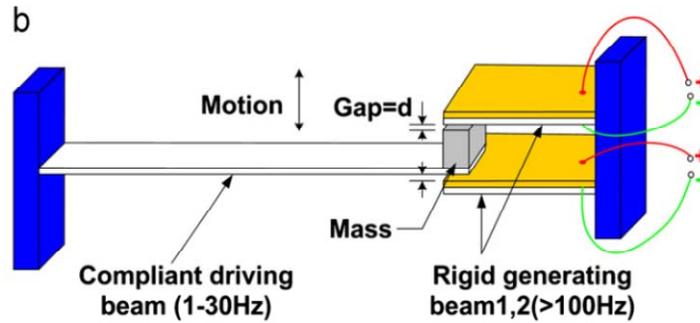


Figure 1.18. Impact vibration energy harvester with separated driving beam and generating beams [72].

The impact technique includes analysis of the generated power of a piezoelectric vibrator by the impact of a steel ball on a piezoelectric membrane [70], investigations of the impact mechanism using a moving mass on piezoelectric bending structures [71], a periodic single impact between a low frequency driving beam resonator and a single or double high frequency piezoelectric generating beam resonators [72-77]. The non-impact techniques include a snap-through buckling (Figure 1.19) energy harvester with a low

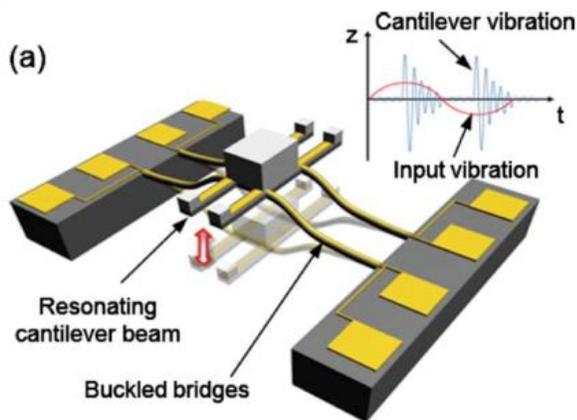


Figure 1.19. Schematic view of proposed non-impact device and expected output characteristics [78]

resonance frequency vibration to drive a few generating beams with high resonance frequency [78], an EM energy harvester using frequency up-conversion [79,80].

These techniques increased the generated power at low frequencies, but require large space and require large acceleration to drive the buckled beam. In this thesis, we will investigate novel MEMS power harvesters that use multi-impact mechanisms to achieve a wide bandwidth response from low frequency and a frequency-up conversion.

CHAPTER 2

DEVICE DESIGN AND MODELING

This chapter will present the design and modeling of low frequency broadband power harvesters. First, design of variable MEMS capacitors with single cavity and two vertical cavities will be discussed. Then, operation principle of the low frequency electrostatic power harvester with wideband response will be described in details. Theoretical background, numerical solution and modeling of electrostatic devices including finite element modeling, frequency analysis, squeeze film damping, and lumped element modeling will also be included. Finally principle of operation of the broadband low frequency electromagnetic power harvesting device will be discussed along with theoretical background and numerical simulation.

2.1 Parallel Plate Power Harvester Design and Modeling

The variable MEMS power harvester was designed using parallel plates forming a vertical capacitive cavity. The moving plate is suspended over a fixed electrode with an air gap to form the capacitor (Figure 2.1). The device was designed for out-of-plane oscillations. When the plate moves down, the capacitance of the device increases. The plate was designed with holes to reduce the squeeze film air damping and help to release the photoresist sacrificial layer during the final step of the fabrication process.

The device operates as follows to harvest power: when the plate moves downward under an external force, the capacitance becomes larger. If the device is supplied with a

voltage source, the capacitor will be charged during this phase. The charging of the capacitor will continue until the cavity reaches the minimum separation of plates. Then, when the plate moves upward by the external and loaded spring forces while keeping the charge constant, the capacitance becomes smaller and the voltage will be increased until it reaches the desired output value (Figure 2.2). After that instance the charge in the capacitor will flow towards the load circuit.

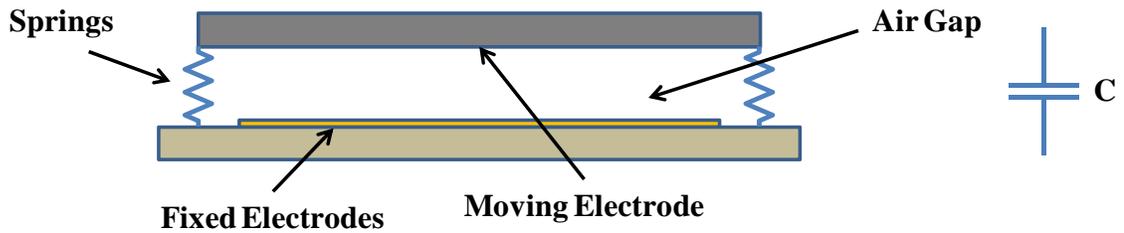


Figure 2.1 Design of the variable MEMS capacitor with variable gap. The capacitance of the device increases when the plate moves down.

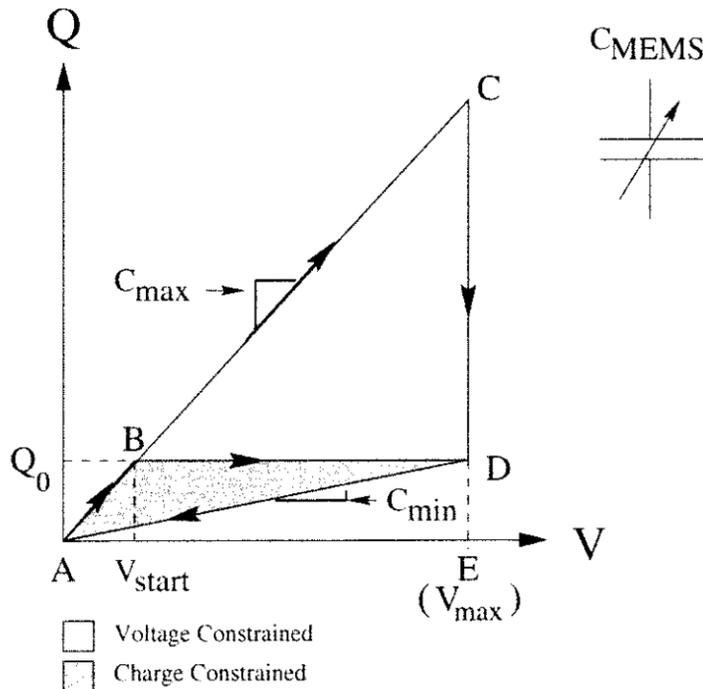


Figure 2.2 A charge-voltage relation of the variable capacitor for energy harvesting showing the charge-constrained and voltage constrained cycles [5].

Figure 2.3 shows the 3D drawing of the designed MEMS capacitor formed with metallic moving plate and Au fixed plate on the substrate. The movable plate is suspended with four suspension beams. The plate, beams and anchors are made of electroplated Ni. The fixed electrodes and traces along with contact pads are designed as Au thin film. Stoppers on the fixed electrodes are coated with SiO₂ dielectric film.

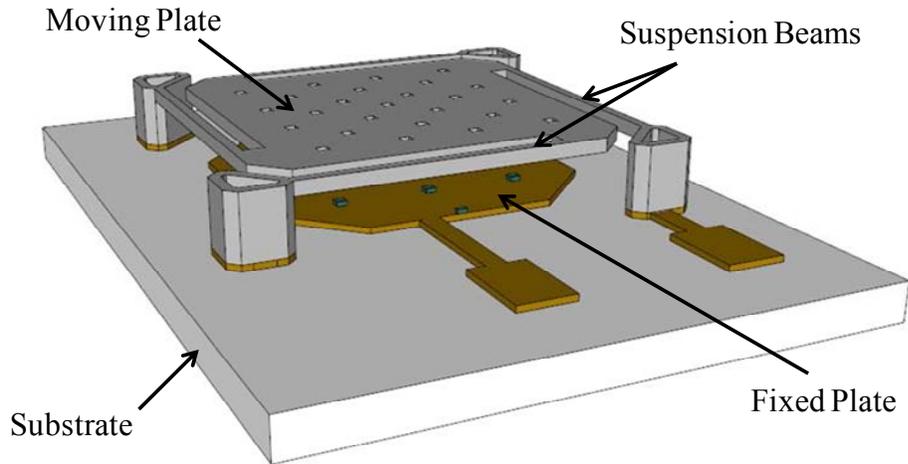


Figure 2.3. 3D model of the variable MEMS capacitor with metallic moving plate and Au fixed plate on the substrate. The movable plate, suspension beams and anchors are made of electroplated Ni. The fixed electrodes and traces along with contact pads are designed as Au thin film. Stoppers on the fixed electrodes are coated with SiO₂.

The device is designed with a $2 \times 2 \text{ mm}^2$ metallic movable plate with a reasonable thickness to achieve large mass, and 4 soft suspension beams that have a length and width of 1.5 mm, and 20 μm , respectively, in order to operate at a natural frequency close to the ambient vibration frequencies between 300 Hz and 1 kHz. The spacing between the suspension arms and the main plate is kept at 40 μm to prevent any mechanical contact between plate and arms (Figure 2.4).

The movable plate and straight suspension beams are designed with high fill factor and fabricated using electroplated Ni because it is mechanically durable material with

controllable residual stress and it is a low cost conducting film that can be fabricated with various thicknesses up to 100 μm . The plate and suspension beams along with the anchors were designed to be electroplated in a single step to reduce the overall cost of fabrication. Therefore the plate thickness and beam thicknesses were kept the same after single step electroplating.

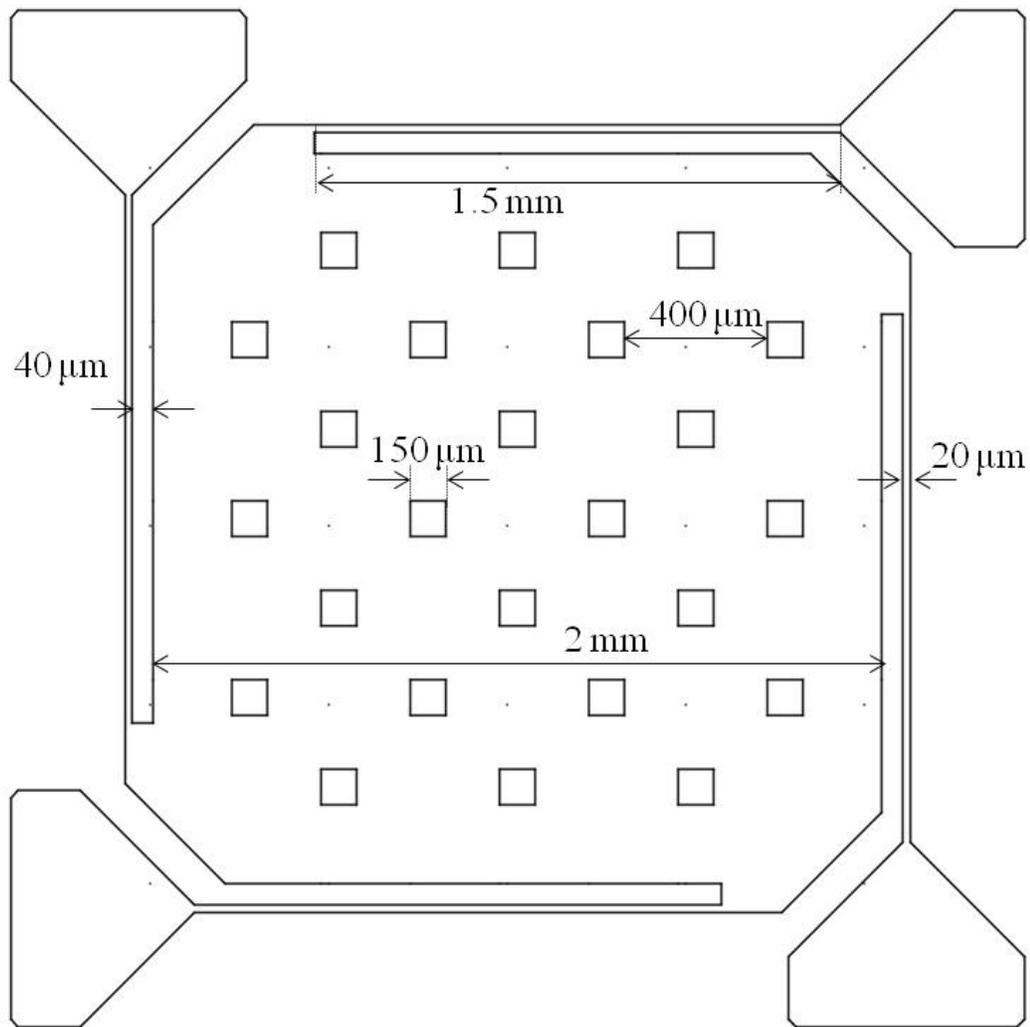


Figure 2.4. Finalized 2D model of the moving plate with release holes along with the suspension beams and anchor areas. The plate and suspension beams along with the anchors were designed to be electroplated in a single step to reduce the overall cost of fabrication.

2.2 Finite Element Modeling of the Movable Capacitive Plate

The structural properties of the designed device with movable Ni and 4 linear suspension beams were modeled using finite element method (FEM) by COMSOL multi-physics tool. The material properties of Ni that were used in the model include Young's modulus 219 GPa and Poisson's ratio 0.31 were pulled from the material library of the COMSOL tool. Also the density of the Ni was used as 8900 kg/m³. For a 10 μm thickness, the effective spring constant was calculated to be 5.41 N/m. The effective mass of the moving plate was calculated from the FEM results as 3.83×10⁻⁷ kg (Table 1).

Table 1. Material properties of Ni used in the FEM model and calculated results a 10 μm thickness.

Young's modulus	Poisson's ratio	Density	Resonance frequency	Spring constant	Effective mass
219 GPa	0.31	8900 kg/m ³	598 Hz	5.41 N/m	3.83×10 ⁻⁷ kg

2.2.1 Frequency Analysis

The model was solved to find out the natural frequency of the plate for an electroplated Ni structure. Different calculations are carried out for different mesh dimensions to minimize the calculation errors (Figure 2.5). For the whole plate, the solution with 3000 mesh elements gives a rough approximation about the natural frequency. Figure 2.6 shows that as the number of mesh elements increases, the frequency value converges to a certain value. More than 40,000 mesh elements give a more precise value.

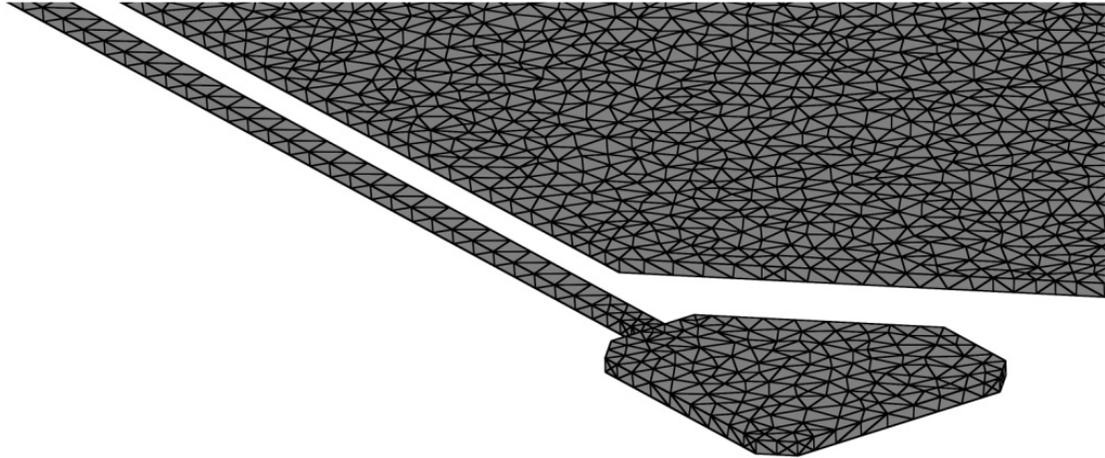


Figure 2.5. Meshed 3D structure with almost 100,000 mesh elements to show the accuracy of the model solved by COMSOL tool.

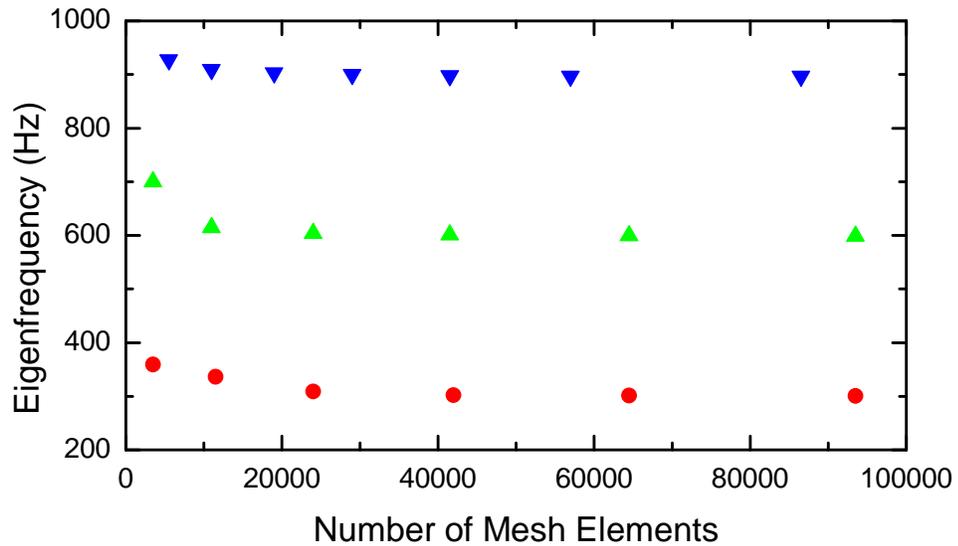


Figure 2.6. Fundamental vibration mode calculations results for different number of mesh elements in FEM model for three different plate and beam thicknesses. The consistency of results can be obtained for more than 4000 mesh elements in the model.

FEM model solution also provides higher order modes of oscillations. For the fundamental mode, the plates move up and down parallel to the base (Figure 2.7). However for the second and third order modes, the motion of the plate seems to be a rocking motion around an axis passing through the plane of the plate area (Figure 2.8).

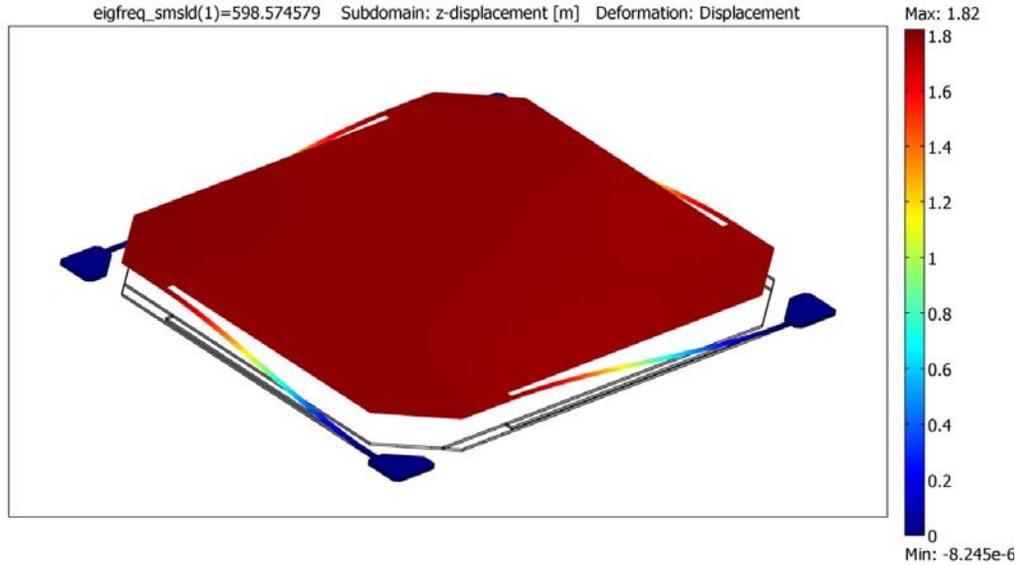


Figure 2.7. Fundamental mode of oscillations for 10 μm thick plate and beams. The motion of the plate in the fundamental mode is perpendicular to the plate.

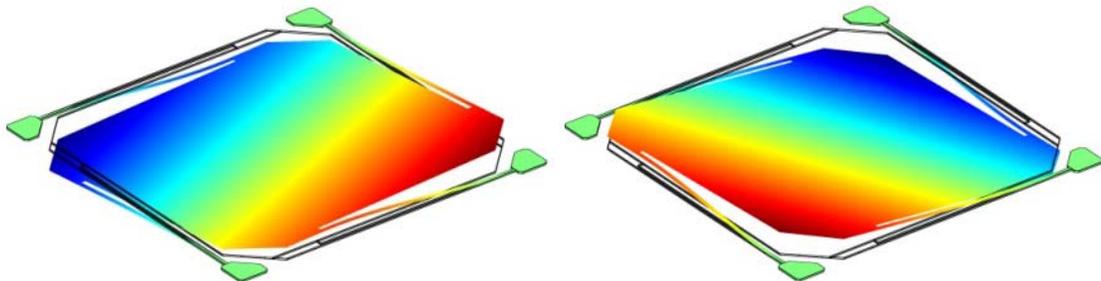


Figure 2.8. Second order (a) and third order (b) vibration modes for a 10 μm thick plate with 10 μm thick suspension beams. Rocking motion is observed at these frequencies.

To understand the effect of material thickness on the operation frequency, we simulated the FEM for different thicknesses. The results show that when the movable plate and suspension beams thicknesses are less than 15 μm , the natural frequency is less than 1 kHz (Figure 2.9). The results show a linear dependence on the thickness for the fundamental undamped mode. As the material thickness is varied within the range of 5 to 20 μm , the natural frequency of the device can be tuned from 300 Hz to 1 kHz low frequency devices are desired for frequency match with the ambient vibrations. However,

very thin structures will not be strong enough to operate as designed. Another advantage of strong plates is that after fabrication, the suspension or the release of the plate becomes a lot easier than soft structures due to their resistance against surface tension of the liquids used in the release process.

The frequency of the plate can further be reduced by growing a thicker plate after fabricating the beams. This keeps the suspension beam thickness unchanged but increase the mass of the plate. The simulation results show the change of frequency for the plate thicknesses varying between 5 to 20 μm while the beam thickness is kept at 5 and 10 μm (Figure 2.9).

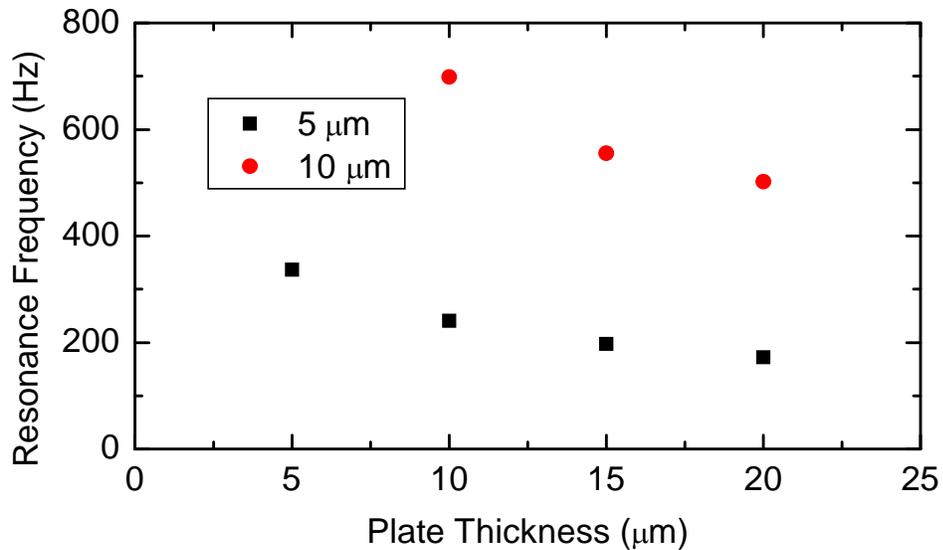


Figure 2.9. Resonance frequency change with respect to plate thickness for different beam thicknesses.

2.2.2 Capacitance Analysis

We have solved another FEM model of the device in COMSOL in order to determine the capacitance characteristics (Figure 2.10). The device is assumed to be operating with an air gap of 5 μm to 30 μm at equilibrium. In order to calculate the

capacitance of the structure, the electric field distribution between the plates and around the plates has been simulated. Figure 2.10 shows the electric potentials of the surfaces under 1 V bias. Since the device area is much more than the thickness, the electric field is

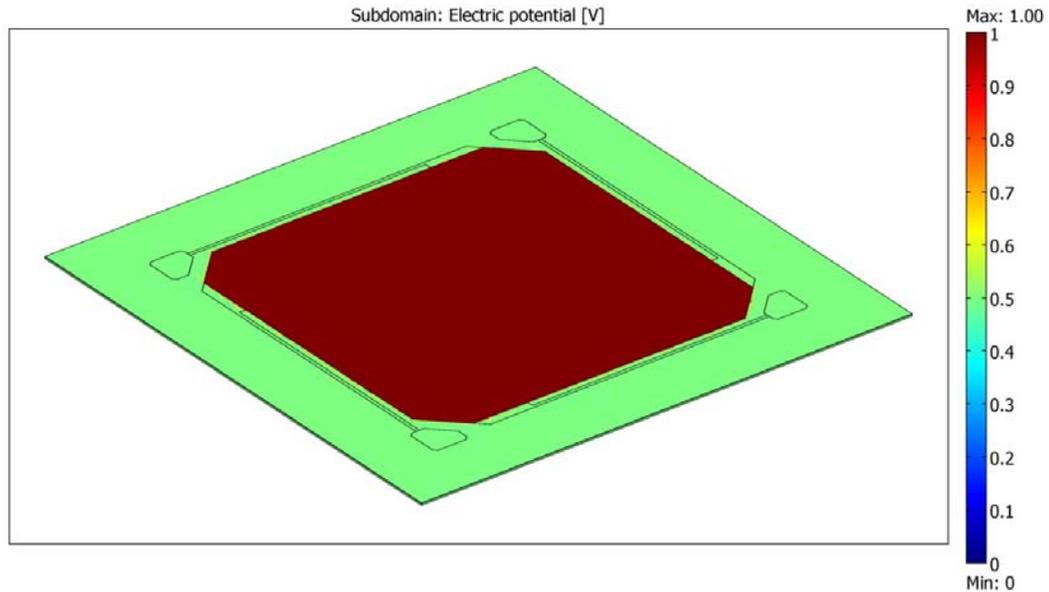


Figure 2.10. FEM model for capacitance calculations for two $2 \times 2 \text{ mm}^2$ metallic plates with an air gap.

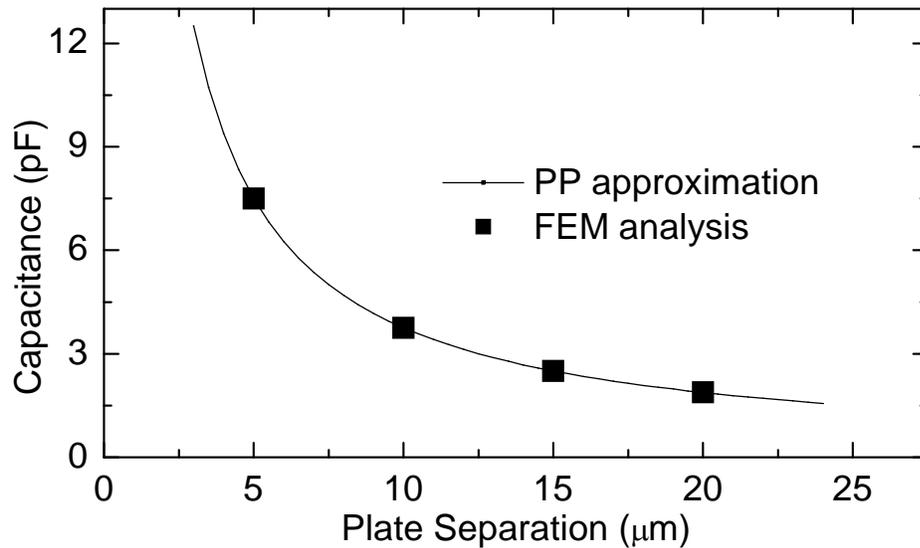


Figure 2.11. FEM results compared with the parallel plate (PP) approximation for different plate separation. Fringe effects can be neglected in this geometry.

almost uniform in between the plates and the edge effects are almost negligible. The capacitance is calculated by computing the integrated surface charge density over one electrode and the value is divided into the voltage applied. The calculated results are compared in Figure 2.11 with parallel plate capacitance calculation with the same area used in the FEM mode. The difference between the parallel plate approximation and the FEM results are less than 0.1 %. Therefore, the parallel plate approximations are used for the rest of the capacitance calculations.

2.2.3 Squeeze Film Damping

To understand the effect of amount of air between the plates on the frequency response, the FEM model for structural mechanics model has been solved along with the squeeze film damping model. During the motion of the plate, air moves in and out and causes damping to the motion (Figure 2.12). The model is simulated for 10 μm air gaps under and above the plate and the frequency is swept from 100 Hz to 10 kHz. As the pressure is decreased below atmospheric pressures, the resonance amplitude is increased. Also the maximum response frequency is shifted to lower frequencies (Figure 2.13).

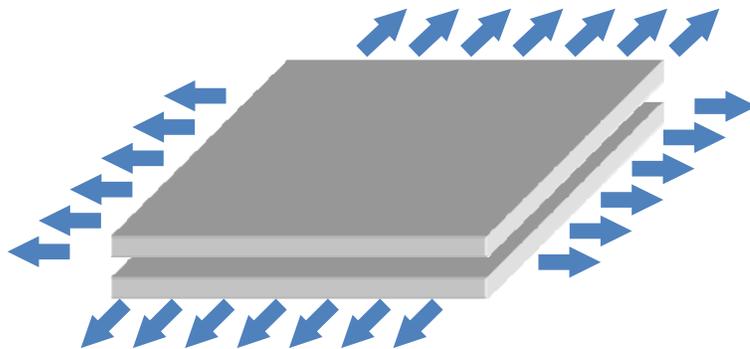


Figure 2.12. Air flow during the motion of the movable plate of the variable capacitor.

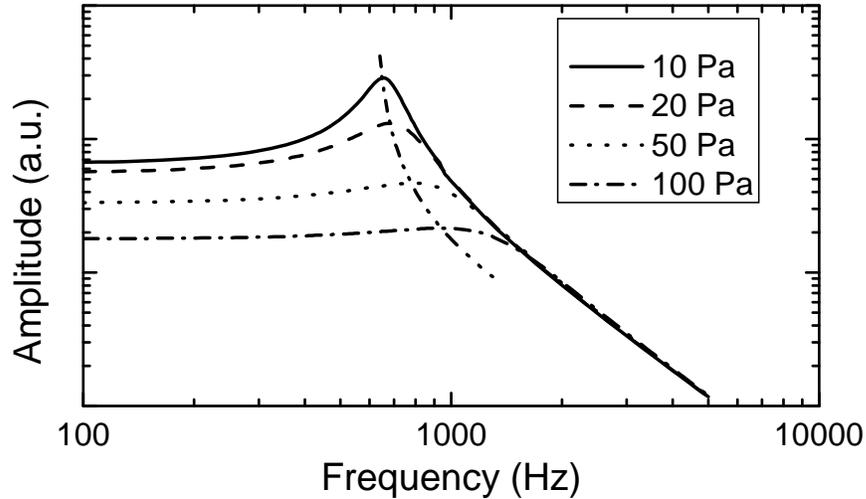


Figure 2.13 Frequency response of MEMS capacitor for different ambient pressure values. For higher pressures, the damping effect is larger and also resonance frequency shifts toward higher frequencies.

2.3 Broadband Electrostatic MEMS Power Harvester Design

We have demonstrated a novel electrostatic power harvester that uses a multi-impact mechanism to achieve a wide bandwidth response from low frequency utilizing frequency-up conversion by impact. We have designed and built a hybrid macro scale wideband electrostatic power harvester prototype for low frequency vibration (Figure 2.14). The device consists of a single-cavity MEMS capacitor fixed at the free end of an aluminum cantilever clamped at one side with a length, width and thickness of 63 mm, 13 mm, 3 mm, respectively, with a high resonance frequency of 605 Hz matched with the single-cavity capacitor, and two cantilevers with a length of 34 mm and 50 mm, width of 9.5 mm, 8 mm, and thickness of 0.5 mm, respectively, made of Al sheet vibrating at low excitation frequency, each with a thick impact mass attached at its unclamped end. The low-frequency cantilevers were attached on top of the clamped side of the high frequency cantilever (Table 2).

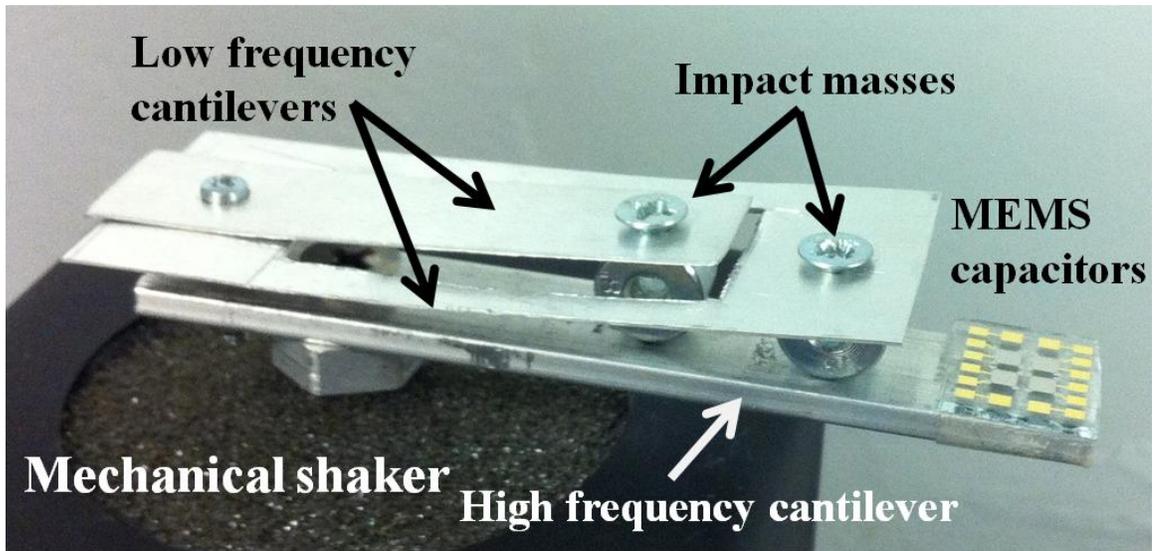


Figure 2.14 A photo of the macro-scale wideband electrostatic power harvester

Table 2. Dimensions and corresponding frequencies for the cantilevers used in electrostatic power harvesting device

	Thickness (mm)	Length (mm)	Width (mm)	Resonance Frequency (Hz)
LF cantilever 1	0.4	50	8	18
LF Cantilever 2	0.4	34	9.5	25
HF Cantilever	3	63	13	605

One of the two low frequency cantilevers on the macro device was designed to resonate at 18 Hz while the other resonates at 25 Hz within the range of ambient vibration frequency. The metallic impact masses with a weight of 4 grams, and were used in order to reduce the cantilever's resonance frequency and improve the momentum transfer to the high frequency cantilever. When the power harvester was subjected to a low frequency vibration using a mechanical shaker, the two low frequency cantilevers responded by vibrating at low frequencies with at least one of them vibrating close to its resonance frequency, and thus their thick metallic masses made impacts with the high resonance

frequency cantilever repeatedly at two locations. This has caused it along with the MEMS capacitor to oscillate with decaying amplitude at its resonance frequency. After the impact occurs, the absorbed energy by the two low-frequency cantilevers were transferred to the high resonance frequency cantilever and to the single-cavity MEMS capacitor, and then to the electrical domain.

2.3.1 Device Design

To harvest power from low frequency structural vibration, we propose mechanisms to transfer power from low frequency vibration to the high frequency vibration through impact oscillators. The proposed design (See Figure 2.14) uses oscillators with low resonance frequencies to convert the energy to a high resonance frequency power harvester through oscillations resulting from intermittent physical contacts between a low frequency oscillator and the power harvester. The main advantages are: (1) Enabling energy transfer from low frequency structural vibration to power harvester whose natural frequency lies outside the frequency ranges of typical mechanical vibration that the device is designed to harvest energy from. (2) Harvesting low frequency energy that is not restricted to the narrow band at the impact oscillator resonance frequency. Due to the nonlinearity of the impact oscillator, it has a much broader bandwidth, from its natural frequency to several times of its natural frequency. If the forcing frequency is above the natural frequency when the oscillator impacts on a stiffer structure, it results in a higher “equivalent stiffness” thus a much broader bandwidth than in the absence of impact. (3) The impact takes place between the oscillator and the elastic beam. The beam inertia is negligible.

2.3.2 Device Modeling

Physical model of the energy transfer through intermittent contact between a low frequency oscillator and a high frequency cantilever was prepared (Figure 2.15). The power harvesting device along with the cantilever mass is modeled by a mass m_2 at the tip of the cantilever. For the preliminary modeling, we ignored the degrees of freedom contained within the power harvester for our capacitive harvester. Another mass m_1 , supported by a linear spring with a spring constant k_1 , models one of the three masses supported by three different cantilevers in Figure 2.15. It is designed to have a resonance frequency in the range of low frequency vibration of a structure, between 5 Hz and 60 Hz. The suspended plate was considered as a separate mass m_3 suspended by springs with equivalent stiffness of k_3 .

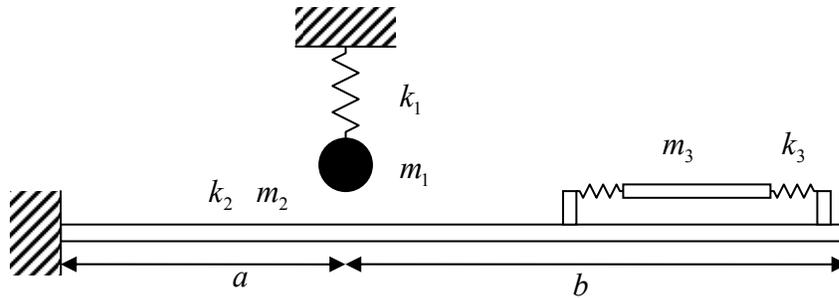


Figure 2.15 The physical model of a low frequency oscillator in intermittent contact with a cantilever supporting a power harvesting device at the edge.

Our complete system includes the linear oscillator and the long cantilever on a vibrating structure. To simplify the model, we treated the support as fixed and apply inertia forces on concentrated masses following d'Alembert's principle. We use y_1 to represent the position of the mass m_1 measured from the potential impact point of the beam. Let x_1 be the displacement of the potential impact point on the beam. Let F_1 be the

contact force acting on the mass m_1 by the cantilever. When the whole system is subjected to base excitation with acceleration of $-A\omega^2\sin(\omega t)$, the equation of motion for mass m_1 is given below:

$$m_1\ddot{x}_1 = -k_1x_1 - c_1\dot{x}_1 - m_1A\omega^2\sin(\omega t) + F_1 \quad (1)$$

The equation for the mass m_2 at the free edge of the cantilever beam is:

$$m_2\ddot{x}_2 = -c_2\dot{x}_2 - m_2A\omega^2\sin(\omega t) + F_2 \quad (2)$$

where F_2 is the total force acting on the mass by the cantilever. The forces F_1 and F_2 are calculated based on whether mass m_1 hits the cantilever. The force calculation can be done by assuming that m_1 does hit the cantilever. The coefficients c_1 and c_2 in (1) and (2) account for the energy dissipation in the impacting mass and MEMS capacitor. The damping coefficient c_2 is thus dependent on the external load resistance. Using engineering beam theory and the principle of superposition, we can directly calculate the displacements:

$$x_1 = -\frac{(F_1 + F_2)a^3}{3EI} - \frac{F_2ba^2}{2EI} \quad (3)$$

$$x_2 = x_1 + \left[-\frac{(F_1 + F_2)a^2}{2EI} - \frac{F_2ba}{EI} \right] b - \frac{F_2b^3}{3EI} \quad (4)$$

Solve the above two equations for the forces. We get

$$F_1 = -\frac{12(a+b)^3EI}{a^3b^2(3a+4b)}x_1 + \frac{6(2a+3b)EI}{ab^2(3a+4b)}x_2 \quad (5)$$

$$F_2 = \frac{6(2a+3b)EI}{ab^2(3a+4b)}x_1 - \frac{12EI}{b^2(3a+4b)}x_2 \quad (6)$$

If the contact force F_1 obtained from the above formula is negative, it implies that mass m_1 does not make contact with the cantilever. Therefore, we must have:

$$F_1 = 0 \quad \text{and} \quad F_2 = -\frac{3EI}{(a+b)^3} x_2 \quad (7)$$

Based on the design, the movable plate of the capacitor is subjected to the nonlinear electrostatic force F_e , the suspension force from springs with combined stiffness k , the damping force F_{dp} , the nonlinear stopper force F_{st} and the excitation force F_{ex} . The dynamic model equation for forces based on Newton's second law is as follows,

$$m_3 \ddot{x}_3 = -c_1 \dot{x}_3 - k_3 x_3 + F_{st} + F_e + F_{ex}. \quad (8)$$

The excitation force F_{ex} is from the motion of x_2 , thus we can get the following equations:

$$F_{ex} = m_3 \ddot{x}_2 - m_2 A \omega^2 \sin(\omega t) \quad (9)$$

2.3.3 Simulation Results

When the complete system is subjected to base excitation, the responses of the system are strongly dependent on the forcing frequency. Recall that the impact oscillator is designed to harvest low frequency vibrations. We thus assume that the base excitation frequency is much lower than the natural frequency of the cantilever but comparable with the natural frequency of the impact oscillator. A representative response is shown in Figure 2.16. The beams length, width and thickness are 17 mm, 6 mm, and 100 μm , respectively. The beam is impacted by a single slow impact oscillator with an excitation frequency near the resonance frequency of the impact oscillator. Figure 2.16 shows the period doubling

phenomenon when the device is subjected to external excitation of 1 g at 25 Hz. Although the instantaneous power is very large immediately after the impact, the average power is much lower. The device modeling also serves to reveal rich nonlinear dynamics phenomena caused by the intermittent contact between the oscillator and the cantilever. We have also determined the low resonant frequency cantilever beams dimensions for multi-impact with the Si cantilever beam at low frequencies between 5-60 Hz. The width and thickness are, e.g., 1 mm (0.5 mm for each side of the second and third beams), and 50 μm , while the lengths are 6 mm, 8 mm, 10 mm, respectively.

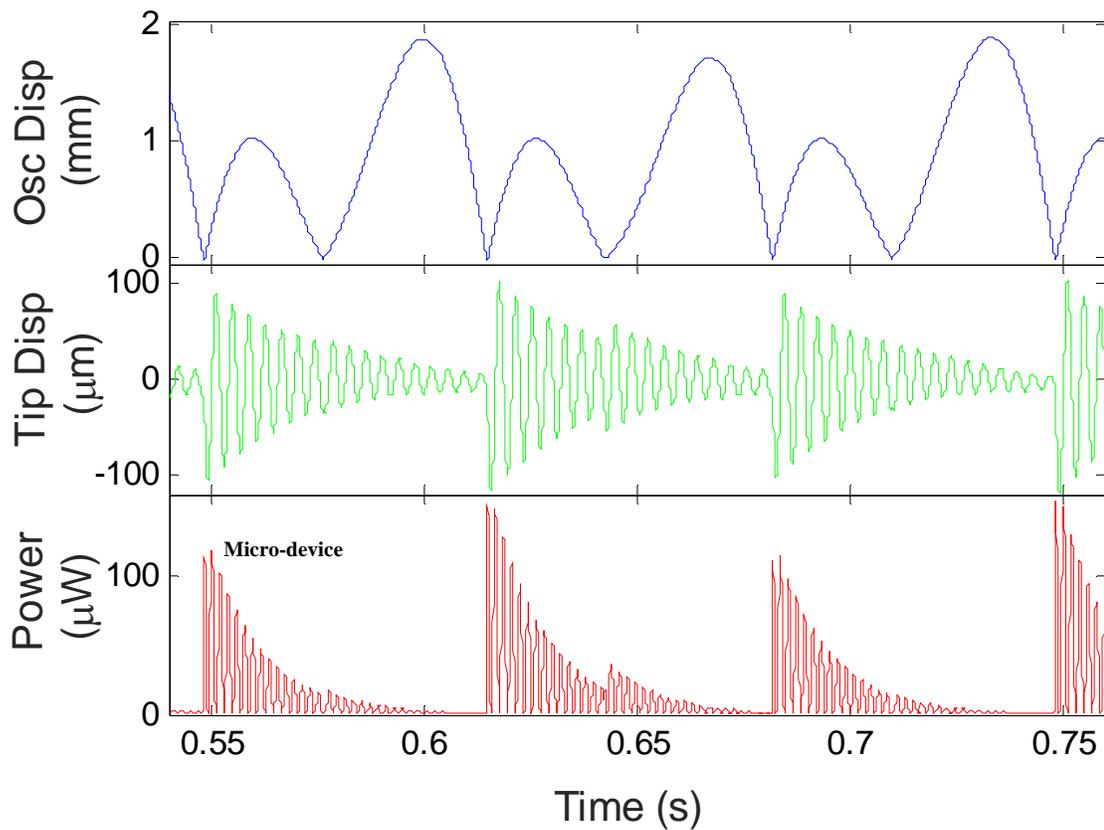


Figure 2.16. Simulation of a micro-power harvester using single impact oscillator at 25 Hz

2.4 Dual-Cavity for Power Harvesting

2.4.1 Device Design

The two cavity MEMS power harvester was designed using parallel plates forming two vertical capacitive cavities. The moving plate was suspended between two fixed plates with equal air gap on each side to form the two cavity device Figure 2.17. The device was designed for out of plane oscillations. When the plate moves, the capacitance increases for one capacitor and decreases for the other. This allows using both up and down directions to harvest power.

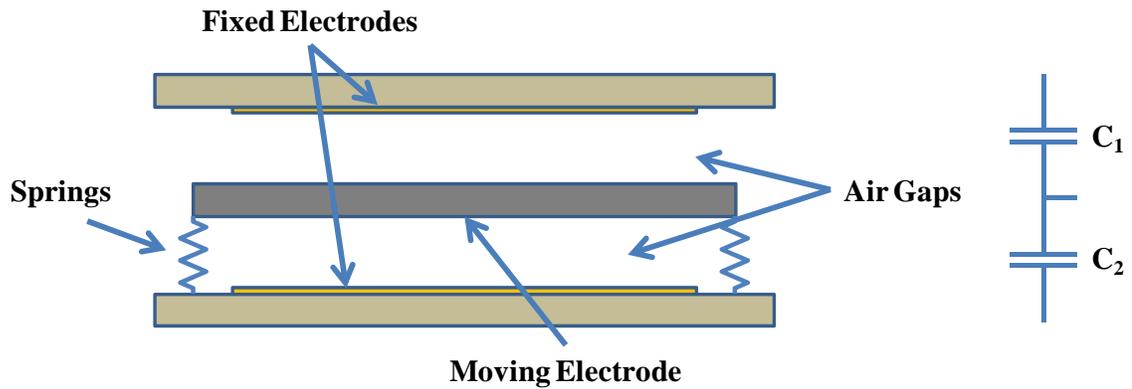


Figure 2.17. Design of the two-cavity MEMS capacitor. Both cavities form capacitors with variable gap. When the plate moves one direction, the capacitance increases for one capacitor and decreases for the other.

The device operates as follow to harvest power: when the plate moves downward under an external force, the capacitance of the bottom cavity becomes larger while the capacitance of the top cavity becomes smaller. If the device is supplied with a voltage source, the bottom capacitor will be charged during this phase. The charging of the bottom cavity will continue until the cavity reaches the minimum separation of plates (Figure 2.18 region I). Then, when the plate moves upward by the external and loaded

spring forces while keeping the charge constant, the capacitance of the lower cavity becomes smaller and the voltage will be increased until it reaches the desired output value (Figure 2.18 region II). After that instance the charge in the capacitor will flow towards the load circuit (Figure 2.18 region III). In the meantime the top cavity capacitance is increased and keeps charging during the upward motion until the top cavity reaches the maximum capacitance value (Figure 2.18 region IV). Then plate starts to move downward and the voltage on the top capacitor will be increased. When the voltage reaches the desired value, the top capacitor will be discharged through the load (Figure 2.18 region VI).

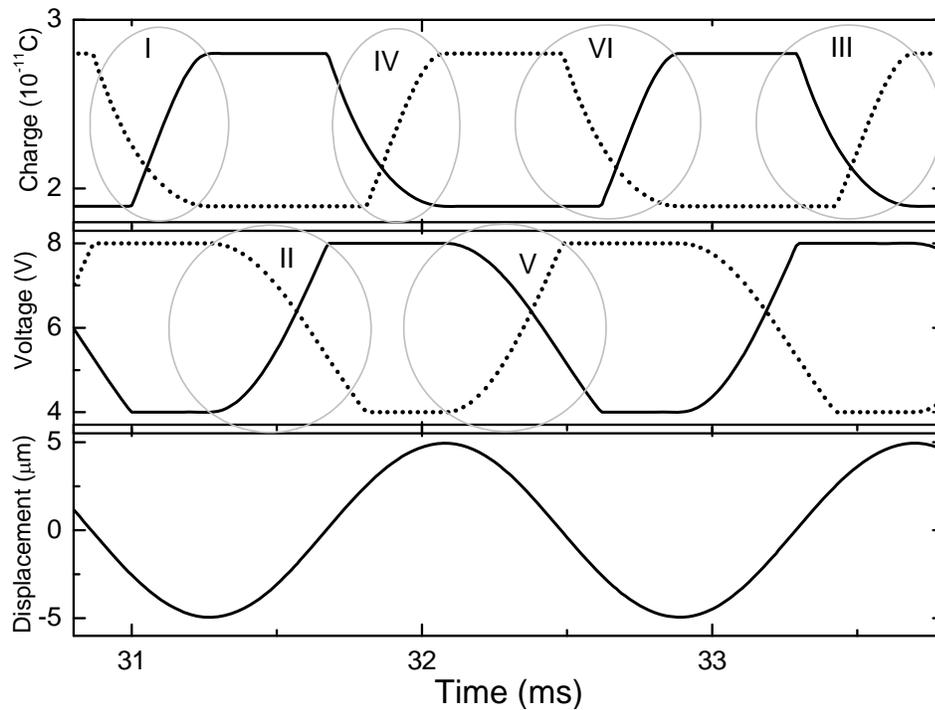


Figure 2.18. Timeline of the two-cavity device for small external forces.

The device is designed with the same parameters used for single cavity device. To form the top cavity, another substrate with fixed electrode and Ni bonding tabs with $30 \mu\text{m}$ height were used (Figure 2.19).

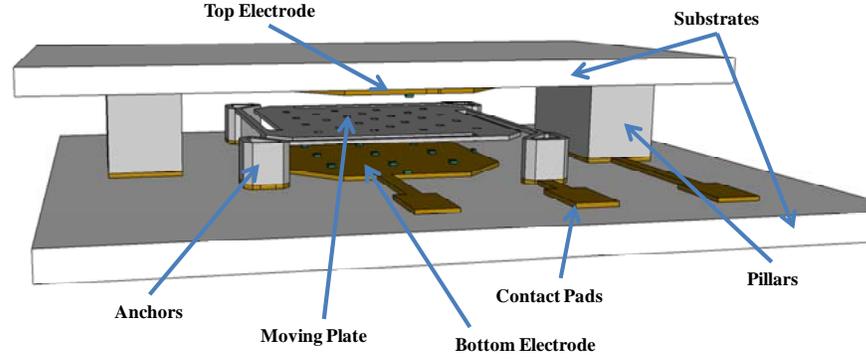


Figure 2.19. 3D model of two-cavity MEMS capacitor for microfabrication. The movable plate, suspension beams and anchors are made of electroplated Ni. The fixed electrodes and traces along with contact pads are designed as Au thin film. Stoppers on the fixed electrodes are coated with SiO₂.

2.4.2 Lumped Element Model

For the transient behavior under sinusoidal excitation conditions, equation of the motion for the lumped element model is solved numerically. For the model, the large plate is considered as the proof mass and the four straight beams are regarded as a single spring. Air gaps under and above the plate behaves as mechanical dampers. In addition, an electrostatic force as a function of the total charge on the plate and the distance between the moving plate and the fixed plate affects from both sides of the plate.

If a 1 degree of freedom damped mass spring system is subject to an external sinusoidal force, the equation of motion of the system will be in the following form

$$m\ddot{x} + c\dot{x} + kx = F_{ext} \quad (10)$$

Then under an additional electrical force, the equation of motion becomes [81]

$$m\ddot{x} + c\dot{x} + kx + F_e = F_{ext} \quad (11)$$

where c is the damping constant, k is the spring constant and F_e is the electrical force;

$$F_e = -\frac{1}{2} \frac{\epsilon A}{(d-x)^2} V^2 \quad (12)$$

For the case in Figure 2.20, the equation of motion can be solved numerically to analyze the mechanical properties of the system. In the absence of electrostatic forces, the solution of the equation for any sinusoidal excitation is straightforward and can be solved.

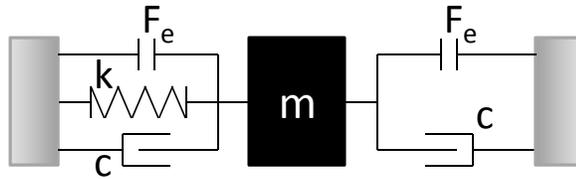


Figure 2.20. Model of the variable two cavity MEMS capacitor with all forces acting on the plate.

To calculate the electrostatic force, the amount of charge has to be calculated at all instances. For the power harvesting circuit as in Figure 2.21, the current flows through the increasing capacitance side of the circuit and the opposite cavity harvests power until the voltage reaches the desired value. Beyond that voltage value, the capacitor is discharged through the storage capacitor. The solution of the equation of motion gives the displacement values of the plate and the corresponding voltage and stored charge values can be calculated accordingly.

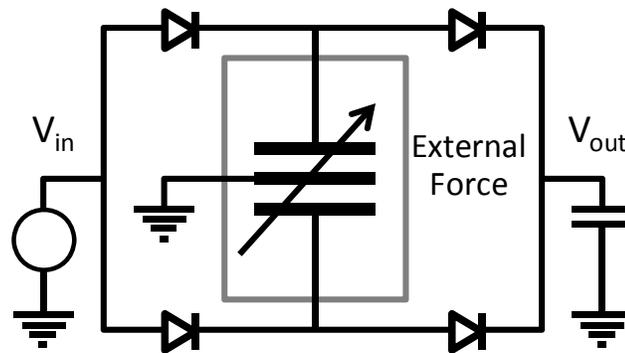


Figure 2.21. Circuit model for power harvesting from a two cavity MEMS capacitor.

2.4.3 Numerical Solutions

The transient behavior of the device was analyzed by solving the equation of motion numerically in the dynamic model for small oscillations where the movable plate does not touch the dielectric stoppers and large oscillations where it does. It should be noted that the dielectric stoppers in the cavity define the maximum allowed capacitance of the tunable capacitive cavity and behaves as very stiff springs that disturb the linear behavior of the oscillation.

For larger amplitudes of excitation, the numerical model results showed a nonlinear behavior and multiple power harvesting actions in a single cycle. We have modeled the stoppers as a 1000 times stiffer spring than the plate suspension spring. As the plate try to move more than allowed physical range, the plate hits the stoppers on the fixed plate and faces additional force caused by the stopper structure. When the plate hits the stopper, it changes the direction of motion while the system is still accelerating the other way. Therefore the plate wants to go back to the plate after it hits. If the initial energy of the plate before the first collision is large enough, the plate jumps several times on the stoppers and generates power on each travel (Figure 2.22).

In large oscillations, (high amplitudes), the movable plate jumps on the stoppers resulting in an extra gain in energy harvesting. For a specific case of 100 μm excitation amplitude in Figure 2.22, plates can harvest power six cycles in a single external vibration cycle. The average current for the two-cavity model with varying external vibration amplitude is shown in Figure 2.23. Due to the applied voltage on the capacitors, pull in behavior prevents the plate from moving and yield drops to zero, i.e. device does

not work in forbidden amplitude region. After pull in force is overcome by external force, the nonlinear behavior due to stopper kicks in, and efficiency jumps more than one order of magnitude.

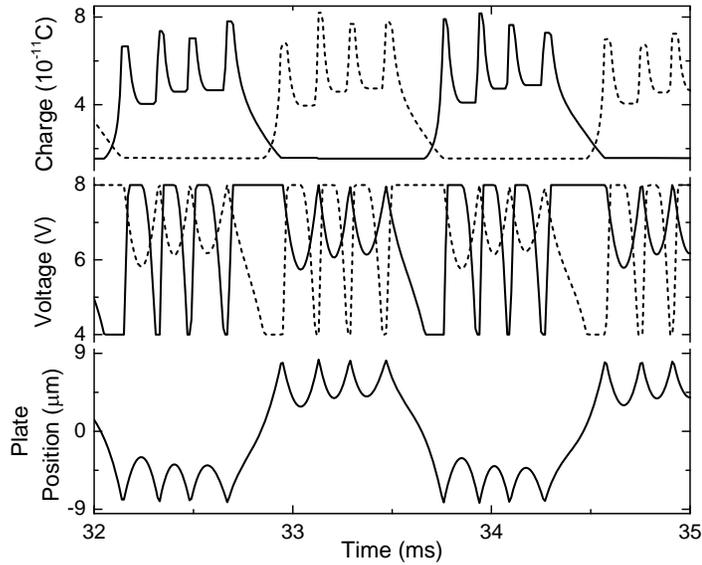


Figure 2.22. Numerical solution of the power harvesting circuit for transient behavior of the metallic plate and the corresponding output voltage and capacitance values.

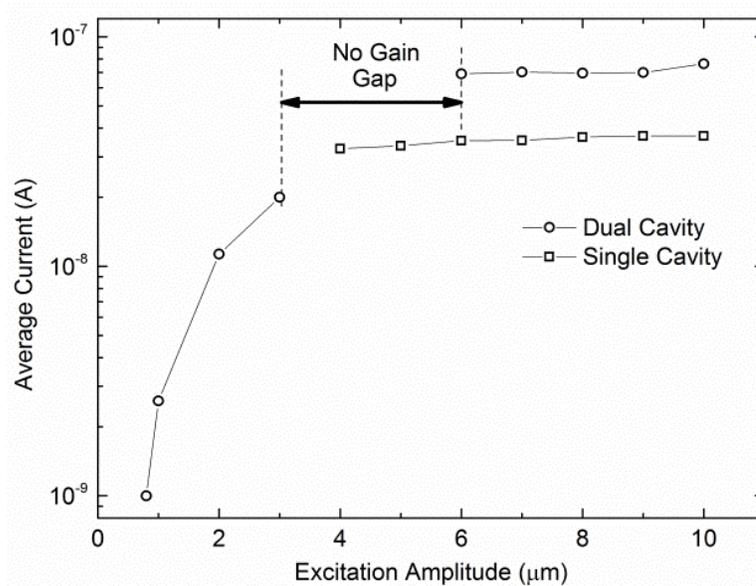


Figure 2.23. Average current harvested from a variable cavity harvester versus external vibration for single and dual cavity devices.

2.5 Broadband Electromagnetic MEMS Power Harvester Design

2.5.1 Theory

Faraday's law of induction explains the interaction between a magnetic field and an electric circuit to produce an electromotive force (EMF) i.e. electromagnetic induction. This phenomenon is the basic principle of transformers, inductors, electrical motors, generators and solenoids [82]. When the coil moves relative to the permanent magnets, an electromotive force (EMF) is generated proportional to the relative velocity of the coil and the magnetic field strength. When the generated EMF is applied to a load resistor, electric current flows through the coil. Therefore, the electromagnetic power harvester itself can be adequately described by a linear system. The effect of the power harvester on the vibration of the silicon cantilever beam can be incorporated into the damping ratio for the cantilever.

According to Faraday's law, a time varying magnetic flux through closed loop of conducting wire induces voltage across the loop as:

$$\varepsilon = -\frac{d\phi}{dt} \quad (13)$$

Here t is time and ϕ is the magnetic flux described as $\phi = \vec{B} \cdot \vec{A}$ where \vec{B} is the magnetic flux density and \vec{A} is the area of the loop. Then similarly the induced EMF for a changing magnetic flux through a coil with N turns is:

$$\varepsilon = -N \frac{d\phi}{dt} = -N \frac{d(\vec{B} \cdot \vec{A})}{dt} \quad (14)$$

For a moving coil in a non uniform magnetic field, the induced EMF can be described as

$$\varepsilon = -N \left[\frac{d\vec{B}}{dt} \cdot \vec{A} + \vec{B} \cdot \frac{d\vec{A}}{dt} \right] \quad (15)$$

For a finite size permanent magnet aligned in x-direction and a coil aligned in z-direction as in Figure 2.24, equation (15) becomes

$$\varepsilon = -N \left[A \frac{dB_z}{dt} + B_z \frac{dA}{dt} \right] \quad (16)$$

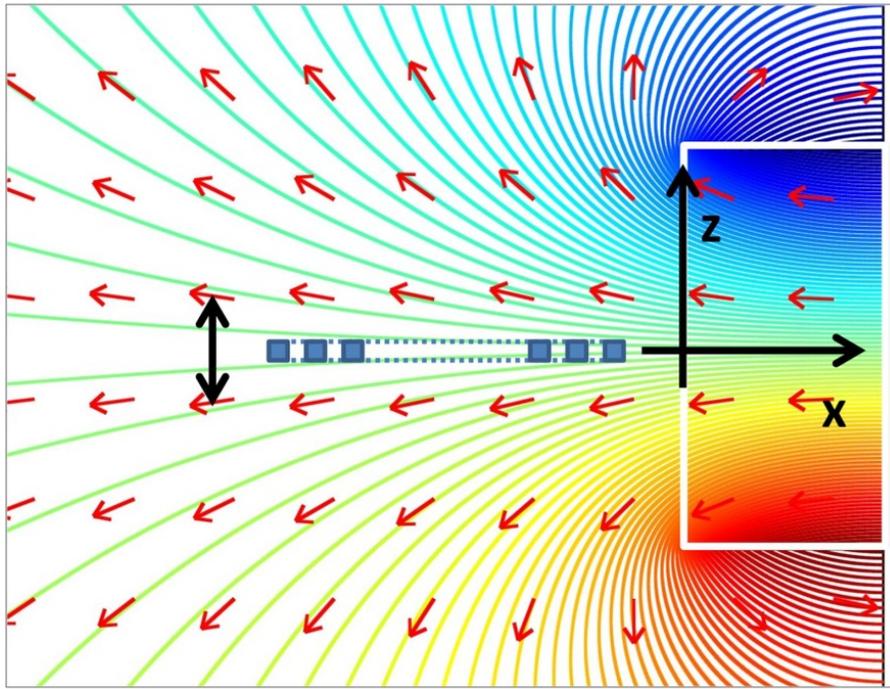


Figure 2.24. Magnetic field profile near a rectangular permanent magnet.

assuming small oscillations in z-direction and $\frac{dA}{dt} = 0$, the approximate induced EMF

$$\varepsilon = -NA \frac{dB_z}{dt} \quad (17)$$

The relative position of the coil can be transferred into magnetic field change.

$$\varepsilon = -NA \frac{dB_z}{dz} \frac{dz}{dt} \quad (18)$$

here $\frac{dB_z}{dz}$ is the magnetic flux change in z-direction and $\frac{dz}{dt}$ is the velocity of the coil.

When there is a harmonic oscillation of the coil in z-direction as $z = z_0 \cos(\omega t)$

$$\varepsilon = NA\omega \frac{dB_z}{dz} z_0 \sin(\omega t) \quad (19)$$

and for decaying oscillations with a decay constant ζ ,

$$\varepsilon = NA\omega \frac{dB_z}{dz} z_0 e^{-\zeta\omega t} \sin(\omega t) \quad (20)$$

2.5.2 Device Design

We designed and built a macro-scale wideband EM power harvester prototype for low frequency vibration using two impact-oscillators [83] and three-impact oscillators (Figure 2.25). The device consists of a copper pick-up coil, fixed at the free edge of an aluminum (Al) cantilever clamped at one side with a length, width, thickness and high resonant frequency of 65 mm, 25.4 mm, 1.63 mm, 210 Hz, respectively, and three cantilevers with a length of 40 mm, 50 mm and 55 mm, width of 6 mm, and thickness of 0.3 mm, respectively, made of brass sheet vibrating at low excitation frequency, each with a thick impact mass attached at its free edge (Table 3). The low-frequency cantilever beams were attached on the clamped side of the high resonance frequency cantilever. Three cantilevers are designed to resonate at 12 Hz 19 Hz and 40 Hz within the range of ambient vibration frequency. A rectangular shaped permanent NdFeB magnet with a size of 3/8", 3/8", and 5/8" and surface magnetic field of 6,950 Gauss is placed in front of the cantilever on a vibrating stage. The pick-up coil has a square shape with area of 12×12 mm² and made of 36 gauge copper wire with 200 turns. The metallic impact masses each

has a weight of 4 grams, and are used in order to reduce the cantilever's resonance frequency and improve the momentum transfer to the high frequency cantilever.

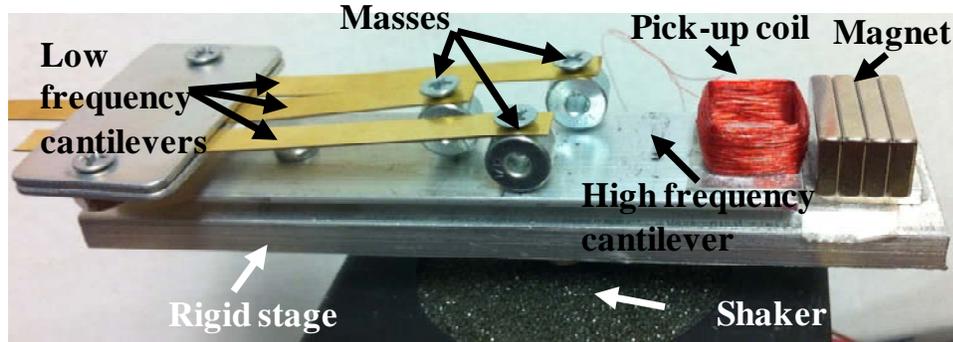


Figure 2.25. A photo of the electromagnetic power harvester.

Table 3. Dimensions and corresponding frequencies for the cantilevers used in electromagnetic power harvesting device

	Thickness (mm)	Length (mm)	Width (mm)	Resonance Frequency (Hz)
LF cantilever 1	0.4	55	6	12
LF Cantilever 2	0.4	50	6	19
LF Cantilever 3	0.4	40	6	40
HF Cantilever	1.6	65	25.4	210

When the power harvester was subjected to a low frequency vibration using a shaker, the three low-frequency cantilevers responded by vibrating at low frequencies with at least one of them vibrating close to its resonance frequency, and thus their thick metallic masses made impacts with the high resonance frequency cantilever repeatedly at three locations. This has caused it along with the pick-up coil to oscillate, relative to the permanent magnet, with decaying amplitude at its resonance frequency. As the high frequency cantilever oscillated in front of the magnet, an electromotive force (EMF) proportional to the relative velocity of the coil and the magnetic field strength was generated. When the generated EMF was applied to a load connected in series with the

pick-up coil, an electric current flowed through the coil due to the magnetic flux change per unit time from the low frequency vibration after the impact occurs. Therefore, after the impact occurs, the absorbed energy by the three low-frequency cantilever beams were transferred to the high resonance frequency cantilever beam along with the pick-up coil, and then to the electrical domain.

2.5.3 Device Modeling

Physical model of the energy transfer through intermittent contact between a low frequency oscillator and a high frequency cantilever was prepared (Figure 2.26). We considered the cantilever massless, although we may include the beam inertia later on. The power harvesting device is modeled by a mass m_2 at the free edge of the cantilever. Another mass m_1 supported by a linear spring models one of the three masses supported by three shorter cantilevers in Figure 2.26. It is designed with a resonance frequency in the range of low frequency vibration, 10-60 Hz.

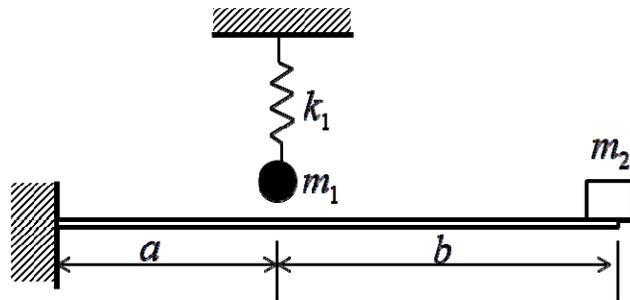


Figure 2.26. The physical model of a low frequency oscillator in intermittent contact with a cantilever supporting a coil at the edge.

Our complete system includes the linear oscillator and the long cantilever on a vibrating structure (Figure 2.26). We treated the support as fixed and apply inertial forces on concentrated masses following d'Alembert's principle to simplify the model. We use

y_1 to denote the position of the mass m_1 measured from the impact point of the beam. Let x_1 be the displacement of the potential impact point on the beam. Let F_1 be the contact force acting on the mass m_1 by the cantilever. When the whole system is subjected to an excitation with acceleration of $-A\omega^2\sin(\omega t)$, the equation of motion for mass m_1 is given below:

$$m_1\ddot{x}_1 = -k_1x_1 - c_1\dot{x}_1 - m_1A\omega^2\sin(\omega t) + F_1 \quad (21)$$

The equation for the mass m_2 at the free edge of the cantilever beam is:

$$m_2\ddot{x}_2 = -c_2\dot{x}_2 - m_2A\omega^2\sin(\omega t) + F_2 \quad (22)$$

where F_2 is the total force acting on the mass by the cantilever. The forces F_1 and F_2 are calculated based on whether mass m_1 makes contact with the cantilever. The force calculation can be done by assuming that m_1 does make contact with the cantilever. We can directly calculate the displacements using engineering beam theory and the principle of superposition:

$$x_1 = -\frac{(F_1 + F_2)a^3}{3EI} - \frac{F_2ba^2}{2EI} \quad (23)$$

$$x_2 = x_1 + \left[-\frac{(F_1 + F_2)a^2}{2EI} - \frac{F_2ba}{EI} \right] b - \frac{F_2b^3}{3EI} \quad (24)$$

Solve the above two equations for the forces. We get

$$F_1 = -\frac{12(a+b)^3EI}{a^3b^2(3a+4b)}x_1 + \frac{6(2a+3b)EI}{ab^2(3a+4b)}x_2 \quad (25)$$

$$F_2 = \frac{6(2a+3b)EI}{ab^2(3a+4b)}x_1 - \frac{12EI}{b^2(3a+4b)}x_2 \quad (26)$$

If the contact force F_1 obtained from the above formula is negative, it implies that mass m_1 does not make contact with the cantilever. Therefore, we have

$$F_1 = 0 \quad \text{and} \quad F_2 = -\frac{3EI}{(a+b)^3}x_2 \quad (27)$$

The coefficients c_1 and c_2 in (1) and (2) account for the energy dissipation in the impacting mass and in the motion of the power harvesting device. Note that as power is harvested, electric current flows through the coil. This in turn generates a mechanical force in the presence of the magnetic field. This force is proportional to the velocity, contributing to the overall energy dissipation of the device. Since the current through the coil is determined by the external load. We assume the external load is a resistor and therefore the damping coefficient c_2 is dependent on the external load resistance.

2.5.4 Simulation Results

When the complete system is subjected to an external base excitation, the responses of the system are strongly dependent on the forcing frequency. Bear in mind that the impact oscillator is designed to harvest low frequency vibrations. Therefore we assume that the base excitation frequency is much lower than the natural frequency of the cantilever but comparable with the natural frequency of the impact oscillator. A representative response of the designed device along with the modeling parameters in are shown in Figure 2.27.

The simulation was performed for a silicon cantilever beam with 210 Hz resonance frequency. The beam is impacted by a low frequency impact oscillator with an excitation frequency near the resonance frequency of the impact oscillator. The Figure 2.27 shows

the period doubling phenomenon when the device is subjected to external excitation of 1 g at 15 Hz. We have obtained an average power of 15.28 μW and 3.82 μW across 20 Ω load resistor for 1 g and 0.5 g acceleration, respectively. The device modeling also serves to expose nonlinear dynamics phenomena caused by the irregular contact between the mass and the cantilever.

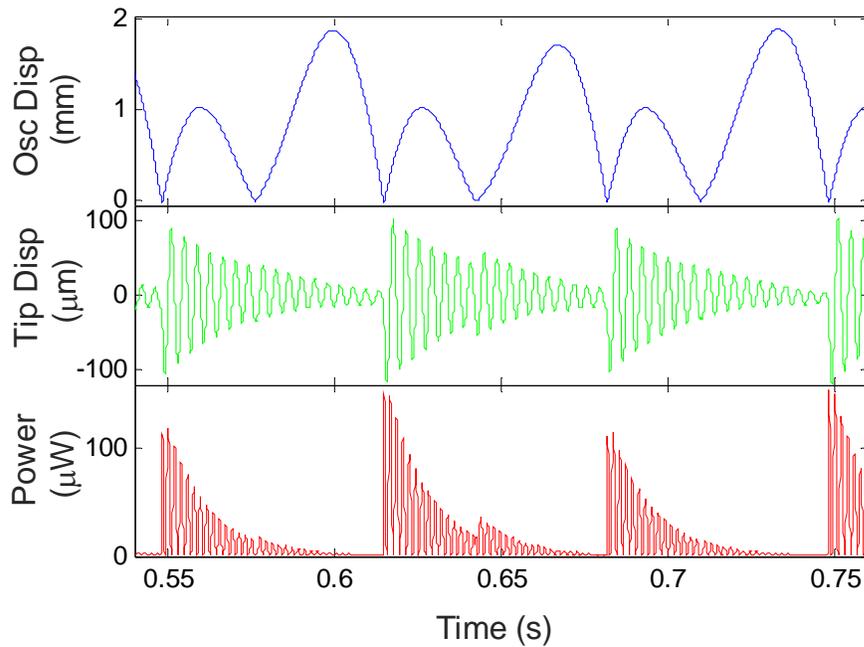


Figure 2.27. Simulation of a macro-power harvester using single impact oscillator at 15 Hz. The average power was 15.28 μW at 210 Hz and 1 g excitation.

CHAPTER 3

DEVICE FABRICATION

This chapter first introduces the microfabrication techniques used in the fabrication of the variable MEMS capacitors which includes surface micromachining, photolithography, different photoresists and electroplating processes adapted to fabricate the MEMS capacitors. Then mask designs and fabrications and device fabrication on Si and glass substrates will be described step by step in details.

3.1 Fabrication Procedures and Materials

3.1.1 Microfabrication

a) Photolithography

Photolithography is a method of patterning a layer of UV sensitive organic material (namely photoresist). Depending on the chemical response of the photoresist, either a positive or a negative image is produced on the film. Photoresist is generally composed of three major components: polymer, photo active compound and solvent. It is the basic technique used to define and transfer patterns in most micromachining and integrated circuit (IC) fabrication processes. Photolithography allows us to define any 2D pattern on the surface of a substrate.

A standard photolithography process begins with a thoroughly cleaned substrate by using piranha solution, acetone and isopropanol (IPA). The substrate is placed and centered on a spinner chuck and held by vacuum. A small amount photoresist is

dispensed on the substrate and then the chuck is spun at a predefined speed to produce a film with a uniform thickness photoresist film. The thickness of the photoresist layer is determined by the viscosity of the material, the spin speed and also spinning time. After spin coating, a soft bake process is performed to reduce the solvent amount within the photoresist. Soft bake process is usually carried out on a fixed temperature hot plate for smaller number of samples. For larger quantities, it can be done by convection oven for a longer time.

After soft baking, the substrate is cooled down to room temperature and exposed to UV light through a photomask using a mask aligner. A photomask usually consists of chromium patterns on soda lime glass. After alignment, the substrate is pressed against the mask to obtain a physical contact with no gap between the substrate and Cr pattern. The mask-substrate pair is then exposed to UV light through the mask by selectively exposing the desired portions of the photoresist as shown in Figure 3.1. The exposure time of UV light must be selected according the power density of light source and

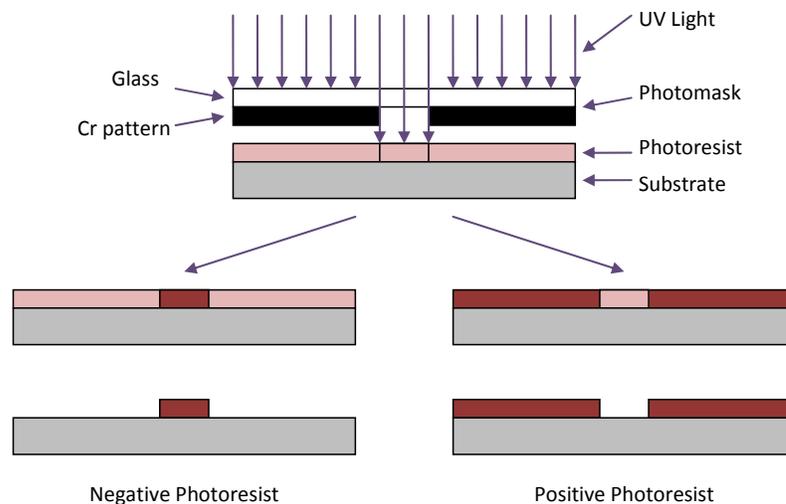


Figure 3.1. Schematics showing the photolithography processes for positive and negative photoresist.

properties and thickness of the photoresist film. The exposed area of the photoresist is either degraded for a positive photoresist or polymerized for negative photoresist.

The unwanted parts of the exposed photoresist are removed chemically by special solution called as developer. For a positive photoresist, the exposed area is dissolved in the developer, and the unexposed area does not interact with the solution. On the other hand, the unexposed area in a negative photoresist is dissolved in the developer.

b) Sputter deposition

Sputter deposition is a physical vapor deposition (PVD) method of depositing uniform thin films with the help of a plasma source. Sputtering is usually referred as atoms ejection from a solid target by bombarding it with accelerated inert gas ions (Argon ion in most cases). A gas discharge is initiated by plasma and the positively charged gas ions are accelerated towards the negatively charged target material (Figure 3.2). After colliding with the target, gas ions remove some target atoms by momentum transfer. These atoms spread into the chamber and condense as a thin film on the substrate and on the walls of the deposition chamber [84].

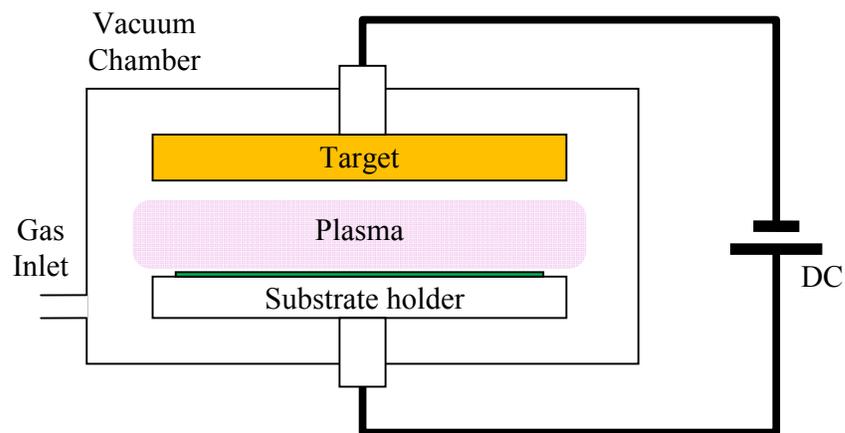


Figure 3.2. Circuit and details of a DC Sputtering system.

Figure 3.3 shows the instrument used for DC-sputtering. Target and substrate faces each other in a vacuum chamber with distance of couple of centimeters. The target is connected to the negative side of the DC power supply, acting as the cathode and the substrate and chamber walls are connected to the positive side of the power supply and act as the anode. After reaching a high vacuum level, an argon atmosphere with a pressure of about 10^{-3} to 10^{-2} mbar is sustained achieved. By applying a DC voltage, the gas discharge is ignited. The created Ar^+ -ions are accelerated towards the target and eject atoms from the target. The free atoms of substrate material are deposited on the substrate as a thin film. DC sputtering is suitable for all conductive target materials but it is impossible to sputter dielectric materials with DC sputtering. The positive charged ions can't flow through the insulator to complete the circuit. Eventually the potential at the cathode drops and the positive ions can no longer be accelerated towards the target [84].

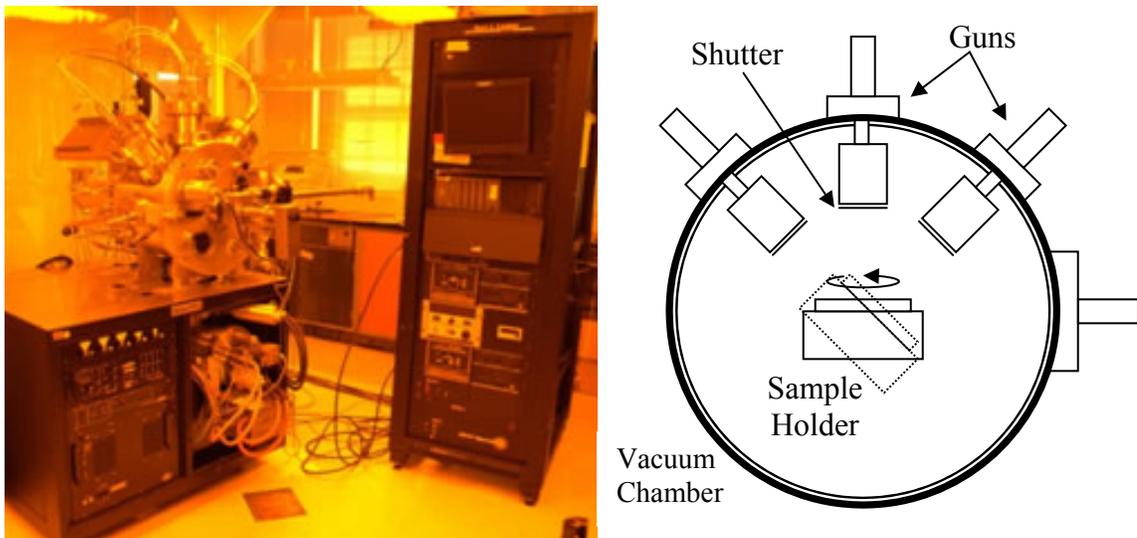


Figure 3.3. The sputtering deposition system and schematics of the chamber and gun locations.

To sputter insulating materials as well as conducting materials, another technique, RF-sputtering is used. In the RF-circuit (Figure 3.4) a negative DC-potential is built up at the target due to the different mobility of heavy ions and light electrons in a high-frequency electric field (13.56 MHz). Since the positive charges don't need to flow through the target to complete the circuit, sputtering of dielectric materials is also possible by RF sputtering. In addition, there is a higher level of ionization caused by the oscillating movement of the free electrons in the RF field resulting in faster deposition rates [85]. Figure 3.5 shows the photo and a detailed sketch of the RF magnetron sputtering chamber used.

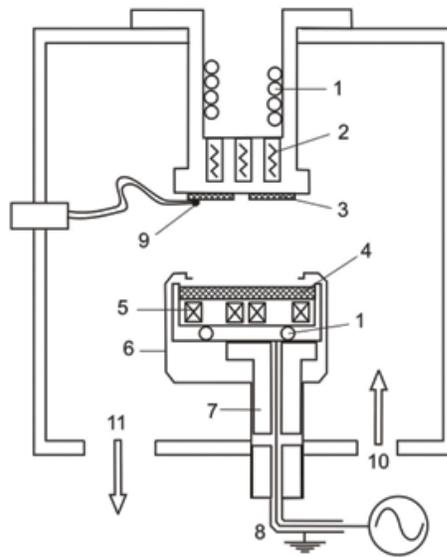


Figure 3.4. RF magnetron sputtering chamber geometry and main components: 1-water cooling line, 2-substrate heater, 3-substrate, 4-target, 5-permanent magnets, 6-shield, 7-insulator, 8- RF cable, 9-thermocouple, 10-gas inlet and 11-vacuum system [85].

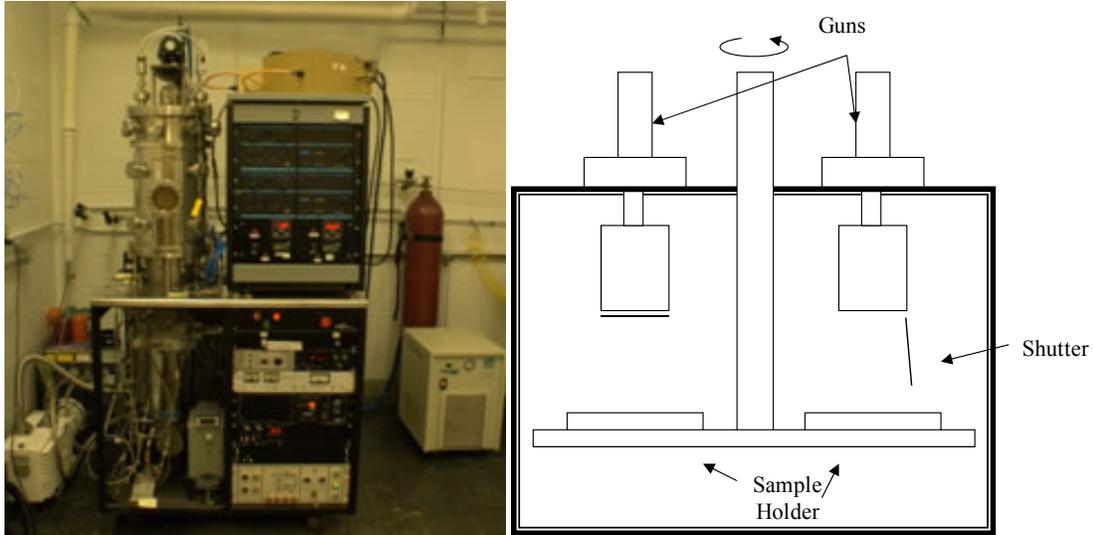


Figure 3.5. The RF sputtering deposition system and schematics of the chamber and gun locations.

d) Electroplating

Electroplating is the deposition of a metal on a negatively charged object in an electroplating solution of metal salts. Positively charged metal ions in the solution are attracted towards the negatively biased substrate. Electrons in the circuit are supplied to the surface of the exposed cathode metal and metal ions in the solution are reduced at that surface (one or more electrons are added to each metal ion so that it becomes a stable metal atom), and deposited onto the surface, as shown in Figure 3.6.

General process flow of electroplating for MEMS devices is shown in Figure 3.7. First, a thin film of metal seed layer is deposited on the substrate by sputtering. Photoresist is spin coated and patterned to form a mold for electroplating. The deposition rate of electroplating is controlled by the applied DC current density. The thickness of the deposited material can be measured by surface profiler without disturbing the mold. Photoresist is then washed away after electroplating and the unwanted parts of the exposed seed layer are removed by etching.

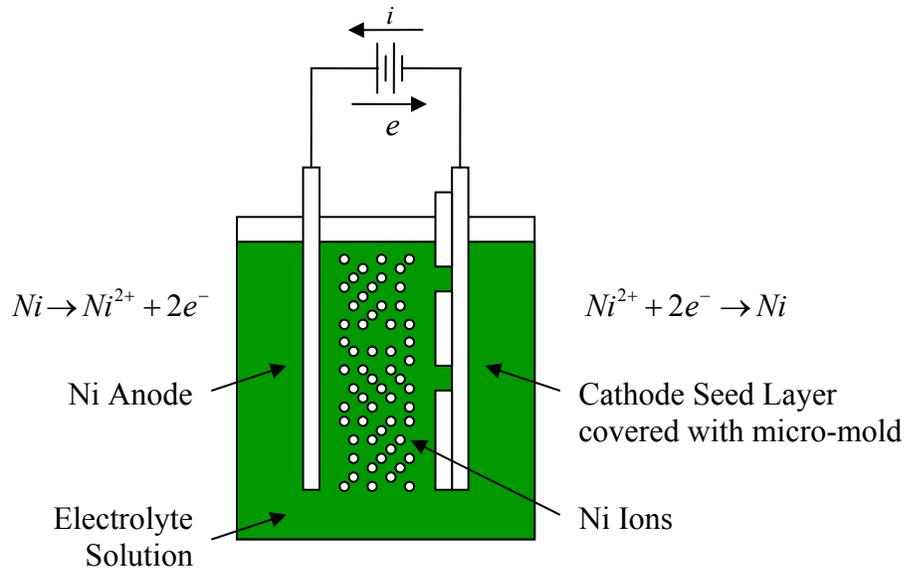


Figure 3.6. Ni electroplating setup in a Nickel Sulfamate solution.

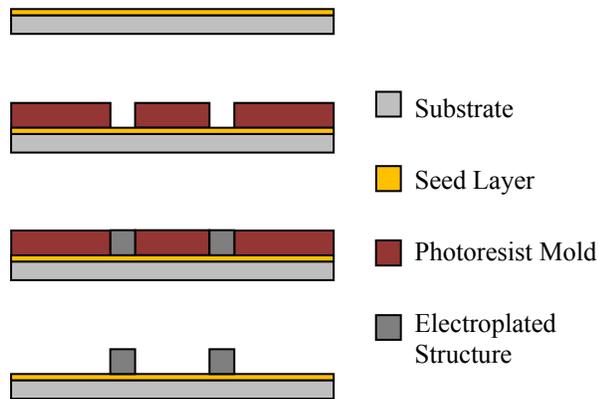


Figure 3.7. Schematics of general process of electroplating.

The substrate with the patterned mold is connected to the cathode side and the Ni electrode is connected to the anode side of the circuit. The power supply is switched to the constant current (CC) mode and the current limit is set to 10 mA for a full wafer. After making all connections in the circuit, the target and the wafer are lowered into the solution. The reduction process happens on the cathode:



The growth rate of the deposited material inside a mold is determined by the current density on the cathode. Nickel Sulfamate $Ni(SO_3NH_2)_2$ was chosen as a source of Ni electroplating solution because of its high temperature resistance, high tensile strength and high ductility and corrosion and oxidation resistance.

e) Etching

Etching is a process that utilizes dry gases or wet chemical to remove some of the bulk material or deposited films on a substrate. A patterned photoresist film can be used as an etch mask. If the etch rate of material is faster than the etch rate of the photoresist or etch mask then the film can be etched without disturbing the initial pattern on the mask. Etching process flow is shown in Figure 3.8.

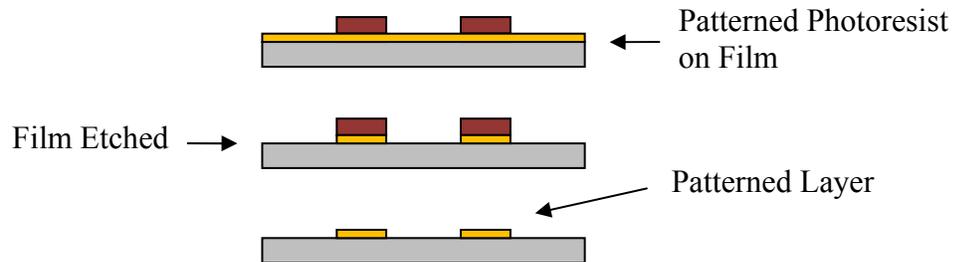


Figure 3.8. Schematics of general process of etching

In dry etching process, a plasma etching system such as reactive ion etching (RIE) is used to etch substrate or thin films in a low pressure chamber (Figure 3.9). The plasma is generated by an RF power supply operated at frequency of 13.56 MHz.

Initially a photoresist film is patterned on the substrate and then the substrate is subject to plasma generated free radicals inside a vacuum chamber. The exposed material is removed by ion assisted chemical reaction. For example, in Si etching with SF_6 , Si

reacts with Fluorine (F) and forms Silicon Fluoride (SiF_4) by the following chemical reaction



and volatile SiF_4 molecules are carried away by the gas flow in the chamber. We have used Oxford Plasmalab 80 Plus RIE tool in this project as shown in Figure 3.10.

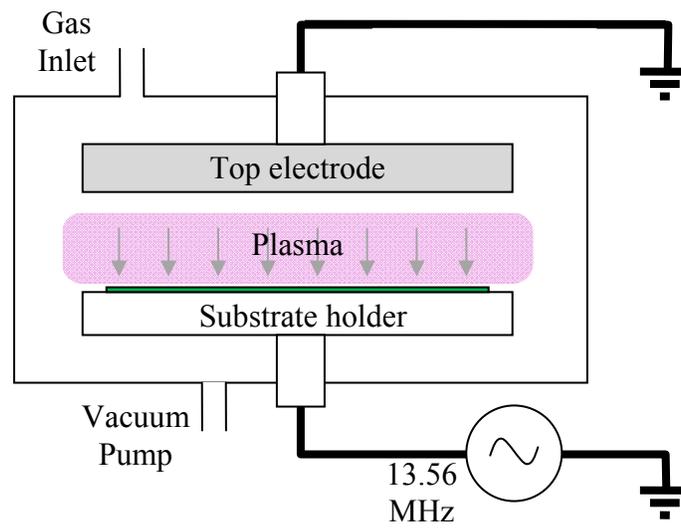


Figure 3.9. Circuit and schematics of the RIE chamber. The substrate holder is water cooled.

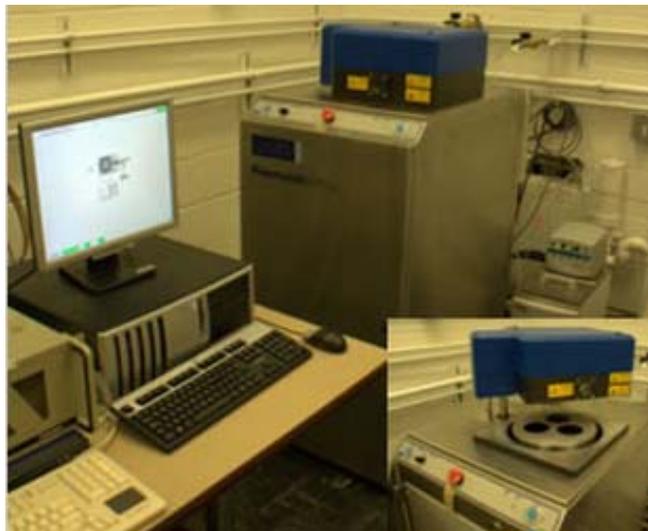


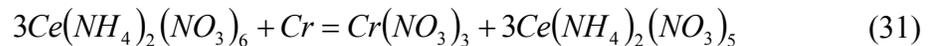
Figure 3.10. Oxford Plasmalab 80 Plus Reactive Ion Etching (RIE) system.

In wet etching, a photoresist film is patterned on the substrate and then the substrate is immersed in the etchant solution. The exposed film is removed by chemical reaction. After the film is removed from the unwanted parts, the photoresist masking layer is removed using Acetone and IPA. For example, in gold (Au) etching solution, Au reacts with Iodine (I₂) and forms gold iodide (AuI) by the following chemical reaction:



The solubility of AuI can be increased by adding potassium iodide (KI) into the solution. An etch rate of 1 μm/min can be obtained by the solution with the ratio of I₂:KI:H₂O = 1:4:40 g at room temperature. This solution may attack the electroplated Ni in some cases. If Au film is used as seed layer for Ni electroplating, then the etching process must be performed in a very controlled manner.

Chromium is selectively etched by ceric ammonium nitrate $Ce(NH_4)_2(NO_3)_6$ and the reaction is governed by the equation



f) Lift off

Lift off is a simpler method to remove a single or multiple layers of films in a single step without any etchant chemical. It is also used to remove hard to etch materials and occasions where etching may damage other components. The process is explained in Figure 3.11 as follows. A photoresist layer is spin coated and patterned on the substrate and then the thin film is deposited on the substrate. When the photoresist is removed in a solvent, the unwanted thin film is lifted off by the solution.

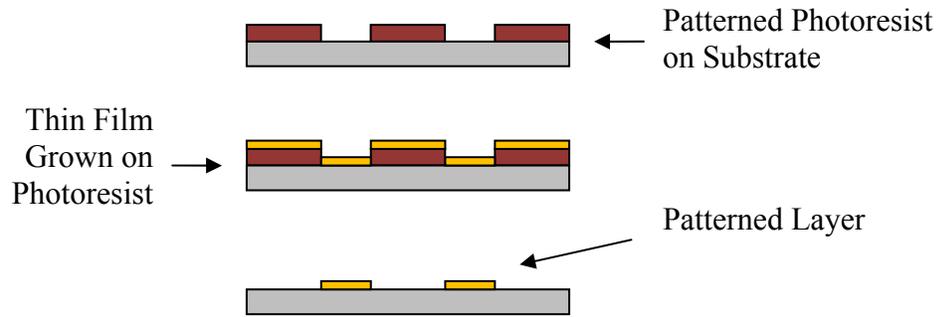


Figure 3.11. Schematics of general process of lift-off. A photoresist layer is spin coated and patterned on the substrate and then the thin film is deposited on the substrate. When the photoresist is removed in a solvent, the unwanted thin film is lifted off by the solution.

3.1.2 Materials

The required materials to fabricate the MEMS capacitors with two cavities need to have very good electrical properties in addition to all mechanical and physical properties. They need to be pure, cheap and well characterized materials. They need to have potential for integration with control and signal processing circuitry.

a) Silicon (Si)

Silicon wafers were chosen as the substrate material. It has a low thermal expansion coefficient and mechanical properties don't change during the surface micromachining process. CMOS process was established on Si wafers and it is the only well investigated material with all electrical, mechanical and thermal properties. Additionally, the driving circuitry for the device can be fabricated on the Si substrate prior to MEMS fabrication. A very good dielectric material SiO_2 can be achieved in Si very easily by different growth techniques providing a good isolation between the device layers.

b) Gold (Au)

Gold was chosen as the material for the bonding pads and interconnections as well as electrodes, and trace lines. It has a low electrical resistance and the micro-fabrication technology of Au is well-established. However, the adhesion between Au and SiO₂ surface is poor. Therefore, a thin layer of Cr or titanium (Ti) is used as an adhesion layer. Au was also chosen as the seed layer for electroplating Ni due to less probability of surface oxidation during the preparation photoresist molds.

c) AZ P4620 photoresist

AZ P4620 photoresist was chosen as the sacrificial layer material for the following reasons. It has a relatively higher viscosity and electroplating mold of almost 100 μm can be achieved (Figure 3.12). After curing at suitable conditions, it can withstand sputter deposition process. Also the hard baked resist can be removed easily by using appropriate photoresist strip remover solutions for releasing the structure.

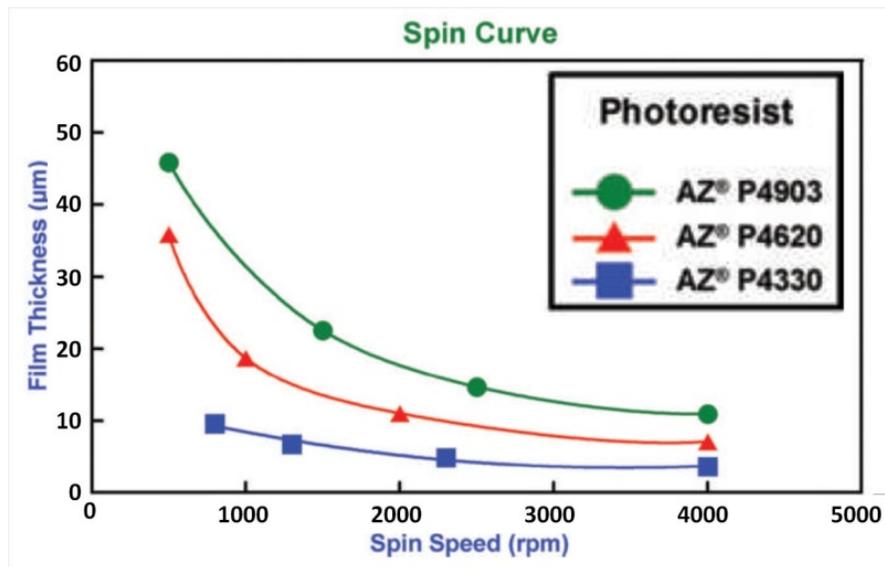


Figure 3.12. AZ P4620 photoresist film thickness vs. spin speed curve [86]

d) Electroplated nickel (Ni)

For the capacitor plate and beams, electroplated Ni was chosen because it makes a conducting film that can be fabricated with various thicknesses up to 100 μm . It provides high deposition rates and mechanically durable material with controllable residual stress. Also electroplated Ni enables low cost devices due to its low price.

e) Electroplated indium (In)

Indium was chosen as the bonding material between the substrates to form the two cavity capacitor. Indium is a conducting material and it can be electroplated on the Ni in the existing mold. It can be softened at a relatively low temperature of 150 $^{\circ}\text{C}$ compared to the other candidates.

3.2 Fabrication Process of MEMS Capacitors

3.2.1 Mask Fabrication

Photomask layouts were drawn using L-Edit Layout Editor software from Tanner, as shown in Figure 3.13. The fabrication of a complete single cavity MEMS capacitor device requires at least four masks and the dual cavity capacitor requires at least seven masks.

- 1) The first mask is used to pattern the wafer prior to oxidation at locations corresponding to the anchor bases and stoppers.
- 2) The second mask is used to pattern the fixed plates, trace lines and bonding pads, and bonding tabs on the bottom substrate.

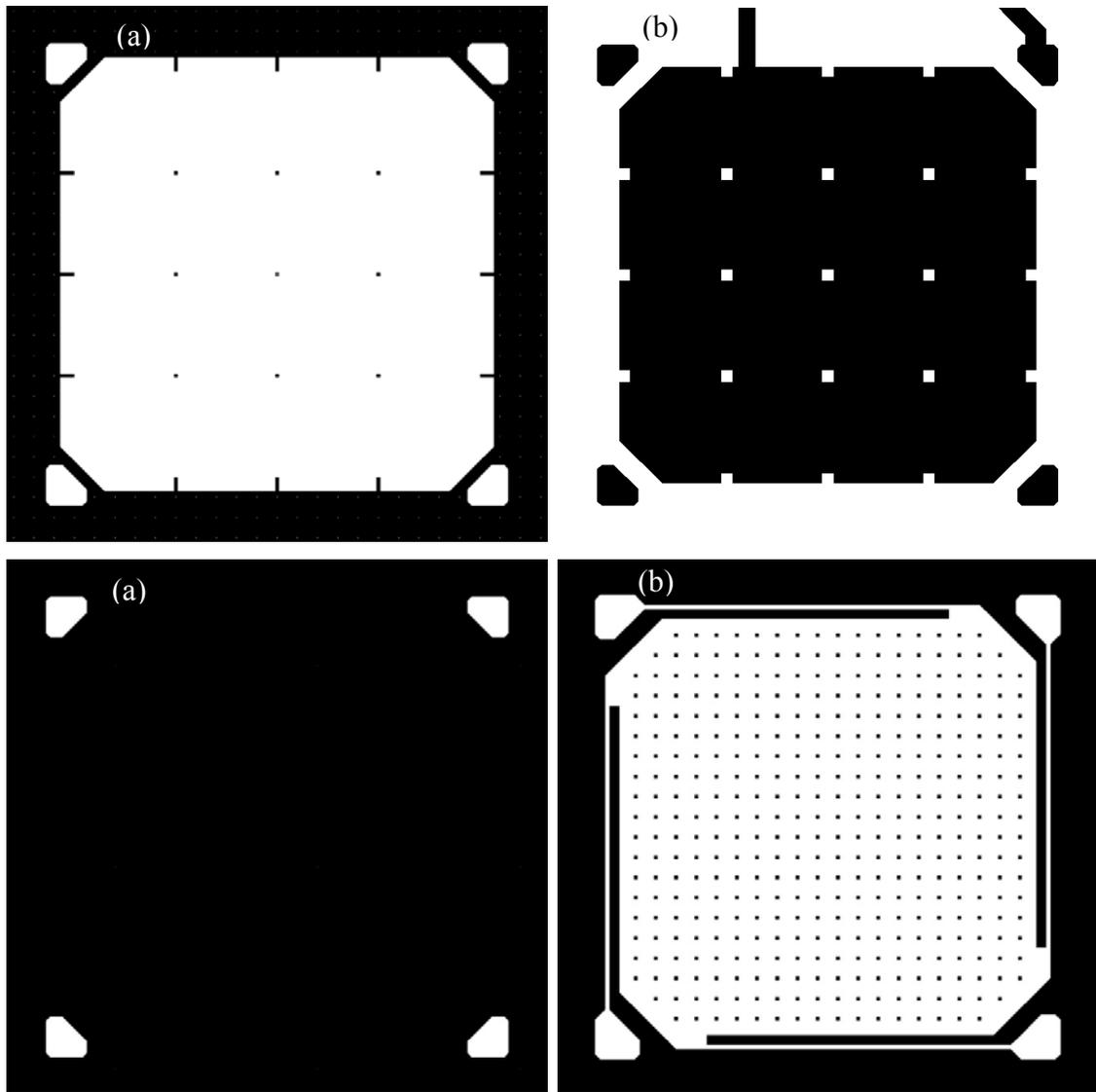


Figure 3.13. a) The layout of Mask I for stoppers and anchor bases of the bottom cavity b) the layout of Mask II for bottom electrodes, bonding pads and anchor bases. c) The layout of Mask III for anchor holes, d) the layout of Mask IV for the capacitive plates and suspension beams.

- 3) The third mask is used to pattern the mold for electroplating bonding tabs for anchors. The photoresist will also serve as a sacrificial layer to create the movable plate.
- 4) The fourth mask is used for electroplating the movable plate

- 5) The fifth mask is used to pattern the second wafer prior to oxidation for bonding tab bases and stoppers.
- 6) The sixth mask is used to pattern fixed electrodes, bonding tabs' bases and trace lines on the second substrate.
- 7) The seventh layer is used for patterning the mold for electroplating the bonding tabs for bonding the two structures together. The bonding tabs are used to bond two substrates together to form the variable capacitor cavities.

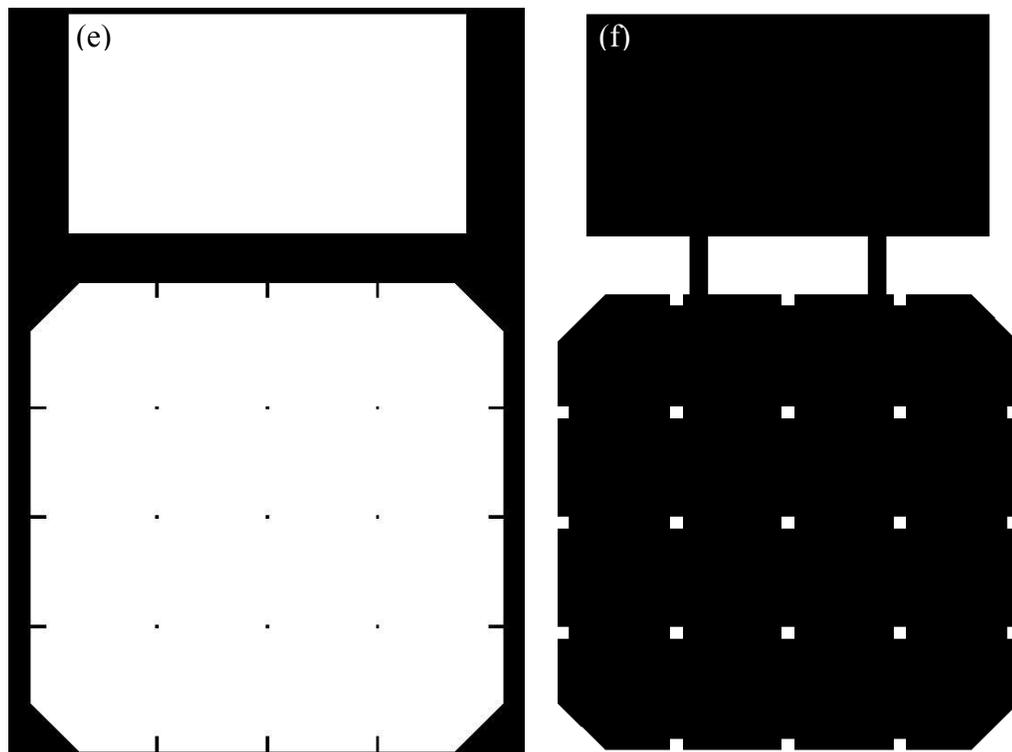


Figure 3.13. e) The layout of Mask V for stoppers and bonding tab bases of the top cavity. f) the layout of Mask VI for top electrode and bonding tab bases.

The layouts of the masks were then printed on a transparency with 65000 dpi resolution using service from an external company. The patterns on the transparency were then transferred to chromium-on-soda lime hard masks using photolithography.

Hard masks are made of 4" square glass plates with a chromium layer and a pre coated AZ-1518 photoresist layer. The chromium layer was patterned by wet etching. The patterned AZ-1518 photoresist layer served as etching mask in wet etching process to finally create the layouts on the chromium layer. Photoresist were removed by acetone after patterning the Cr layer. The fabrication of the complete two cavity MEMS capacitor device requires at least seven masks (Table 4)

Table 4. The masks set used in the fabrication process of MEMS variable capacitors on Si substrate.

	Name	Descriptions
The mask I	Bottom stoppers mask	To create the patterns of stoppers, anchors and bonding tabs for bottom substrate
The mask II	Bottom electrodes mask	To create the patterns of fixed plates, electrodes, trace lines, and the seed layers of anchors and bonding tabs
The mask III	Anchor holes mask	To create the photoresist mold for electroplating the anchors
The mask IV	Movable plate mask	To create the photoresist mold for electroplating the movable plate and anchors with suspension beams
The mask V	Top stoppers mask	To create the patterns of stoppers and bonding tabs for top substrate
The mask VI	Top electrodes mask	To create the patterns of fixed plates, trace lines, and the seed layers of bonding tabs and bonding tabs on top substrate
The mask VII	Bonding tabs mask	To create the photoresist mold for electroplating the bonding tabs

3.2.2 Device Fabrication

The MEMS dual cavity power harvesters were fabricated successfully using surface micromachining technologies using the following sequence on top of a Si substrate.

(1) The Si substrate is cleaned using piranha solution prepared by 1:3 ratio of hydrogen peroxide (H_2O_2) to sulfuric acid (H_2SO_4). The H_2O_2 is 50% concentrate and H_2SO_4 is 98% concentrated. The substrate is immersed in the piranha solution bath for 3 minutes immediately after preparing the piranha solution while it is hot. The active

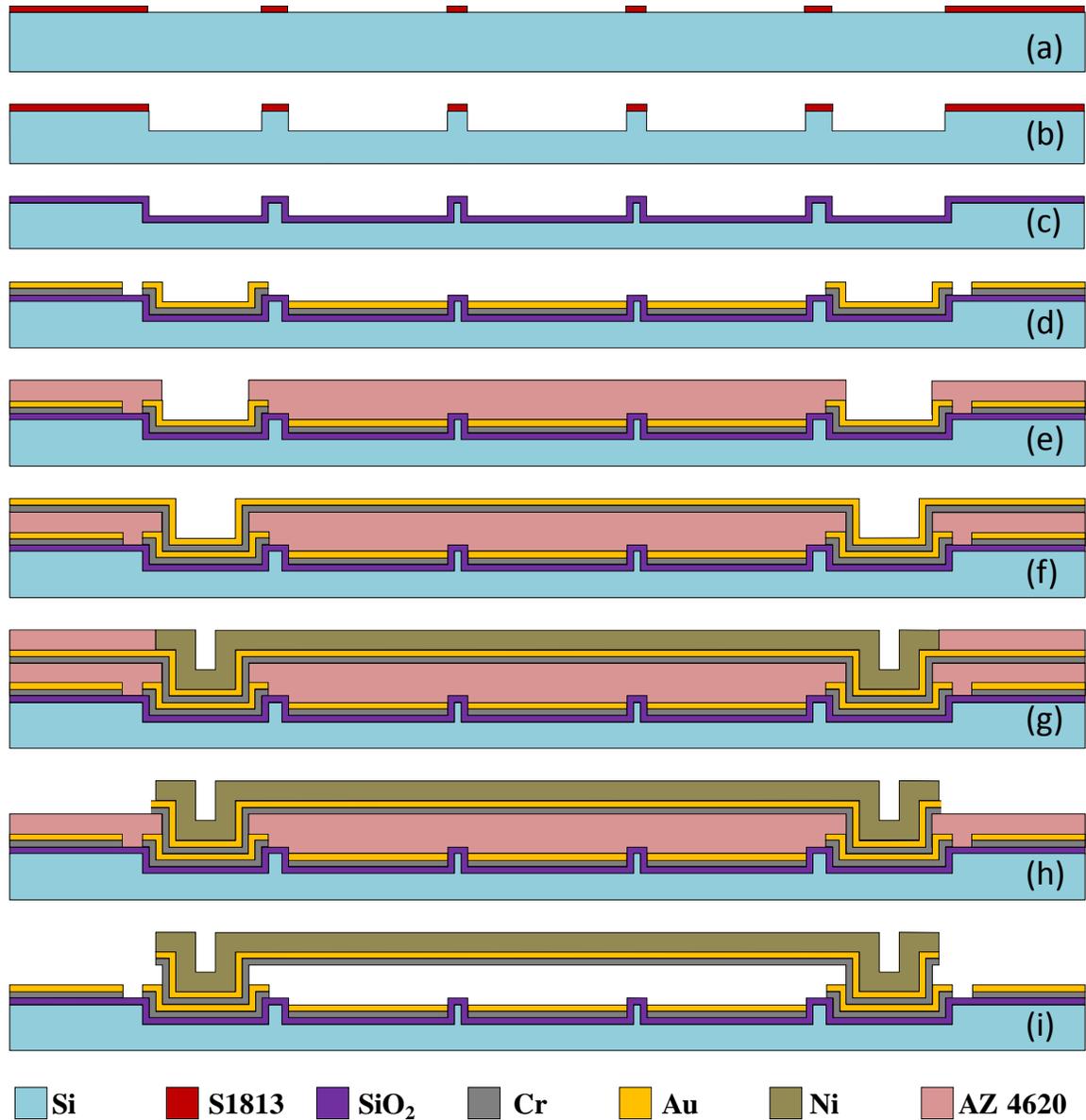


Figure 3.14. Schematics of the variable capacitor fabrication process on Si substrate by surface micromachining.

piranha solution reacts with all organic materials on the substrate and removes them in the form of CO₂ gas and water vapor. The substrate is then rinsed thoroughly with DI water and dried with nitrogen blower. The fabrication facility has ELGA DI water system capable of maintaining 18 MΩ resistance at of water.

(2) A thin layer of Shipley S1813 photoresist is spin coated at 3000 rpm for 30 seconds with an acceleration of 500 rpm/sec. The photoresist is then soft baked on a hot plate for 2 min at 90 °C and and patterned using MA6 mask aligner to form square shaped stoppers and trenches at locations corresponding to the anchor's locations. The photoresist is then developed in MF319 developer (Figure 3.14 (a)).

(3) The Si substrate is etched in order to form stoppers and anchor holes using Reactive Ion Etching system (RIE) and the photoresist is cleaned with acetone and IPA and piranha solution (Figure 3.14 (b)). (4) The wafers are thermally oxidized (Figure 3.14 (c)) in a furnace to form a 1 μm thick SiO₂ film for better electrical isolation between separate devices and also between the electrodes of the same device (Figure 3.15).

(5) Then Cr and Au layers were deposited for thicknesses of 50 nm and 150 nm respectively on the SiO₂ surface by DC sputtering. A base pressure of 7×10^{-7} Torr can be reached with the cryogenic vacuum pump (cryopump) and deposition pressure was kept around 5 mTorr by flowing argon (Ar) gas into the vacuum chamber during the process. The deposition power for Cr and Au are 200 W and 90 W respectively. The deposition time is determined for the preferred thicknesses. The calibrated deposition times in the process chamber are 5 min and 6 min for Cr and Au respectively. (6) The Au layer is patterned to form the bottom plate, bonding pads and trace lines. (Figure 3.14 (d)). A thin

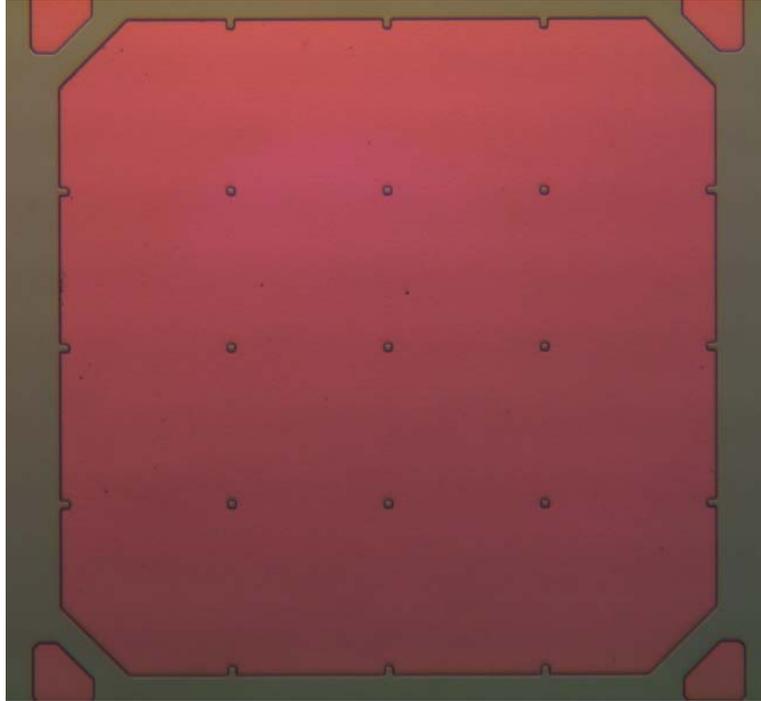


Figure 3.15. Magnified view of the substrate after oxidation.

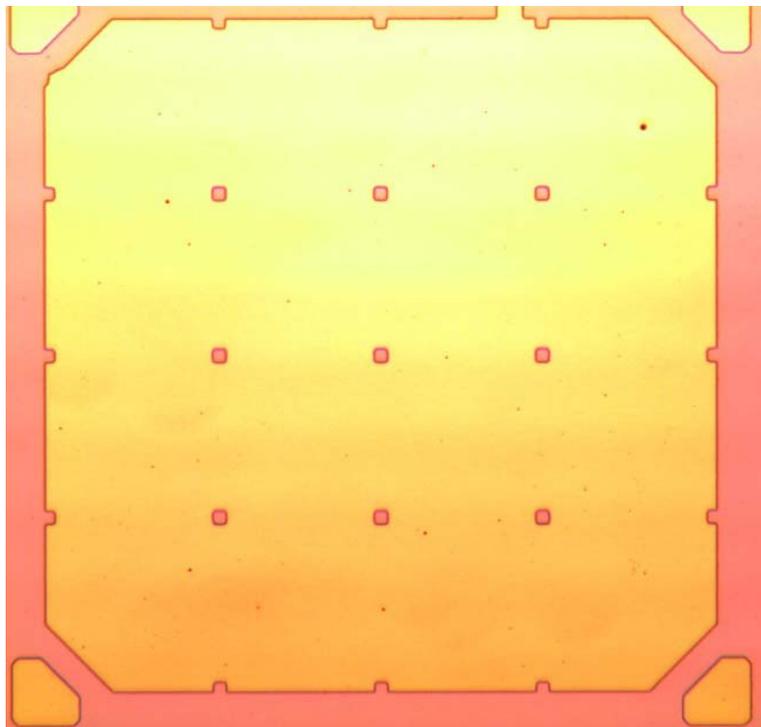


Figure 3.16. Magnified view of the substrate after gold patterning.

layer of Shipley S1813 photoresist is spin coated and patterned using Mask II. Gold layer is etched in potassium iodide (KI) solution. After the gold etching, the photoresist is cleaned with acetone and IPA. The optical microscopic view of the substrate after gold patterning is shown in Figure 3.16.

(7) The first mold for creating the anchors is prepared with a 10 μm thick layer of AZ P4620 photoresist (Figure 3.14 (e)). The same photoresist layer will serve as a sacrificial layer for suspending the power harvester after fabrication. A thick photoresist sacrificial layer was spin coated at 1800 rpm for a height of 10 μm and soft baked at 110 $^{\circ}\text{C}$ for 2 min. After UV exposure, the photoresist is developed in 1:3 ratio of AZ 400K developer : DI water solution. This sacrificial layer serves as a mold for creating the capacitor moving plate anchors. An optical microscope image of the substrate with photoresist mold is shown in Figure 3.17

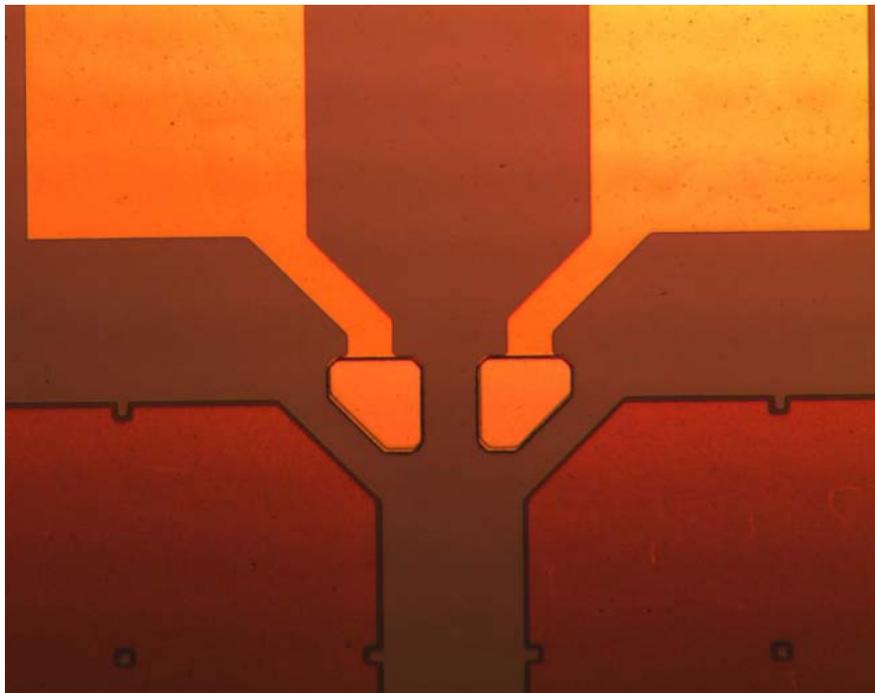


Figure 3.17. An optical image of the photoresist mold for the anchors before hard baking.

(8) The photoresist sacrificial layer is cured in a convection oven with an optimized temperature 120 °C for 90 minutes (Figure 3.18). This step is necessary to prevent cracks or wavy patterns on the sacrificial layer after sputter deposition. (9) Another Cr/Au seed layer is deposited by DC sputtering on the sacrificial layer (Figure 3.14 (f)). (10) A second photoresist mold was patterned on top of the second seed layer to create the top movable plate along with the suspension beams (Figure 3.14 (g)). The mold was then patterned to provide the movable plates with square holes (Figure 3.19). This will simplify the removal of the photoresist sacrificial layer and reduce the damping factor due to squeeze film effect. (11) The movable plate and suspension beams are grown on the second seed layer by electroplating Ni for a thickness of 10 μm (Figure 3.14 (g)). This allows us to fabricate conductive anchors and plate with large mass. The plate is grown with holes in order to facilitate releasing of the structure and also for reducing the damping factor due to squeeze film effect.

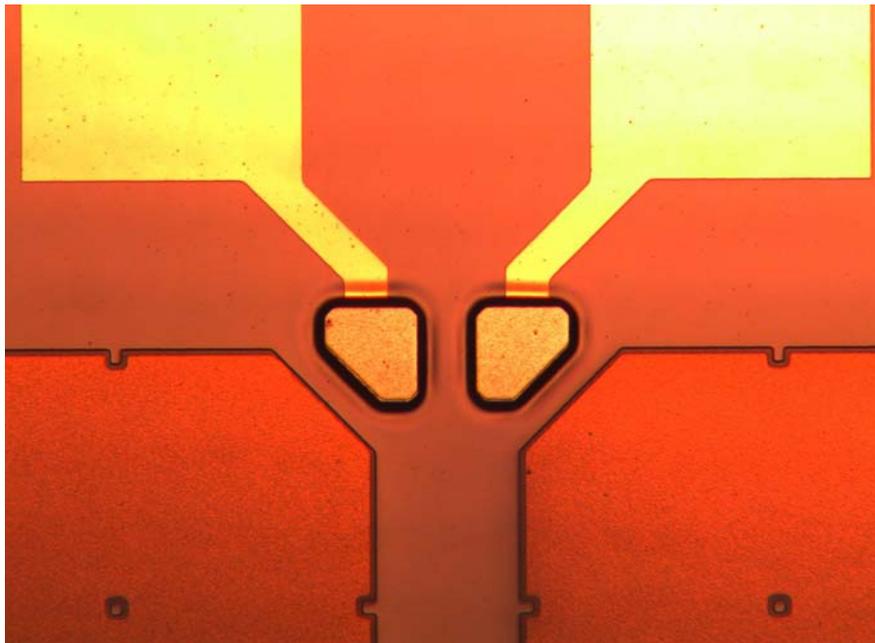


Figure 3.18. An optical image of the photoresist mold for the anchors after hard baking.

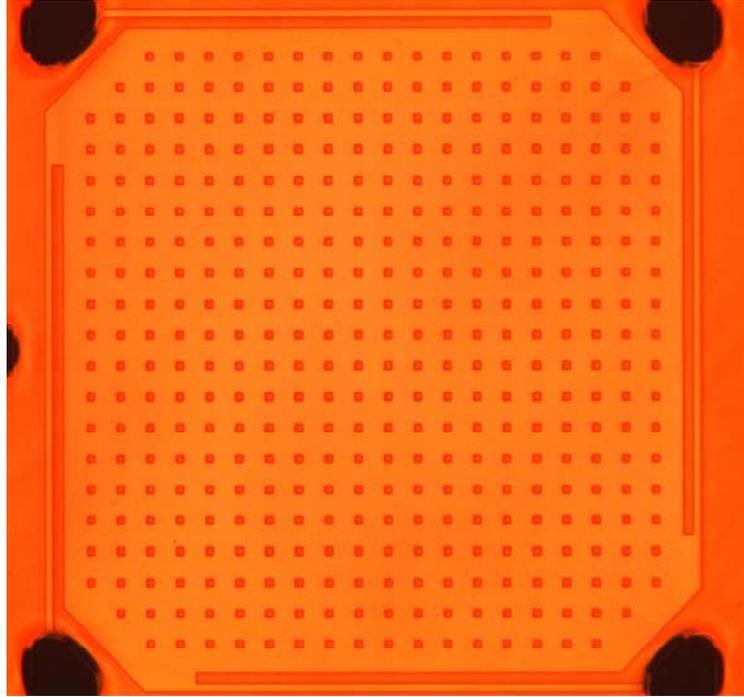


Figure 3.19. An optical image of the second photoresist mold patterned on the second seed layer.

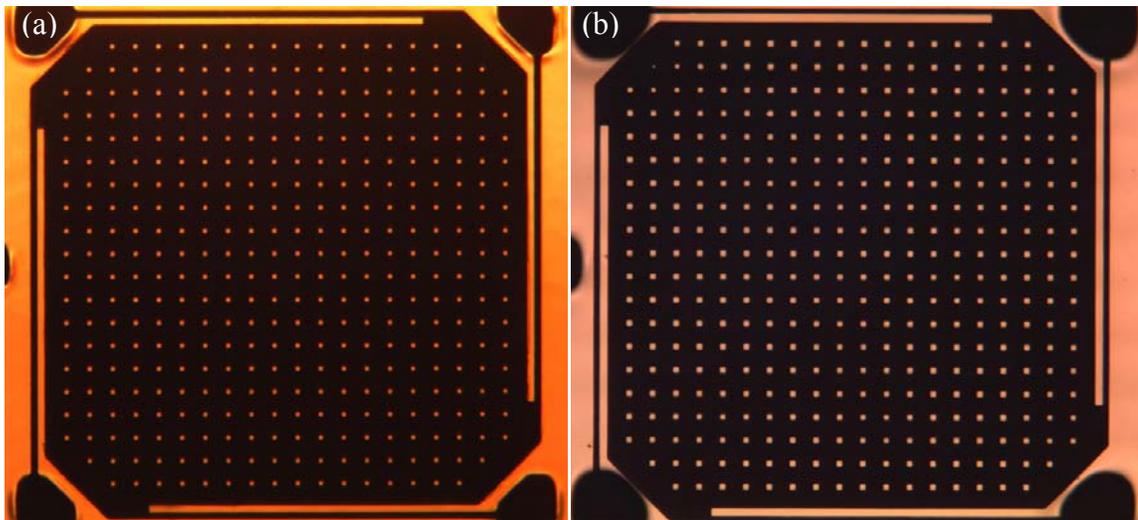


Figure 3.20. An optical image of the device a) after removing the second photoresist mold and b) after removing the Au layer. Cr layer is still noticeable under the Ni structure.

(12) After desired thickness of the material is deposited, the top mold is washed away carefully by solvents. A magnified optical microscopy image of electroplated Ni

plate after removal of photoresist mold can be seen in Figure 3.20(a). The remaining of the second seed layer is etched chemically. The photoresist mold on top of the seed layer has been removed without attacking the sacrificial layer and the seed layer is then removed by etching Au and Cr consequently (Figure 3.14 (h)).

(13) At the final step, the sacrificial layer is removed with resist stripper at 85 °C and the device is rinsed thoroughly with DI water and then set aside for air dry (Figure 3.14 (i)). The ultrasonic agitation is added to help removal of the sacrificial layer.

After releasing the suspended plate, the device is immersed in DI water to clean any residual solution (Figure 3.21). Then IPA solution is used to replace DI water from the surfaces of the device for a better control of drying with smaller surface tension. SEM micrographs of the fabricated device showed suspension of plates with flat surface (Figure 3.22).

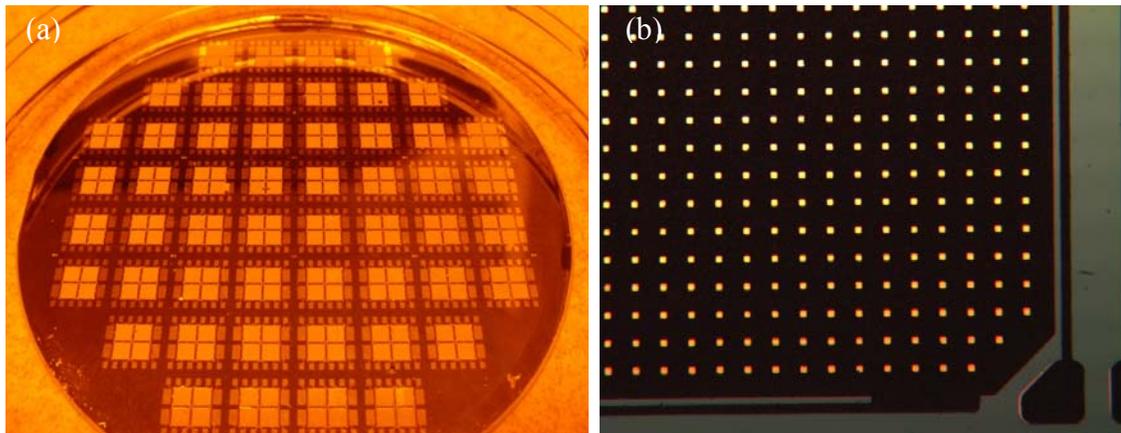


Figure 3.21. a) A Photo of the full wafer after fabrication and b) an optical microscope image of the device after removing the photoresist sacrificial layer.

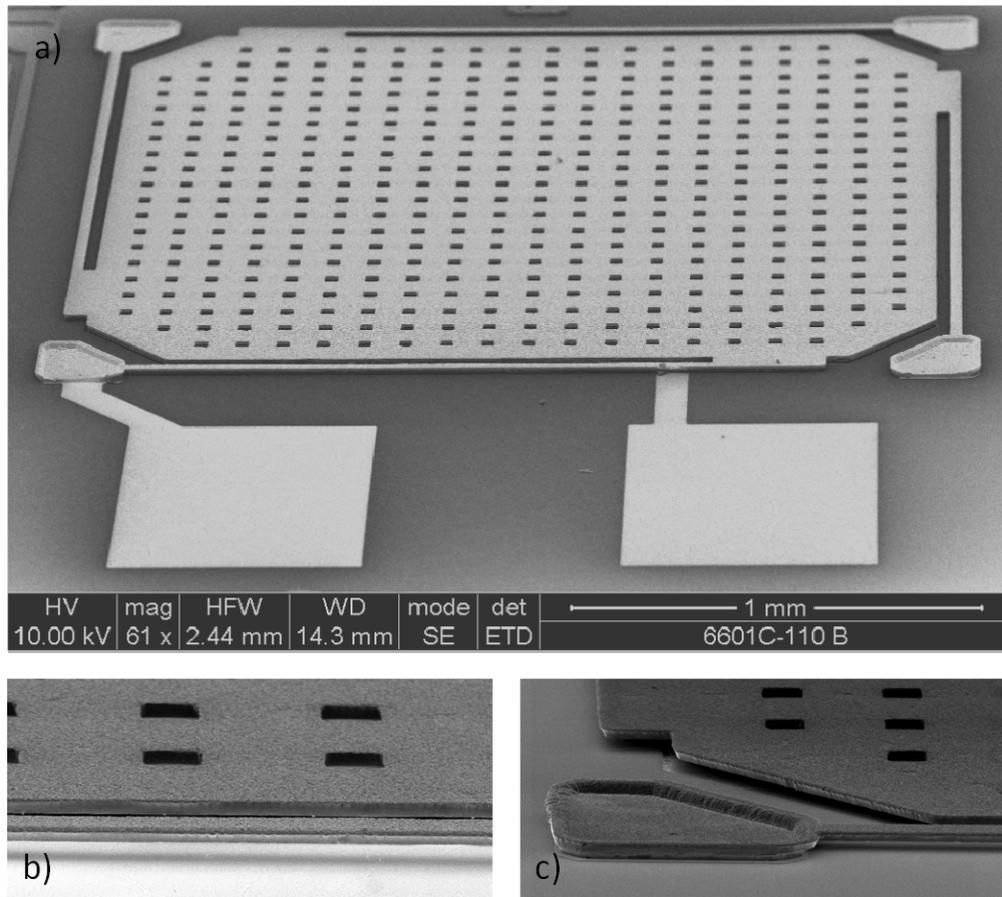


Figure 3.22. The SEM micrographs of MEMS capacitor with the lower cavity part, a) full device, b) magnified view of the movable plate side, c) anchor and suspension beams.

To create the top cavity, the second silicon substrate only with the fixed plates, stoppers and Ni bonding tabs prepared using the same fabrication process as described previously.

Instead of using the mask of anchors and bonding tabs, the AZ-P4620 photoresist sacrificial layer is patterned to form an electroplating mold using a separate mask for bonding tabs. The bonding tabs are similarly formed by electroplating Ni for a thickness of 30 μm inside the mold. In addition, a thin layer of indium (In) about 1 μm is electroplated on top of the bonding tabs. The side view of the substrate is shown in

Figure 3.23 is used to create the top capacitive cavity. (1) Stoppers and electrodes are fabricated using the same process of the bottom cavity (Figure 3.23 (a)-(e)). The Cr layer is kept for electrical connection to the seed layers. (2) A 30 μm photoresist mold for Ni pillars is spin coated and patterned on the sample by double coating (Figure 3.23 (f)).

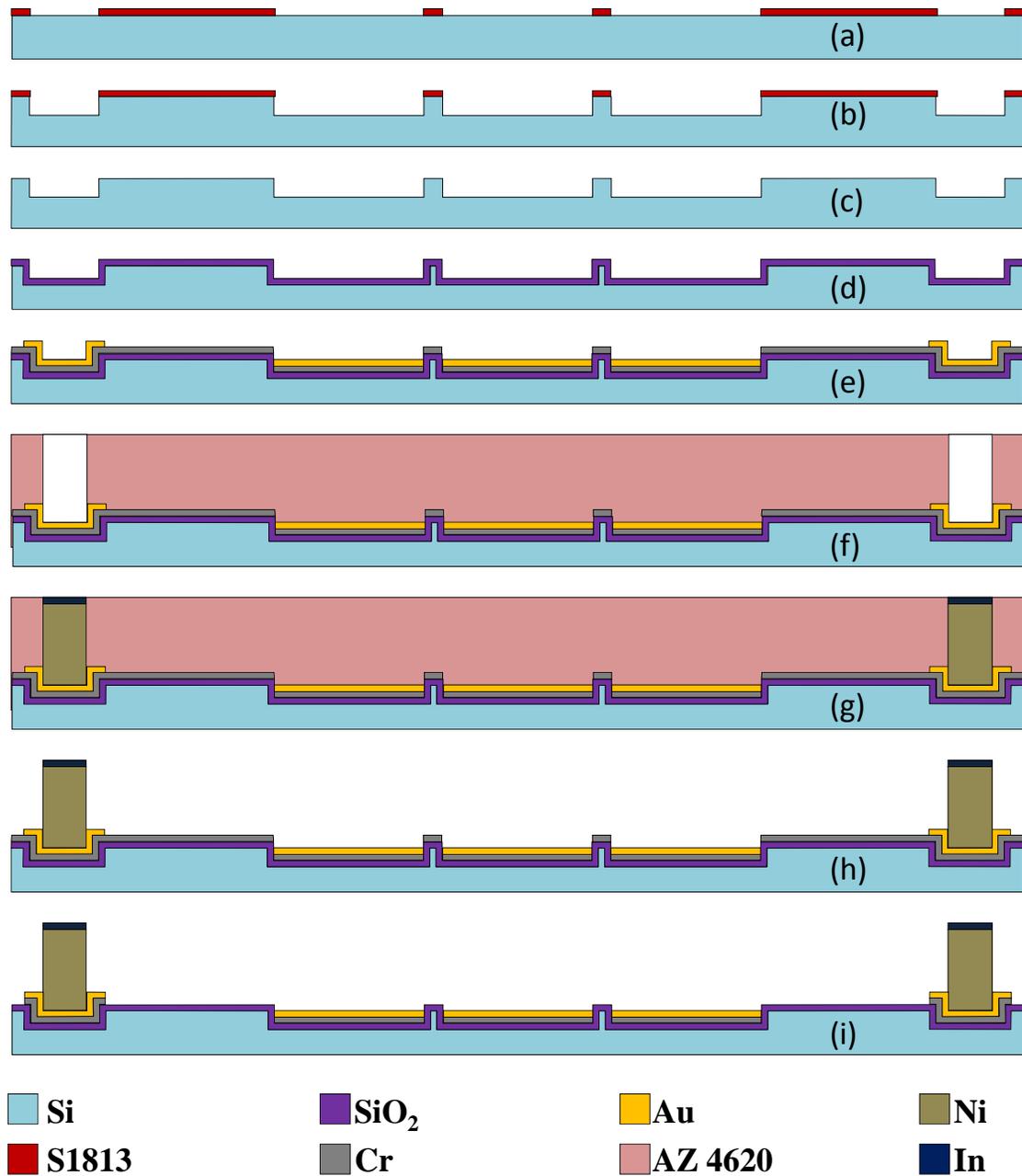


Figure 3.23. Side view schematics of the top cavity fabrication process for Si substrate.

(3) Nickel bonding tabs with a thickness of $30\ \mu\text{m}$ are grown by electroplating Ni. (Figure 3.23 (g)) The growth rate control of the Ni plating allows us to adjust the height of the second cavity. (4) A layer of indium (In) is deposited ($\sim 1\ \mu\text{m}$) using In electroplating (Figure 3.23 (g)) The indium layer is used as the electrical and mechanical bonding material for the final device. (5) Finally the mold is removed (Figure 3.23 (h)) and Cr layer is etched by wet etching to isolate all the devices on the substrate (Figure 3.23 (i)).

The two substrates were dices into small dies, each containing four devices. The bonding tabs on the two substrates were then aligned under the microscope and fixed together by applying a small physical pressure (Figure 3.24). Then they were heated to $150\ ^\circ\text{C}$ in order to soften the indium layers and form a strong bond between them and then cooled down (Figure 3.25).

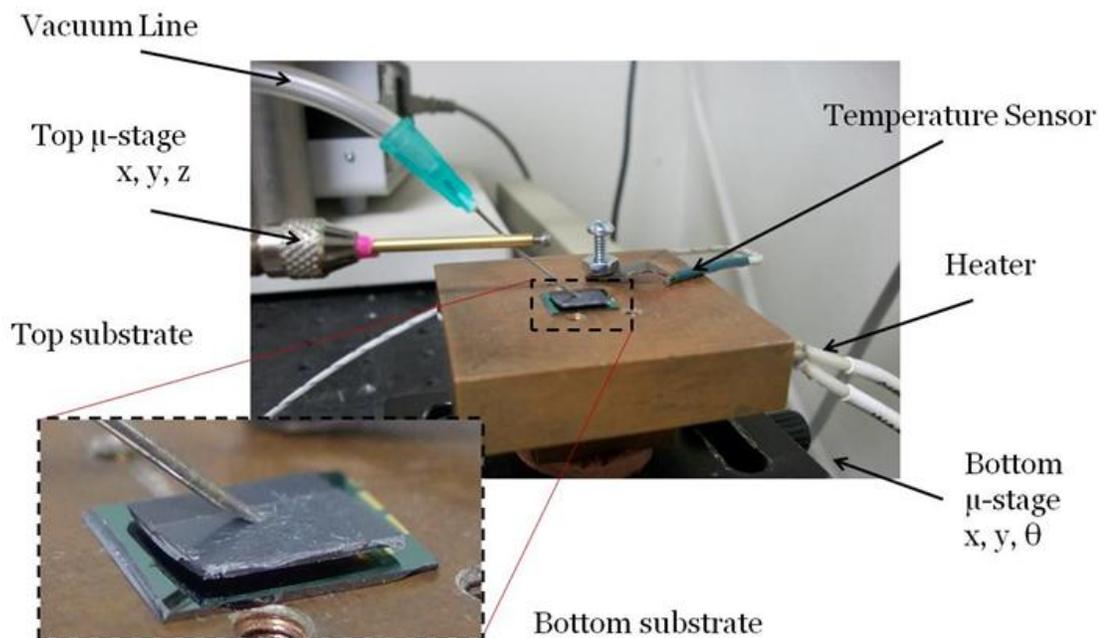


Figure 3.24. Photo of the experimental setup to bond the two substrates together to form the two cavity MEMS device.

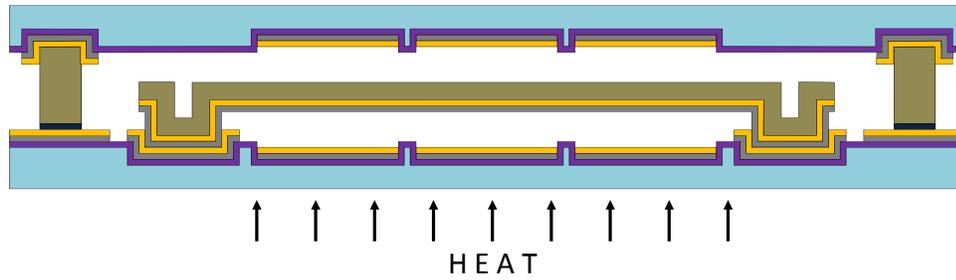


Figure 3.25. A Schematic of the bonding process to form the two cavity MEMS power harvester.

SEM micrographs of the successfully fabricated and bonded devices show that a good control on the fabrication of two cavity MEMS capacitor is possible with the control of Ni growth thickness and control on the sacrificial layer thickness (Figure 3.26).

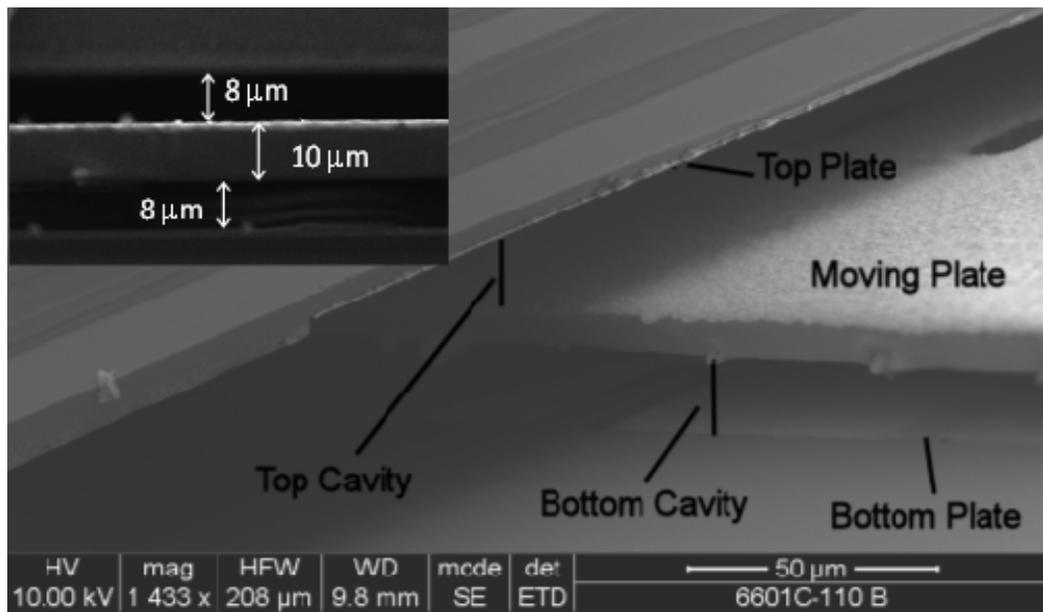


Figure 3.26. An SEM micrograph of two cavity device after bonding. Isometric view SEM micrographs is taken to show the two cavities. The inset shows the front view of the device.

3.2.3 Mask Fabrication for Glass Substrate

Photomask layouts were drawn in L-Edit Layout Editor software from Tanner, as shown in Figure 3.27 and fabricated using the same procedure outlined above. The fabrication of the single cavity MEMS capacitor device requires at four masks (Table 5)

- 1) The first mask I is used to pattern fixed plates, electrodes and trace lines.
- 2) The second mask II is used to pattern the dielectric layer via lift off.
- 3) The third mask III is used to pattern the mold for electroplating pillars for anchors.
- 4) The fourth mask IV is used for electroplating the movable plate.

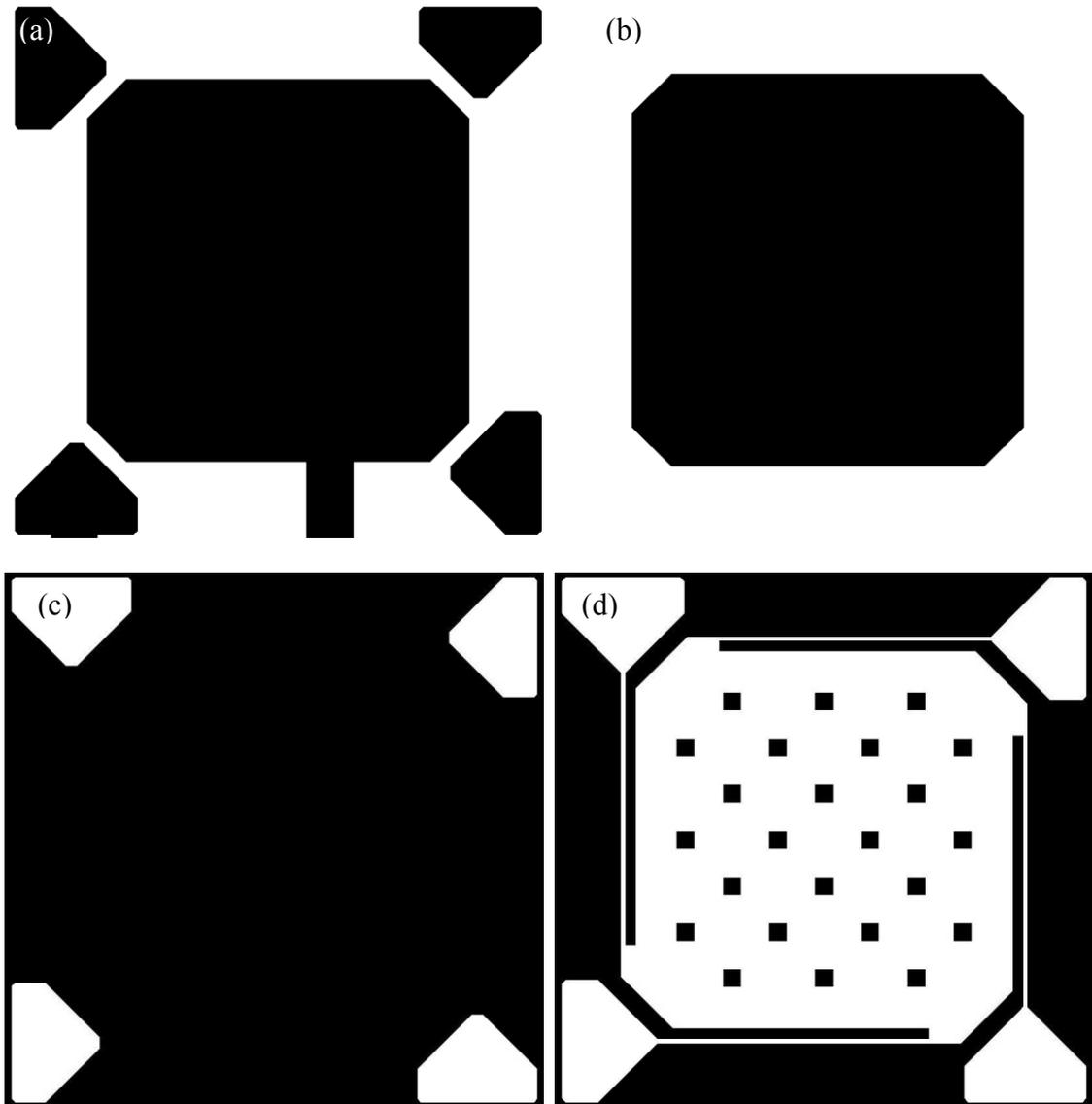


Figure 3.27. a) The layout of Mask I for bottom electrodes, bonding pads and anchor bases, b) The layout of Mask II for dielectric layer. c) the layout of Mask III for anchor holes, d) the layout of Mask IV for plates and suspension beams

Table 5. The masks set used in the fabrication process of MEMS variable capacitors on Si substrate.

	Name	Descriptions
The mask I	Bottom Electrodes mask	To create the patterns of fixed plates, electrodes, trace lines, and the seed layers of anchors and bonding tabs
The mask II	Dielectric mask	To pattern the dielectric layers
The mask III	Anchor Holes mask	To create the photoresist mold for electroplating the anchors
The mask IV	Movable Plate mask	To create the photoresist mold for electroplating the movable plate and anchors with suspension beams

3.2.4 Device Fabrication on Glass Substrate

The MEMS capacitors were fabricated successfully using surface micromachining technologies by the following sequence on top of a substrate. (1) The glass substrate is cleaned using piranha solution for 3 minutes. The substrate is then rinsed thoroughly with DI water and dried with nitrogen blower. (2) Cr and Au layers are sputter-deposited and patterned with thicknesses of 50 nm and 150 nm, respectively (Figure 3.28 (a) and (b)). (3) Au layer is etched (Figure 3.28 (c)). After the Au etching, the photoresist is removed (Figure 3.29 (b)), and Cr layer is etched chemically (Figure 3.30). Cr layer serves as the adhesion layer between gold layer and the glass surface (See Figure 3.28 (d)).

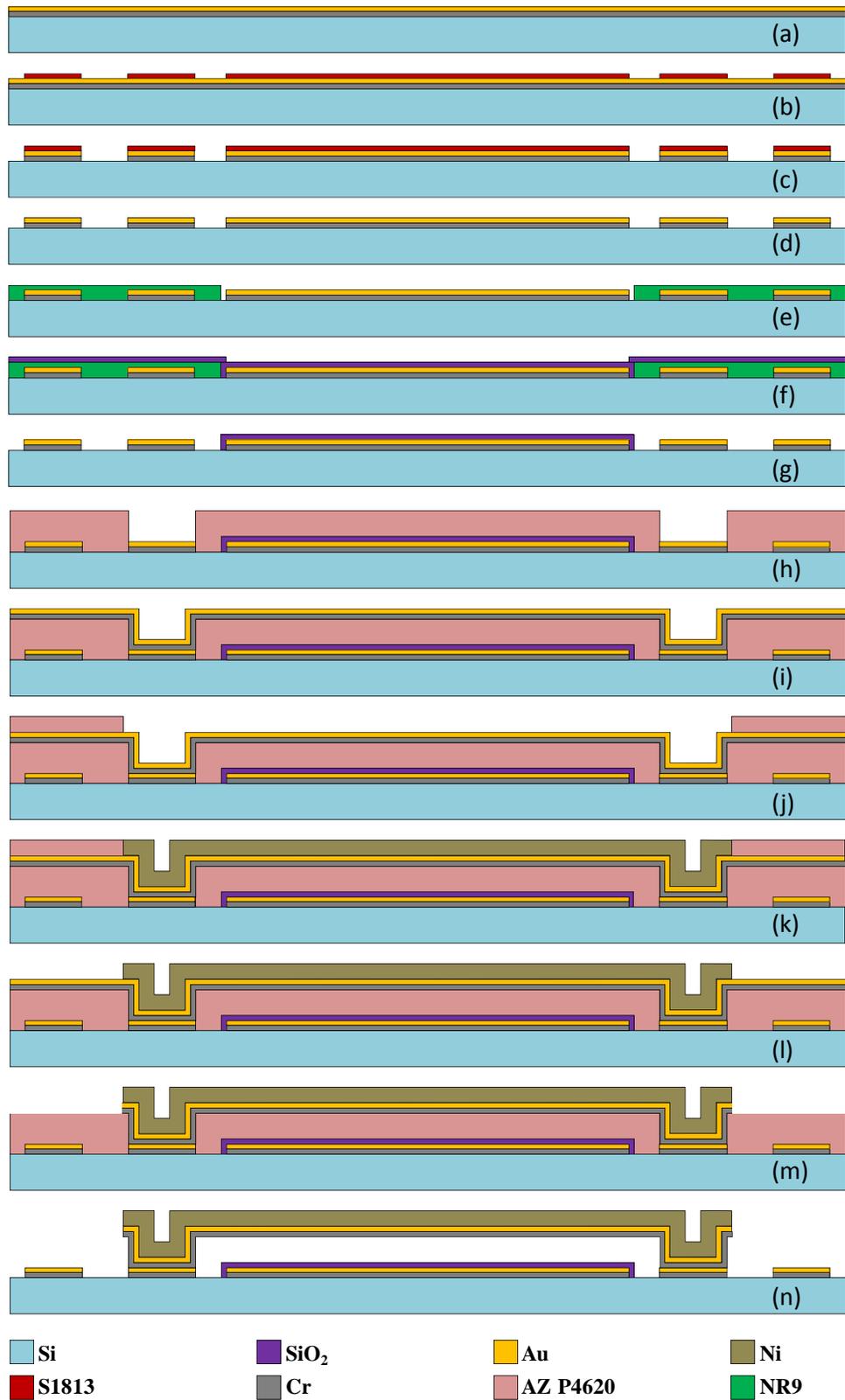


Figure 3.28. Schematics of the MEMS variable capacitor fabrication process on a glass substrate.

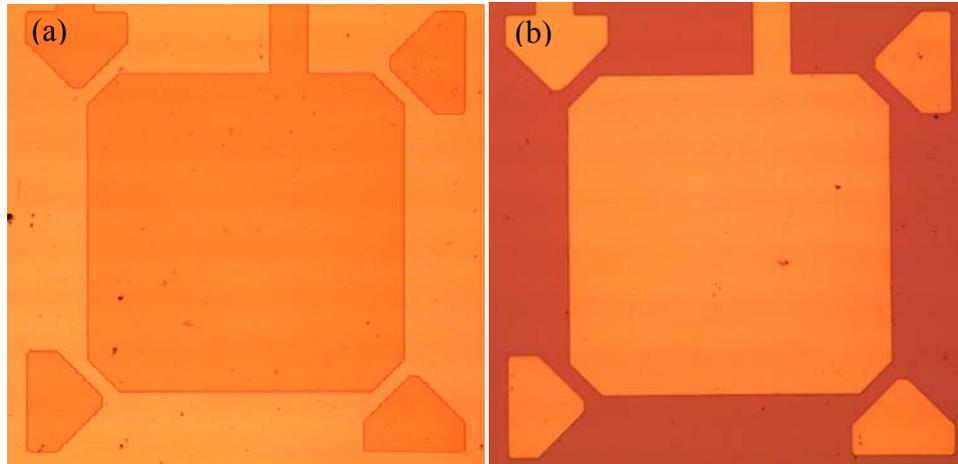


Figure 3.29. An optical image of the substrate a) after developing photoresist b) after gold etching.

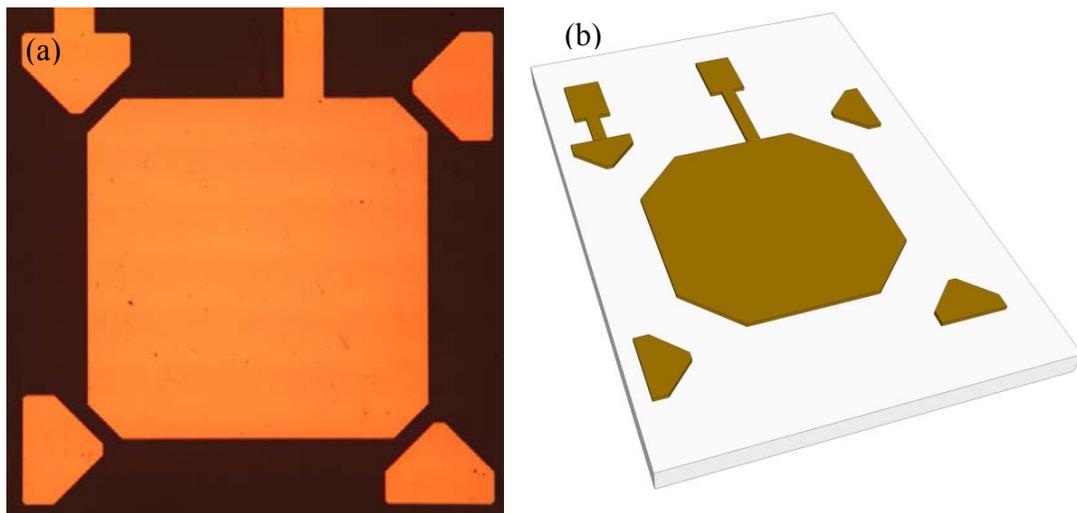


Figure 3.30. An optical image of the substrate after etching Cr and Au layers.

(4) A thin layer of NR-9 3000PY negative photoresist is spin coated at 4000 rpm for 30 seconds with an acceleration of 500 rpm/sec. The photoresist is soft baked on a hot plate for 1 min at 150 °C and then cooled down slowly and then exposed to UV light. The photoresist is post exposure baked on a hot plate for 1 min at 100 °C and then cooled down slowly and developed in MF319 developer (Figure 3.31). This step is used for patterning the SiO₂ dielectric layer using lift-off process (Figure 3.28 (e)).

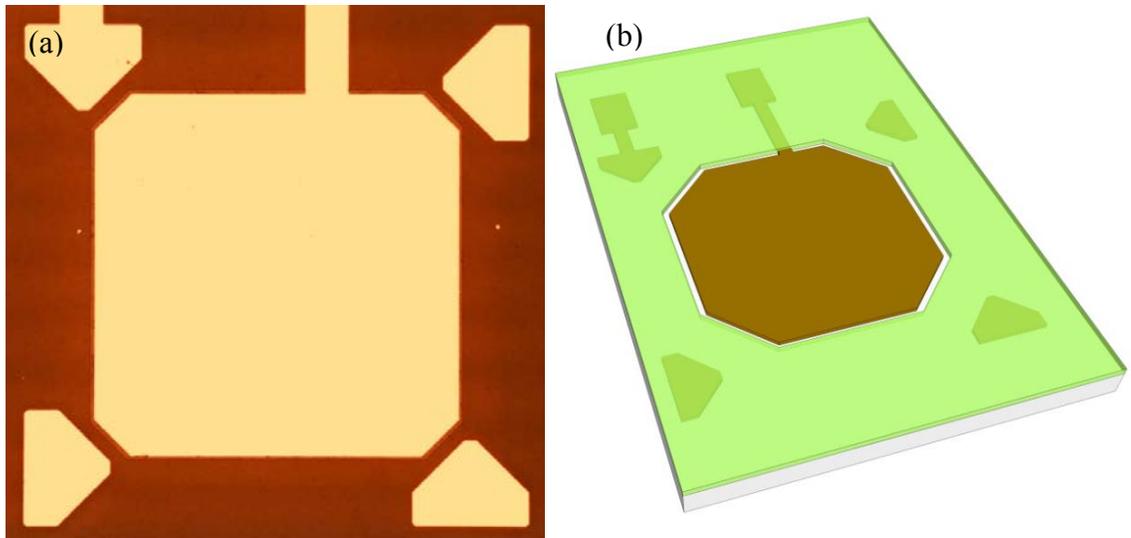


Figure 3.31. An optical image and 3D drawing of the substrate after developing NR-9 3000 PY photoresist layer. Photoresist is everywhere except the plate area.

(5) SiO_2 dielectric film is deposited for thicknesses of 200 nm on the surface by RF sputtering (Figure 3.28 (f)). The process power was 200 W and the film was deposited in multiple steps of 20 minutes. (6) The substrate was inserted in an acetone bath in ultrasound agitation to lift off the SiO_2 film (Figure 3.28 (g)). Optical image of the magnified view of the device area after lift-off process can be seen in Figure 3.32.

(7) The first mold for the anchors was prepared with a 10 μm thick layer of AZ P4620 photoresist (Figure 3.28 (h)). The same photoresist layer functions as a sacrificial layer. It was spin-coated at 1800 rpm for a height of 10 μm and soft baked at 110 $^\circ\text{C}$ for 2 min. After exposure under UV light, the photoresist is developed in 1:3 ratio of AZ 400K developer : DI water solution. This sacrificial layer serves as a mold for creating the capacitor moving plate anchors. The optical microscope image of the substrate with photoresist mold is shown in Figure 3.33. (8) The photoresist sacrificial layer is cured in a convection oven with an optimized temperature 120 $^\circ\text{C}$ for 90 minutes and followed by

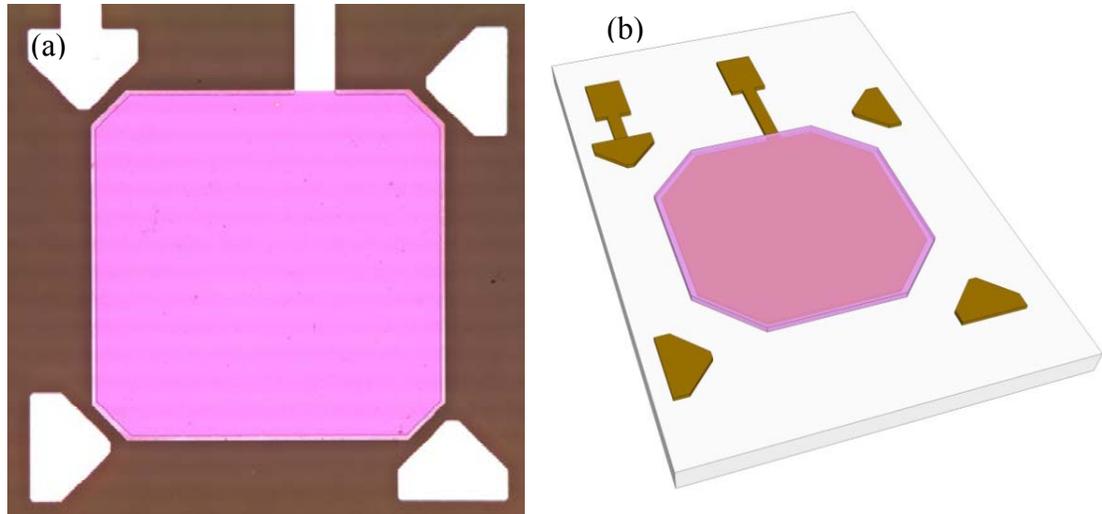


Figure 3.32. An optical image of the device area after lift-off process and 3D drawing of the device at this stage.

the deposition of another Cr/Au seed layer (Figure 3.34). (9) A second photoresist mold was patterned on top of the second seed layer to create the top movable plate along with the suspension beams (Figure 3.28 (j)). The mold was then patterned to provide the movable plates with square holes (Figure 3.35).

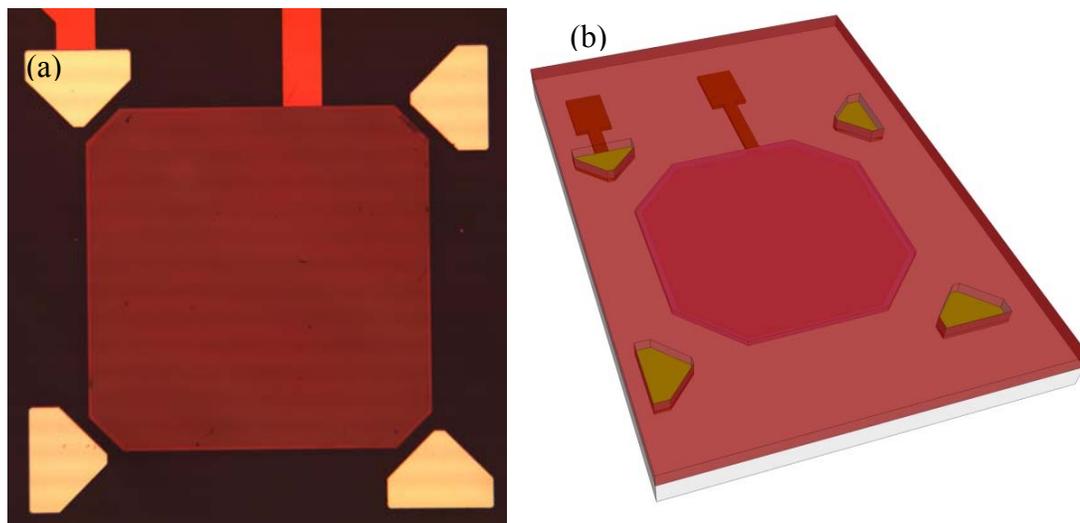


Figure 3.33. An optical image of the photoresist mold for the anchors and 3D drawing of the device at this stage.

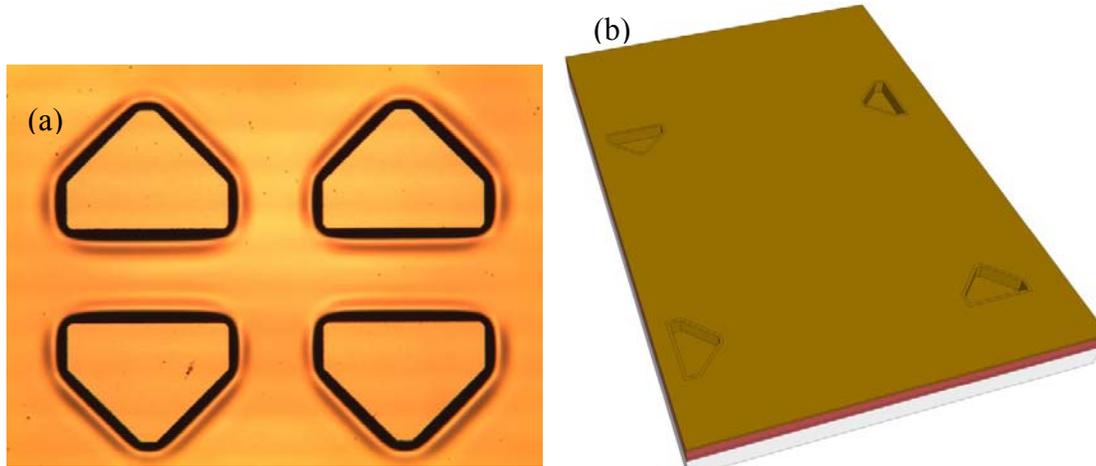


Figure 3.34. An optical image with a magnified view of the anchor area after Cr/Au deposition on the cured first mold and 3D drawing of the device at this stage.

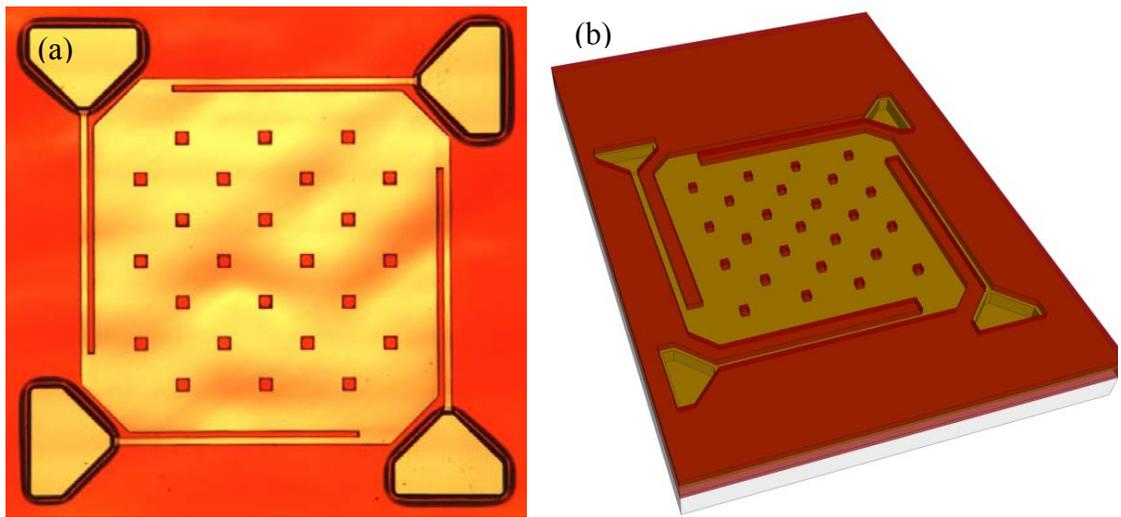


Figure 3.35 An optical image of the second mold on top of the second seed layer defining suspension beams, plate with holes and anchors and 3D drawing of the device at this stage.

(10) The moving plate and suspension beams are grown on the second seed layer by electroplating Ni for a thickness of $10\ \mu\text{m}$ (Figure 3.28 (k)). Magnified optical microscopy image of electroplated Ni plate can be seen in (Figure 3.36). (11) After desired thickness of the material is deposited, the top mold is washed away carefully by solvents (Figure 3.28 (l)). The seed layer is then removed by etching Au (Figure 3.37 (a)) and Cr (Figure 3.37 (b)) consequently.

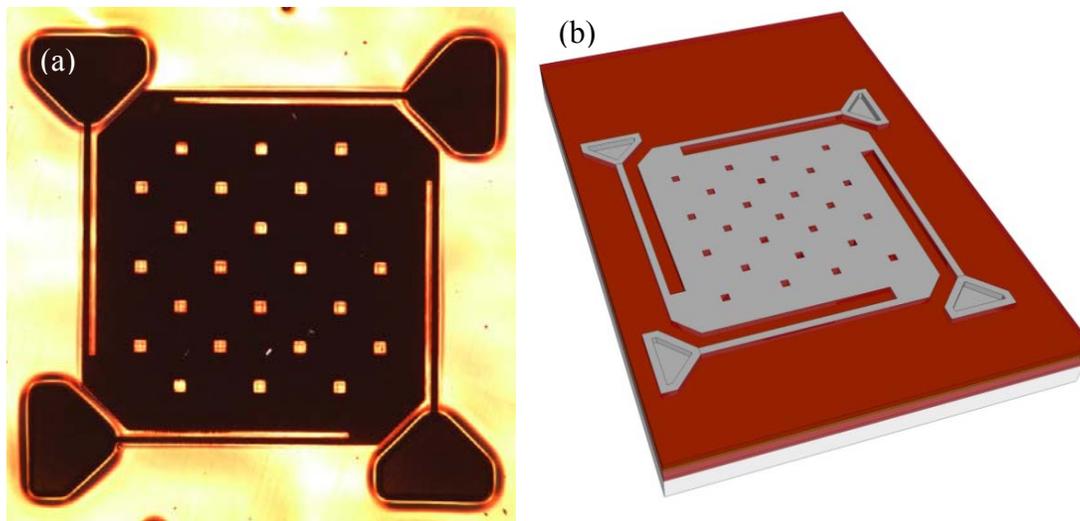


Figure 3.36. Optical image of the magnified view of the electroplated Ni into the device mold on top of the second seed layer and 3D drawing of the device at this stage.

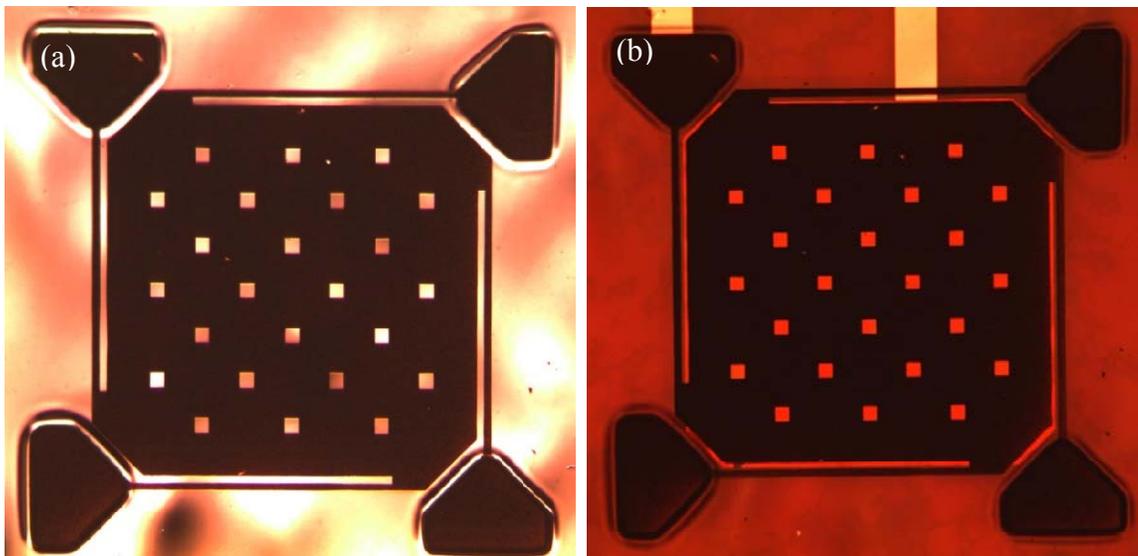


Figure 3.37. Optical image of the magnified view of the device a) after removing Au layer, after this step, Cr layer is still covering the photoresist mold b) device after removing the Cr layer. After this step, bottom electrode and trace lines can be seen through transparent photoresist layer.

(12) At the final step, the sacrificial layer is cleaned with resist stripper at 85 °C and the device is rinsed thoroughly with DI water and then set aside for air dry (Figure 3.28 (m)). The ultrasonic agitation is added to help removal of the sacrificial layer

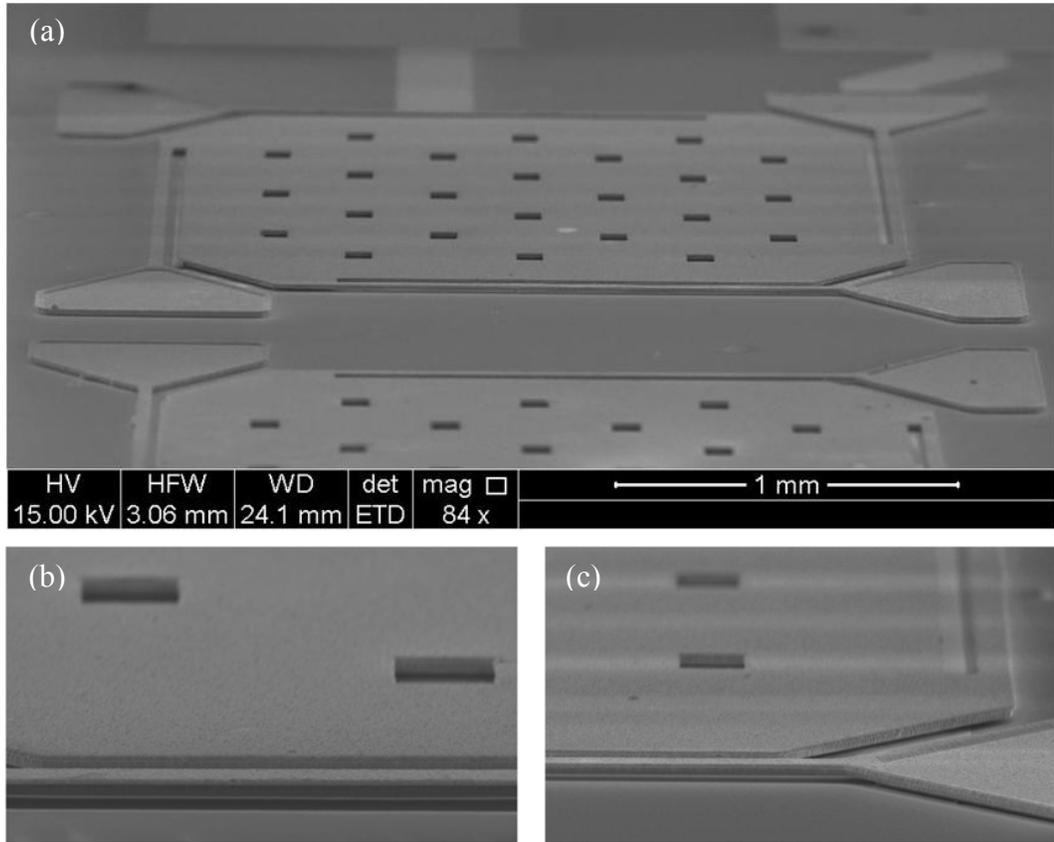


Figure 3.38. SEM micrographs of MEMS capacitor fabricated on glass substrate, a) full device, b) magnified view of the movable plate side, and c) anchor and suspension beams.

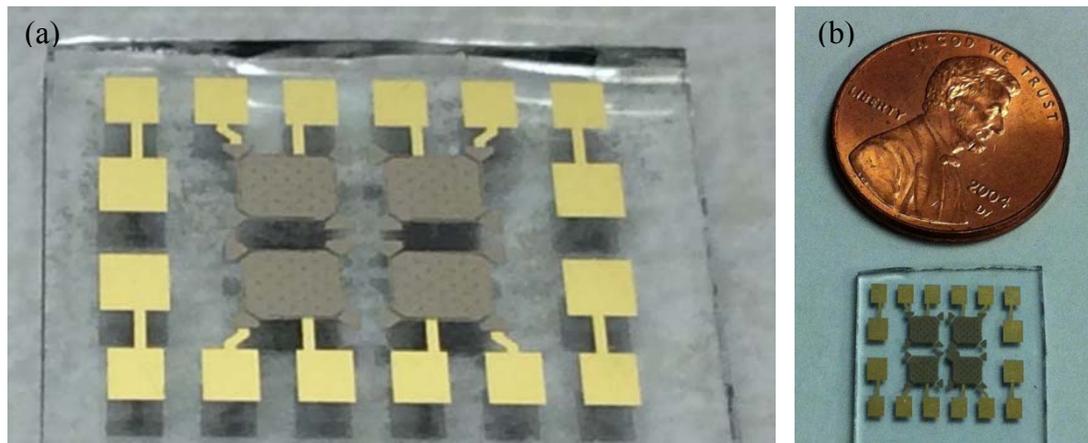


Figure 3.39. Optical images of one die with four suspended capacitive plates after dicing the substrate.

After releasing the suspended plate, the device is immersed in DI water to clean any residual solution. Then IPA solution is used to replace DI water from the surfaces of the device for a better control of drying with smaller surface tension. SEM micrographs of dried out samples showed suspension plates with flat surface (Figure 3.38). Figure 3.39 shows optical images of one die with four suspended capacitive plates after dicing the substrate.

CHAPTER 4

DEVICE CHARACTERIZATION AND DISCUSSIONS

In this chapter the experimental results, including both mechanical and electrical testing will be given and discussed for electrostatic and electromagnetic power harvesters. Measurements of the MEMS device in time and frequency domain will be presented. The measured signals in time and frequency domain will be analyzed and processed for further discussions. Experimental results, including resonance frequency, and power across the load resistors, resonance frequency shifting, under a variety of vibration conditions will be discussed. Then the results of wideband electrostatic power harvester characterization will be presented for low frequency response. Finally, wideband electromagnetic power harvesters will be characterized for different excitation conditions.

4.1 Mechanical Testing of the Fabricated Single Cavity Power Harvester

After completing the fabrication, the device was placed on the shaker (TMS K2007E1) driven by a sine wave generator and the motion of the plate was observed under a large working distance microscope (Figure 4.1). The operating frequency of the shaker was swept from 550 Hz to 650 Hz with 5 Hz increments and a digital overlay image for each individual operating frequency was recorded by a digital camera (Figure 4.2). When the displacement versus frequency graph was plotted, resonance behavior can be seen clearly (Figure 4.3).

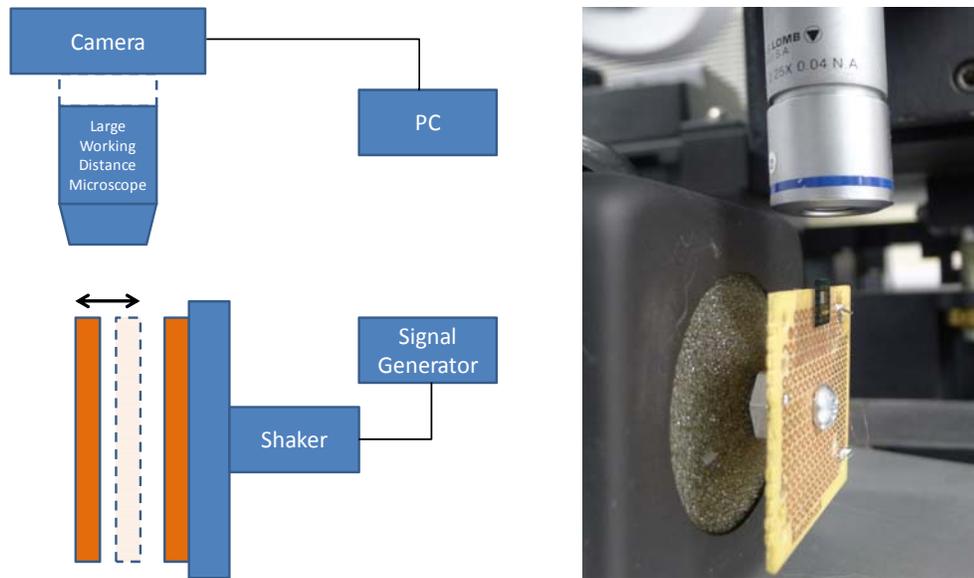


Figure 4.1. Mechanical testing setup: MEMS capacitor was placed on the shaker driven by a sine wave generator. The shaker was placed under a large working distance microscope. Digital camera on the microscope was connected to a PC.

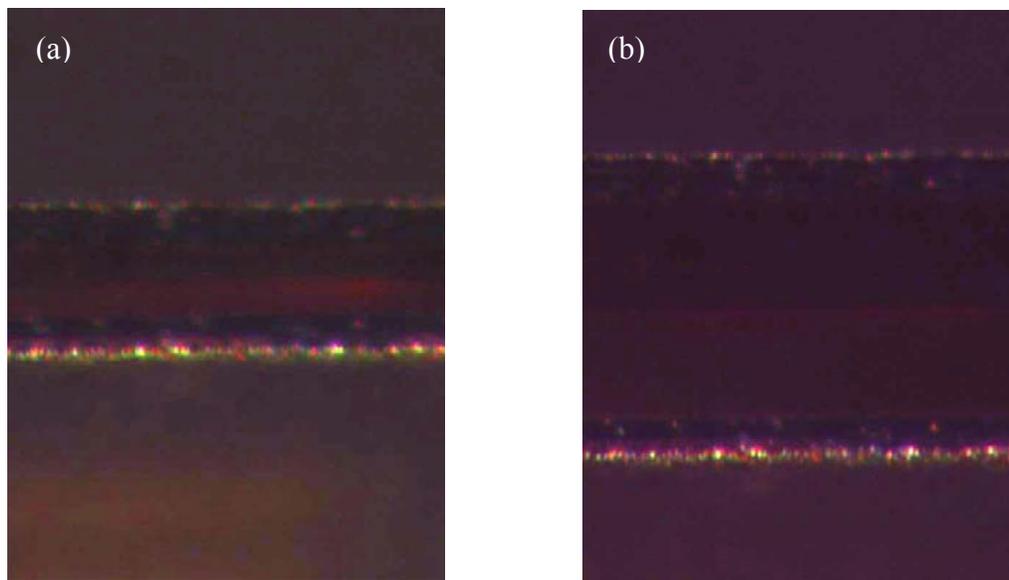


Figure 4.2. Overlay image of the moving plate side view under different excitation frequencies a) far from b) near the resonance frequency of the suspended plate. Plate motion can be clearly observed on the overlay images for different amplitudes.

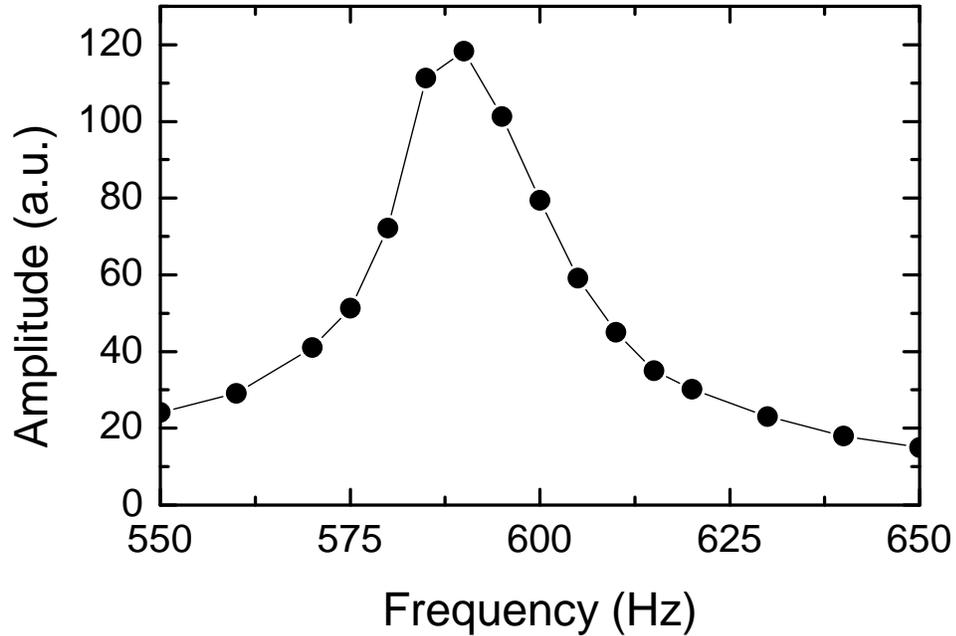


Figure 4.3. Plate displacement values for different excitation frequencies.

4.2 Electrical Testing of the Fabricated Single Cavity Power Harvester

4.2.1 MEMS Power Harvesting Device Characterization

The device was fixed on PCB board, and the connections wiring were made manually using gold wires and indium bits. The PCB was placed on the shaker driven by a sine wave generator. The capacitor on the PCB was then connected to the testing circuit in series with a load resistor to measure the voltage during the motion of the plate. The current flowing through the capacitor was observed by the voltage across the load resistor (Figure 4.4). The shaker was operated in a frequency range and the voltage across the load resistor was measured by oscilloscope and spectrum analyzer.

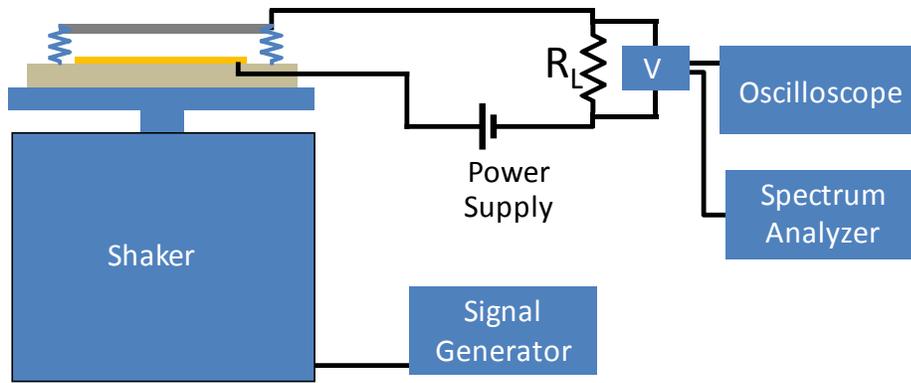


Figure 4.4. Electrical testing setup: MEMS capacitor was placed on the shaker driven by a sine wave generator. The electrodes were connected to the testing circuit. The oscilloscope and spectrum analyzer were connected to a PC via GPIB ports.

The capacitance of the MEMS variable capacitor device was measured for different physical gap values. The moving plate was forced to a position with a micro probe positioned and the capacitance was measured with a capacitance meter. From the theoretical fit to the capacitance graph, a parasitic capacitance value of 1.78 pF was determined (Figure 4.5). This measurement also indicated that the capacitance value of the device varies from around 3 pF to 9 pF during the harmonic motion.

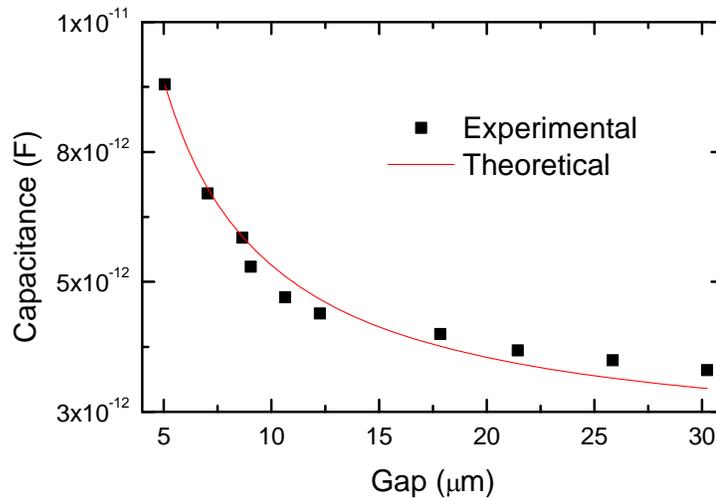


Figure 4.5. Measured capacitance values for different gaps. The solid curve represents theoretical fit for parallel plate approximation with a parasitic capacitance of 1.78 pF.

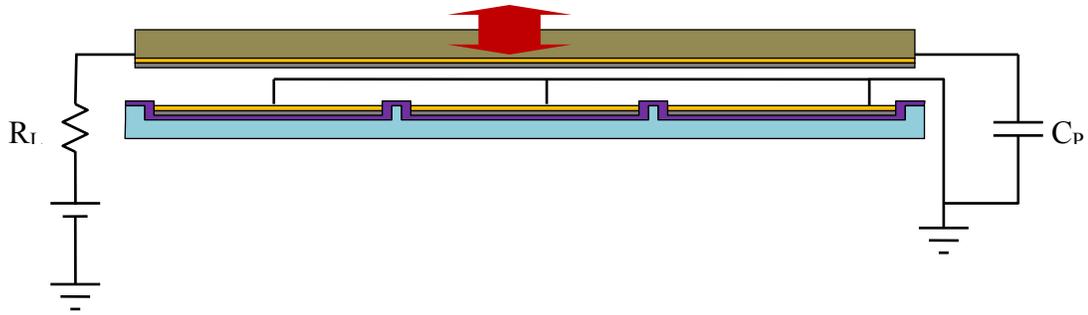


Figure 4.6. The resulting electrical circuit after combining the parasitic capacitance and load resistor for output voltage measurements.

In order to test the device in electrical domain, the PCB board with the device on it was mounted on the mechanical shaker that is operated by a constant AC voltage supplied within a frequency range from 250 to 1500 Hz. While tuning the operating frequency, the rms output voltage was measured and the data is acquired by a LabVIEW program. The resonance behavior of the moving plate can be seen clearly on the frequency distribution graph in Figure 4.7 and the results show a natural frequency of vibration at 605 Hz. The measured resonance frequency profile agrees with the results obtained using FEM simulation by COMSOL for a 10 μm plate and beam thickness.

The response of the plate around natural oscillation frequency was limited by squeeze film damping due to the large area and small distance between plates [87]. Hence, the response can be maximized by reducing the pressure of the working environment of the device [88]. Therefore, additional improvements can be achieved during the packaging of the device [89].

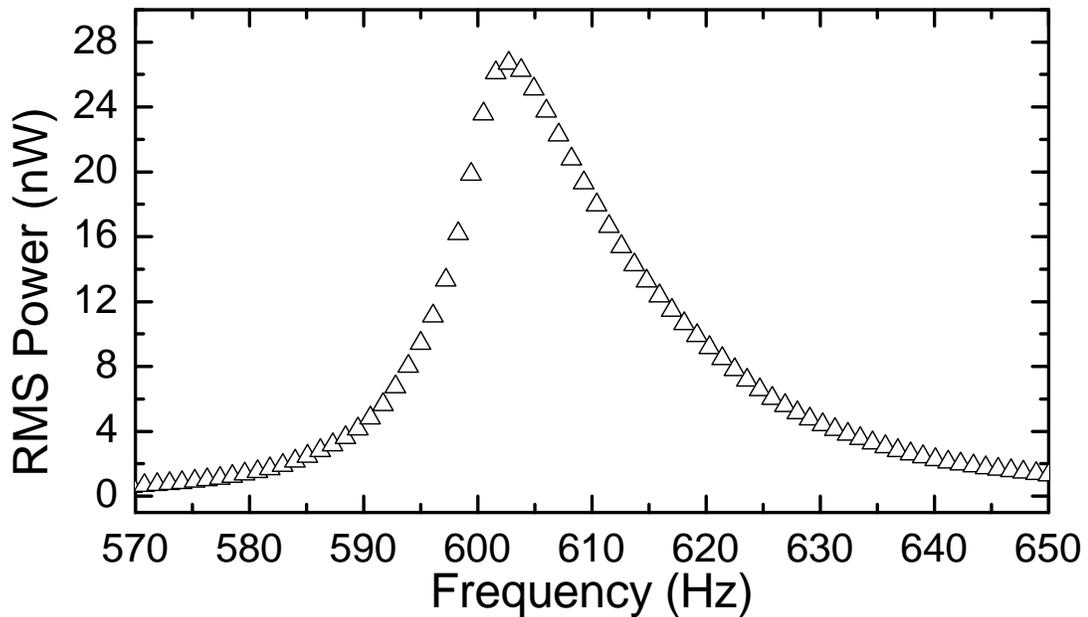


Figure 4.7. Frequency response of the moving plate measured in the electrical domain.

The voltage across the load resistor can be monitored with an oscilloscope in AC coupling mode. Figure 4.8 was recorded on a real time oscilloscope and the data was transferred into PC via a GPIB cable. The magnitude of the AC signal was determined by several factors; the applied DC voltage, external force and hence the capacitance change per unit time and the load resistor within the circuit. At small supply voltages applied to the device and small amplitudes of oscillations, the resulting output voltage curve in time domain was almost symmetric but for larger bias voltages the output voltage is larger in one direction.

The device was tested for different load resistor values. A set of resistors were connected to the circuit and under different biasing conditions the output power across the resistor was measured (Figure 4.9). For large bias voltages, the optimum load resistor was determined to be around 100 k Ω .

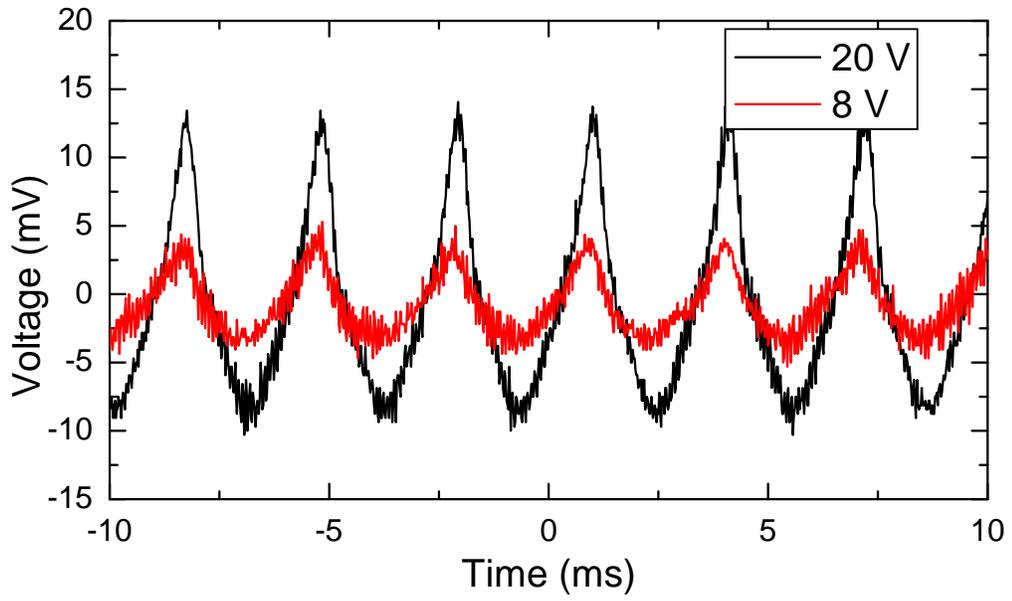


Figure 4.8. Transient behavior of the output voltage for different bias voltages from the variable capacitor for a constant shaking force.

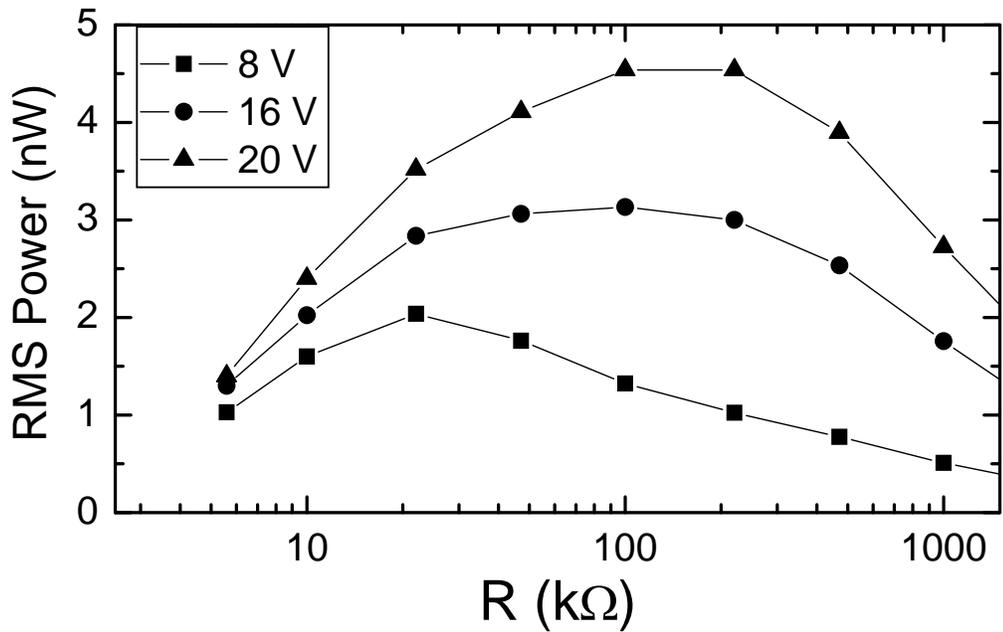


Figure 4.9. The RMS output power from the broadband electrostatic power harvester versus load resistor under 8V, 16V and 20V bias voltages.

The effect of excitation acceleration to the frequency response was also investigated.

The device was tested under different acceleration values while a constant bias voltage

was applied. A considerable amount of shift in resonance frequency was observed towards lower frequencies as the acceleration is increased (Figure 4.10). At larger accelerations, when the movable plate gets closer to the fixed plate, the electrostatic force between the two plates becomes larger and increases nonlinearly. Therefore, the electrostatic force has a softening effect because it can reduce the resonance frequency determined by the elastic suspension.

It is noted that shaking amplitude has a major effect on the mechanical behavior of the moving plate when a constant DC voltage applied to the device. As the movable plate moves close to the fixed plate due to the larger acceleration, the electrostatic force between the plates increases nonlinearly. This causes a frequency shift towards lower frequencies. Therefore, the electrostatic force has softening effect in nature. In this experiment, we experimentally investigated the nonlinear effects of acceleration to the MEMS variable capacitor by sweeping the excitation frequency around devices' resonance frequency, and in the meantime increasing the excitation acceleration. Figure 4.10 shows the output power as a function of excitation frequency within the range of 570 to 650 Hz for different excitation accelerations. It was observed that the resonance frequency decreases from approximately 612 to 603 Hz when the excitation acceleration increases from 3 to 5 g.

The input voltage supplied to the capacitor determines the amount of the charge loaded in each cycle. Hence the higher voltage applied to the capacitor leads to a higher output voltage from the device. On the other hand, bias voltage does not affect the resonance frequency of the device as it can be seen from Figure 4.11

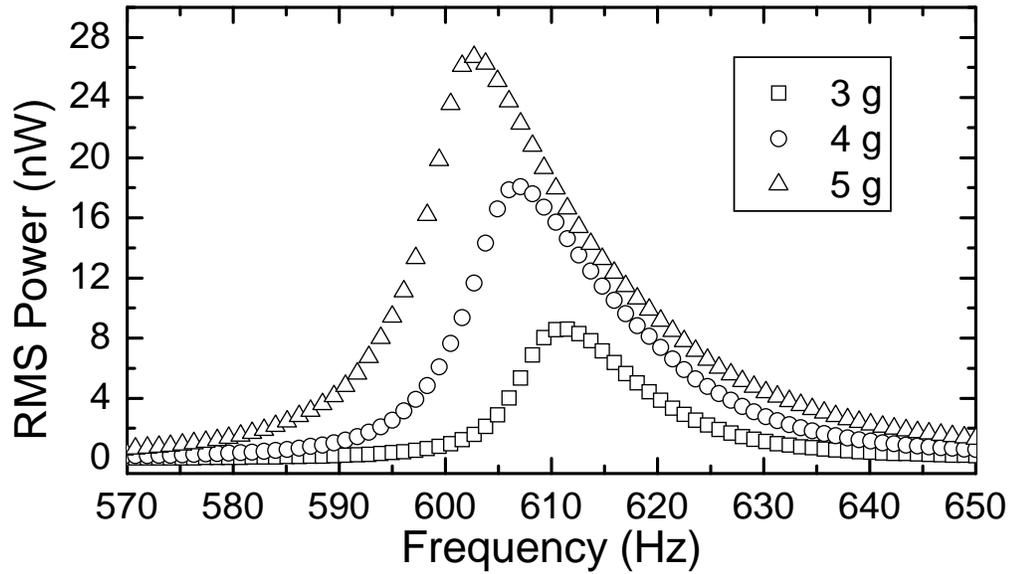


Figure 4.10. Frequency response of the moving plate measured in the electrical domain for different excitation accelerations.

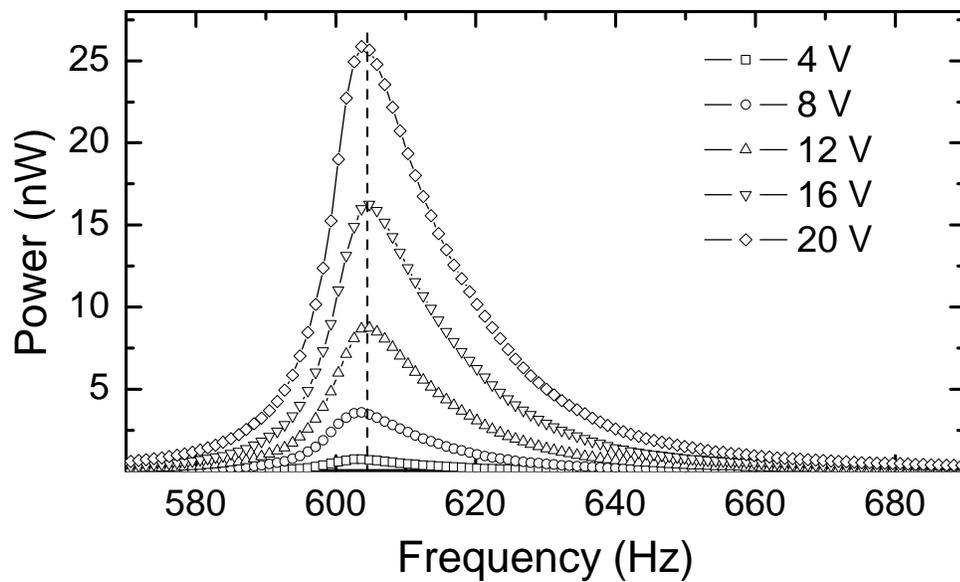


Figure 4.11. Frequency response of the MEMS device for different bias voltages.

To investigate the maximum output power from the MEMS device, the output characteristics under different biasing conditions were measured for different

accelerations. It can be seen from Figure 4.12 that the output power from the device can reach up to 186 nW from a single device at resonance excitation of 603 Hz.

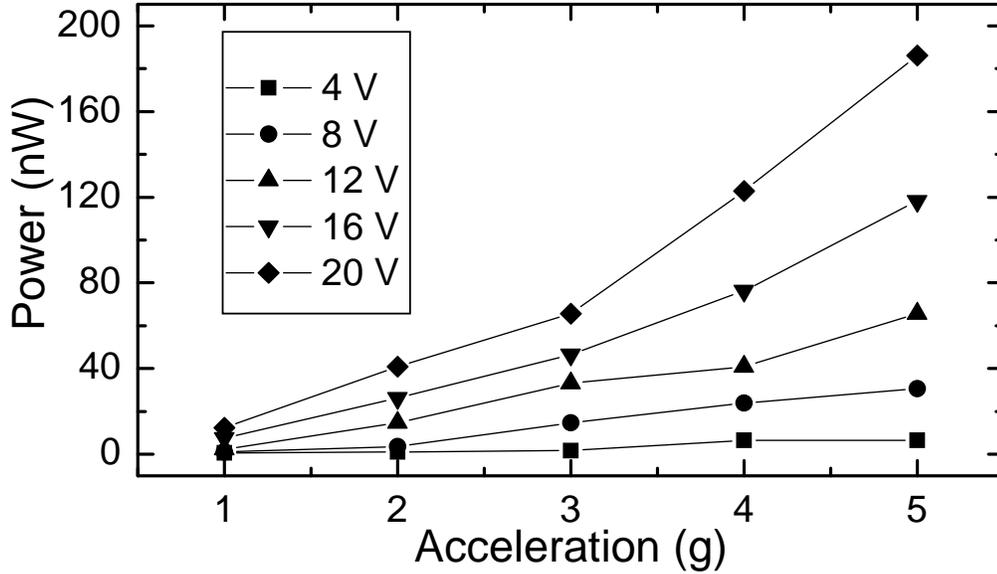


Figure 4.12. Output power for different excitation amplitudes at the resonance frequency

4.2.2 Broadband Low Frequency Electrostatic Device Characterization

Prior to assessing the fabricated devices, a simple electrical circuit was built to extract the output power generated by the MEMS power harvester. The power source performance was characterized by placing it on a controllable vibration shaker with adjustable vibration frequency and acceleration. The device was connected to a load resistor and the output voltage was measured across a load resistor connected in series with the MEMS capacitor. The voltage was monitored on a PC using LabVIEW and a data acquisition cable through an oscilloscope. The optimum value for the load resistor was determined experimentally. Several measurements were performed including the resonance frequency of the cantilever beams and the MEMS capacitor, the total harvested

power versus excitation acceleration, the total harvested power versus frequency for various acceleration values and bias voltage in order to determine the bandwidth.

An analog accelerometer was used to determine the acceleration at various vibration conditions, and thus calibrate the power harvesting device. The power harvesting devices were characterized by fixing the device on a rigid stage on the shaker (Figure 2.14). AC signals of different frequencies were applied to the shaker, and the resulting output voltages were measured across a load resistor connected in series with MEMS capacitor, using an oscilloscope, AC voltmeter and electrical spectrum analyzer. Initially, the optimized load resistor value was determined experimentally (Figure 4.13).

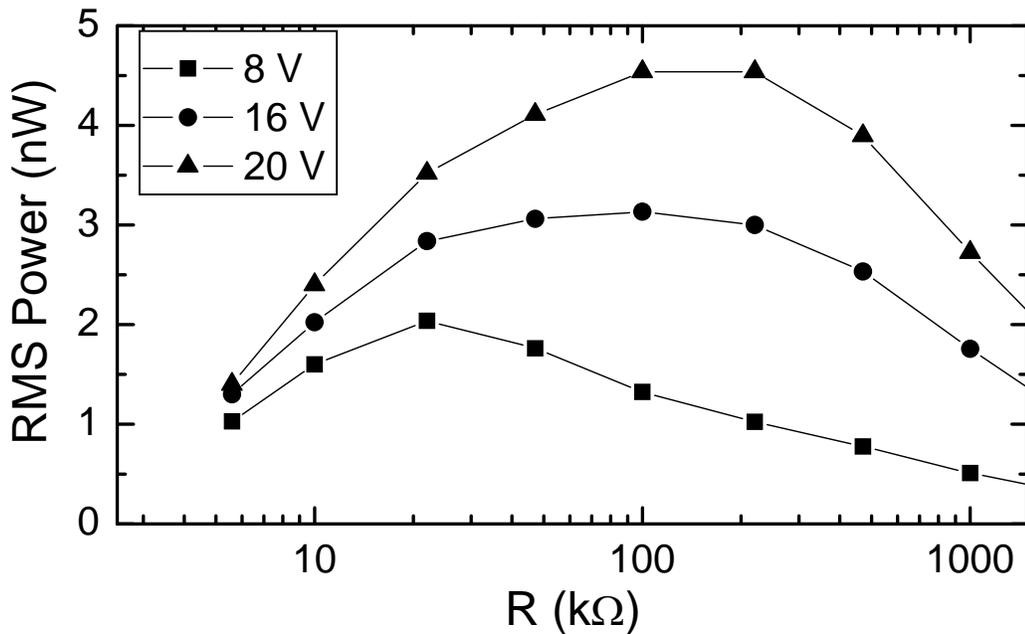


Figure 4.13. The RMS output power from the broadband electrostatic power harvester versus load resistor under 8V, 16V and 20V bias voltages.

The results showed that the best performance can be achieved with the load resistor values around 100 kΩ. To determine the resonance frequency of the high frequency

cantilever, the excitation frequency was swept from 100 to 1 kHz, and the generated output voltages were measured using a Multimeter.

The resonance frequency was observed around 605 Hz for low frequency excitation conditions (Figure 4.14). A typical time domain plot of the measured output AC voltage across a load resistor (100 k Ω) when the device was exposed to an ambient vibration at 25 Hz is shown in Figure 4.15 and Figure 4.16. The plot clearly demonstrates a nonlinear behavior with exponential decay at its resonance frequency of 605 Hz that can be calculated by $f = \frac{1}{T}$, and the peak to peak signal corresponds to a low frequency vibration of 25 Hz.

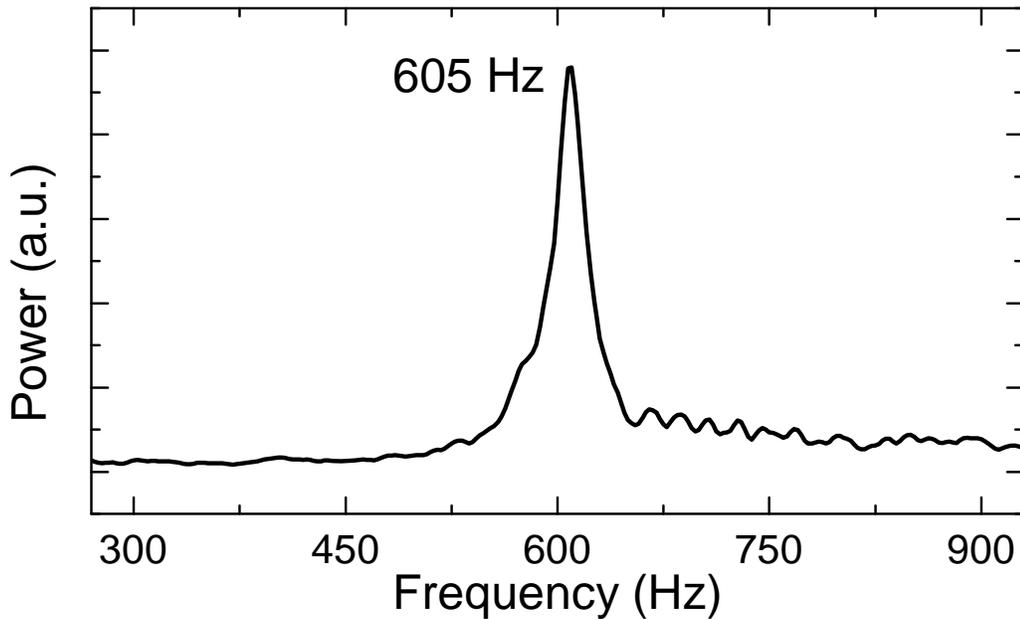


Figure 4.14. Typical spectra of the output power at the resonance frequency of the high frequency cantilever.

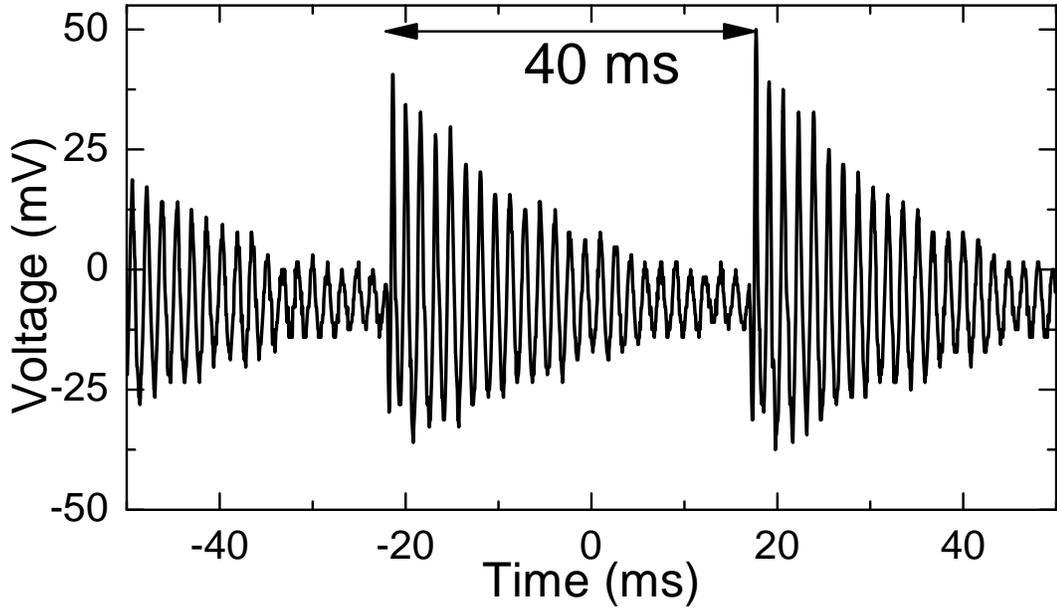


Figure 4.15. Time domain plot of the output voltage across the load resistor.

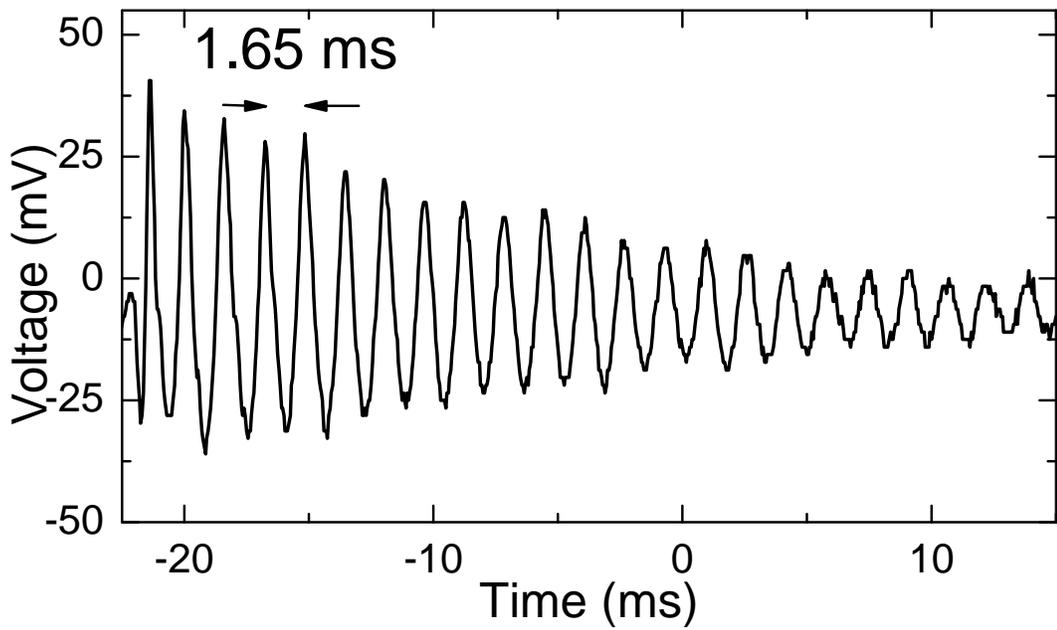


Figure 4.16. Time domain plot of the high frequency signal decay.

This clearly indicates the device ability for frequency up-conversion. To estimate the response bandwidth, the devices were first characterized by sweeping the excitation frequency from 5 Hz to 50 Hz with steps of 0.1 Hz under sinusoidal excitations with (0.5

g, 1 g and 2g) of constant acceleration, while the output voltage was measured for each excitation frequency across the load resistor. Initially, with a small acceleration of 1 g, only one impact cantilever with a resonance frequency of 18 Hz responded and made impacts with the high frequency cantilever up to 21 Hz. As the frequency increased further, both cantilevers started to make impact with the high frequency cantilever. As the frequency increased further, the low frequency cantilever stopped hammering the high frequency cantilever because it could not reach it anymore, and only the second cantilever beam kept hammering the high frequency cantilever beam up to 39 Hz. This has resulted in a wide bandwidth response from 15-35 Hz at 0.5 g. At higher acceleration of 1 g and 2g, the bandwidths were 13-39 Hz and 12-44 Hz, respectively, (Figure 4.17). The measured power across the load resistor achieved a maximum power of 55.5 nW, 96.2 nW and 137 nW under an excitation of 0.5 g, 1 g, and 2g respectively.

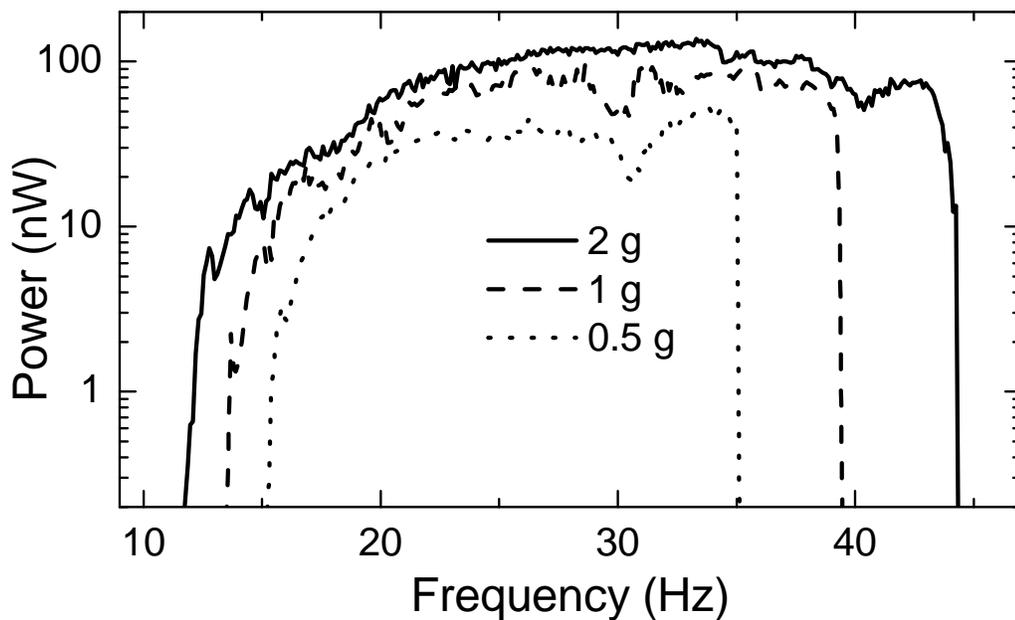


Figure 4.17. The RMS output power as a function of frequency for 0.5 g, 1 g and 2 g excitation accelerations.

Qualitatively speaking, the oscillator responded with a variable resonance frequency depending on the degree of impact. Therefore, the device had an optimal response over a much broader low frequency. It is noted that two impact masses were enough to cover the frequency range from 13 to 39 Hz at 1 g.

4.2.3 Broadband Low Frequency Electromagnetic Device Characterization

The power harvester was characterized by fixing the device and the magnet on a rigid stage on the shaker (Figure 2.25). An AC signal with different frequencies was applied to the shaker, and the resulting output voltages were measured using an oscilloscope, AC voltmeter and spectrum analyzer. First, we experimentally determined the optimized load resistor value (Figure 4.18). The results showed that the best performance can be achieved with the load resistor values around 22 ohms.

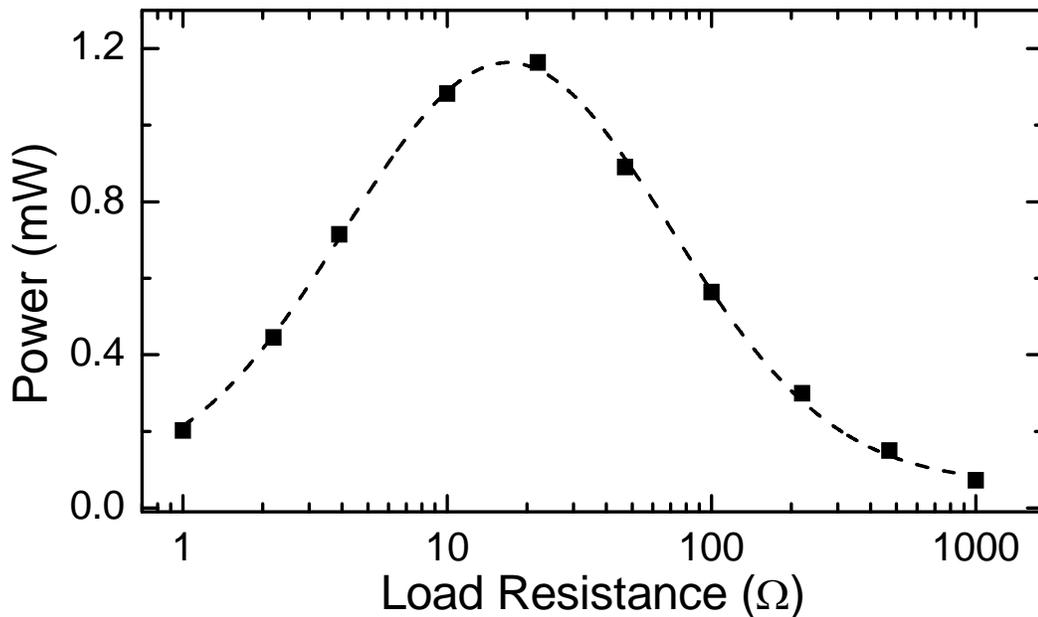


Figure 4.18. The RMS output power of the low frequency power harvesting device versus load resistance. Maximum power can be harvested from the device across a load resistor of 20 Ω .

To determine the resonance frequency of the high frequency cantilever, the excitation frequency was swept from 100 to 1 kHz, and the generated output voltages across the pick-up coil were measured by a multimeter. The resonance frequency was observed around 210 Hz for low frequency excitation conditions (Figure 4.19). Typical time domain plots of the measured output AC voltage across the pick-up coil (15 Ω) when the device was exposed to an ambient vibration at 15 Hz is shown in Figure 4.20. The plots show oscillations with decaying amplitude at its resonance frequency of 210 Hz, and the impacts at low frequency vibration of 15Hz are evidently noticeable. This clearly demonstrates the device ability for frequency up-conversion. The higher order modes are decaying much faster than the fundamental mode, and the fundamental mode survives between each impact. The frequency from the theoretical fit to the oscillations is also 210 Hz.

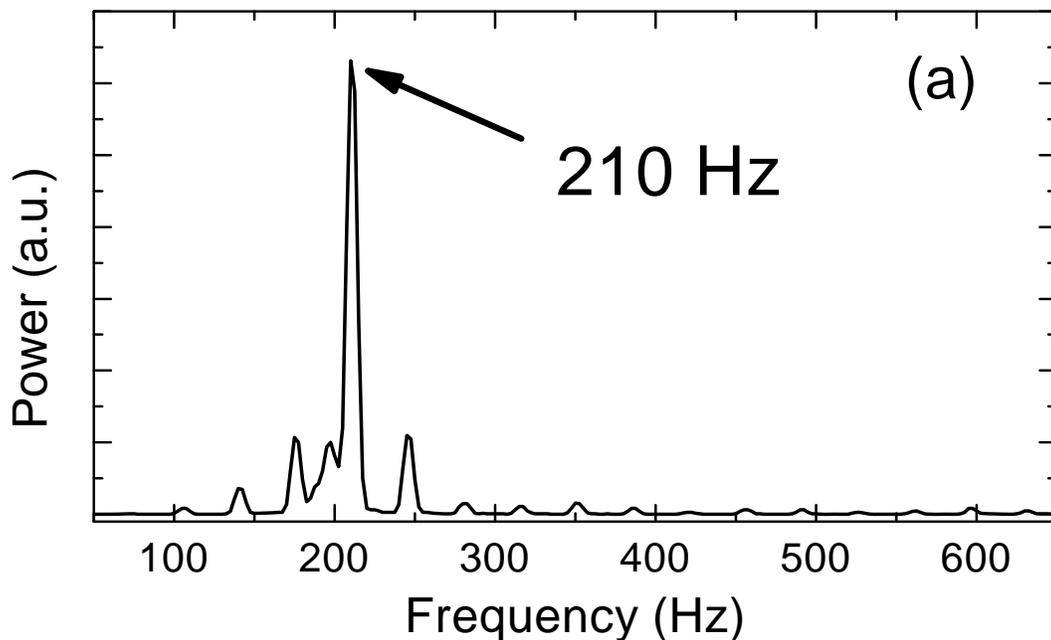


Figure 4.19. Typical spectra of the output power at the resonance frequency of the high frequency cantilever measured across the load resistor using a spectrum analyzer.

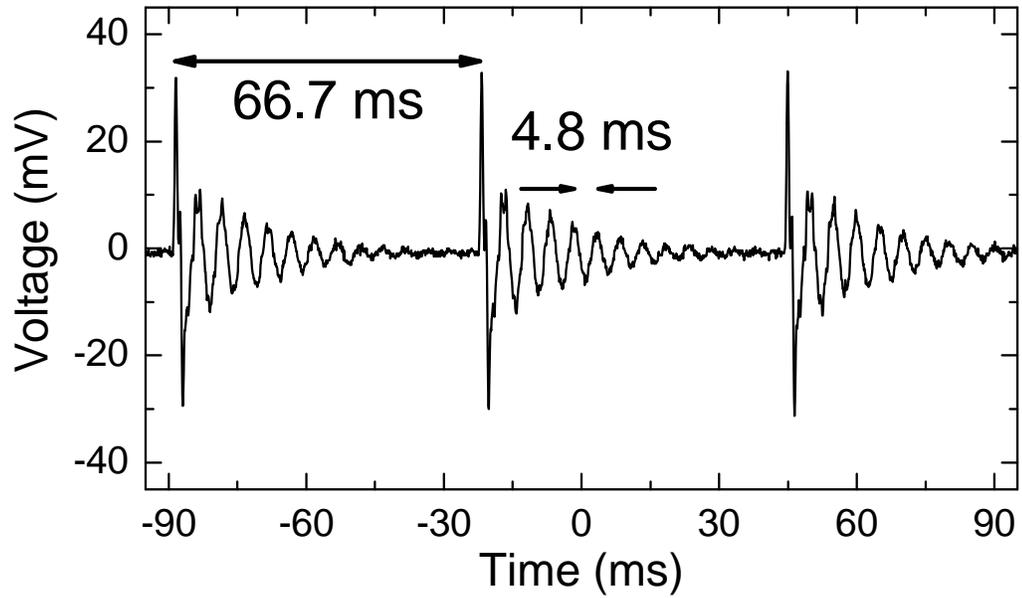


Figure 4.20. Typical spectra of output voltage in time domain measured across the load resistor using an oscilloscope. The time interval between impacts can be observed clearly while the high frequency signal is decaying between consecutive impacts.

To estimate the response bandwidth, the devices were first characterized by sweeping the excitation frequency from 5 Hz to 65 Hz with steps of 0.1 Hz under sinusoidal excitations with a constant acceleration (0.5 g, 1 g and 2g), across the load resistor (22Ω), connected in series with the pick-up coil, for each excitation frequency. At the beginning, with a small acceleration of 0.5 g, only one impact cantilever with a resonance frequency of 13 Hz responded and made impacts with the high frequency cantilever up to 22 Hz. When the frequency was increased further, both cantilevers started to make impact with the high frequency cantilever. When the frequency was increased further, the first cantilever stopped hammering the high frequency cantilever beam because it could not reach it anymore, and only the second cantilever beam kept hammering the high frequency cantilever beam up to 34 Hz. Again, as the frequency increased further, the third impact cantilever beam with resonance 40 Hz has started to

impact the high frequency cantilever. This has resulted in a wide bandwidth response from 12-58 Hz at 0.5 g. At higher acceleration of 1 g and 2g, the bandwidths were 11-62 Hz and 10-66 Hz, respectively, (Figure 4.21). The measured power across the load resistor achieved a maximum power of 5.5 μW , 17.5 μW and 65.8 μW at 29 Hz under an excitation of 0.5 g, 1 g, and 2g respectively. Qualitatively speaking, the oscillator responded with a variable resonance frequency depending on the degree of impact. Therefore, the device had an optimal response over a much broader low frequency. It is noted that three impact masses were enough to cover the frequency range from 11 to 62 Hz at 1 g. The EM power harvester gets its energy from the kinetic energy of the impact mass. Therefore, the impact mass must be comparable to the mass of the whole pick-up coil, otherwise the motion of the cantilever and the pick-up coil will be very small.

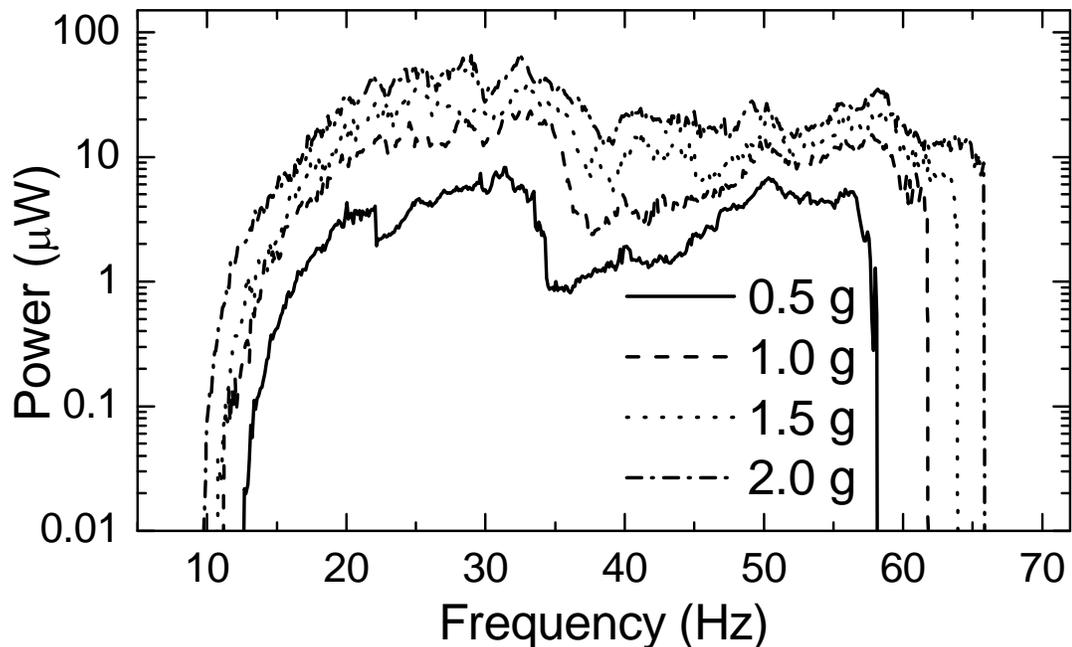


Figure 4.21. The RMS output power as a function of frequency for different excitation amplitude. The device covers the frequency range from 11 to 62 Hz at 1 g acceleration.

CHAPTER 5

CONCLUSION

A MEMS capacitor for power harvesting with $2 \times 2 \text{ mm}^2$ movable Ni plate has been designed, modeled, and fabricated. The device was fabricated on Si and glass substrates using surface micromachining and standard photolithography techniques. It was shown that a good control on the cavity size was possible with the control of growth rates of Ni. Devices were tested mechanically and electrically under different excitation and different biasing conditions. The resonant behavior of the moving plate was observed in both mechanical and electrical measurements. The structural and electrical properties of the modeled structure were analyzed using FEM. The structural method was used to determine the resonance frequency and squeeze film damping behaviors of the moving plate. The analysis of damping showed that vacuum packaging can improve the efficiency of the device. The equations of motion of the systems were numerically solved for dynamic behavior of the system under external sinusoidal excitations. The results indicated that nonlinear behavior due to mechanical interactions can enhance the device output.

The single cavity device was characterized in time and frequency domain under different excitation and biasing conditions. The operation frequency range of the Ni structure for thickness around $10\mu\text{m}$ was observed between 600 and 650 Hz. The load resistor, which is connected in series to the power harvester to measure the power, was optimized at constant external acceleration. An optimum load resistor value of 100 k Ω

that achieve maximum amount of output power was determined. The device was tested at different bias voltages ranging from 4V to 20V. Extensive measurements were performed under different external accelerations ranging from 0.5 g to 5 g by applying different AC voltages to the mechanical shaker. The results showed that, resonance frequency of the movable Ni plate shifted towards lower frequencies at larger acceleration due to softening effect of the electrostatic force. At resonance frequency, the device is able to generate 186 nW of maximum power across a 100 k Ω resistor at 5 g acceleration under 20V DC bias.

The MEMS device was shown to be utilized for low frequency applications with broadband response. Proposed macro-scale system has been built and tested for a frequency range of 10-50 Hz. The device can operate from 13 to 39 Hz at 1 g and 12 Hz to 44 Hz under the excitation of 2g while the resonance frequency of the MEMS device is at 605 Hz. Maximum power 96.2 nW and 137 nW was measured across the load resistor under an excitation of 1 g, and 2g respectively. With further enhancements in design parameters, it is possible improve the performance of the proposed electrostatic power harvesting device. It is also possible to miniaturize the device into micro scale and tune the frequency for a specific application

Multi impact frequency conversation and broadband response effect was shown in electromagnetic power harvesting devices. A macro scale prototype of an electromagnetic power harvester was studied with three impact masses and modeled for low frequency vibrations. The device is able to transfer the energy from low frequency oscillations from a broad range into a high frequency oscillation and then the oscillations

at high frequency into electrical energy by electromagnetic induction using a magnet on the base and a pick-up coil fixed on the high frequency cantilever beam. In addition the device is not restricted to narrow bandwidth because of the nonlinearity caused by the impacts. The electromagnetic power harvester with three impact masses has wide bandwidth response from 11-62 Hz at 1 g and 10-66 Hz at 2 g acceleration. A maximum output power of 23.5 μW and 65.8 μW can be harvested at 1 g and 2 g acceleration, respectively, across an optimum load resistor of 22 Ω .

REFERENCES

- [1] Y. B. Jeon, R. Sood, J. Jeong, and S. G. Kim, "MEMS power generator with transverse mode thin film PZT," *Sens. Actuators A, Phys.*, vol. 122, no. 1, pp. 16-22, 2005.
- [2] L-C J. Blystad, E. Halvorsen, S. Husa, "Piezoelectric MEMS Energy Harvesting Systems Driven by Harmonic and Random Vibrations," *IEEE T-UFFC*, vol. 57, pp. 908-919, 2010.
- [3] S. P. Beeby, R. N. Torah, M. J. Tudor, P. Glynne-Jones, T. O'Donnell, C. R. Saha, and S. Roy, "A micro electromagnetic generator for vibration energy harvesting," *J. Micromech. Microeng.*, vol. 17, no. 7, p. 1257, 2007.
- [4] C. Serre, A. P. Rodriguez, N. Fondevilla, J. R. Morante, J. Montserrat, J. Esteve, "Vibrational energy scavenging with Si technology electromagnetic inertial microgenerators" *Microsyst. Technol.*, vol. 13 pp. 1655-1661, 2007.
- [5] S. Meninger, J. O. Mur-Miranda, R. Amirtharajah, A. Chandrakasan, and J. H. Lang, "Vibration-to-electric energy conversion," *Very Large Scale Integration (VLSI) Systems, IEEE Transactions on*, vol. 9, no. 1, pp. 64-76, 2001.
- [6] G. Despesse and S. O. Lution, "Innovative Structure For Mechanical Energy Scavenging," in *Proc. Transducers & Eurosensors*, 2007, pp. 895-898.
- [7] P. D. Mitcheson, E. K. Reilly, T. Toh, P. K. Wright, and E. M. Yeatman, "Performance limits of the three MEMS inertial energy generator transduction types" *J. Micromech. Microeng.*, vol. 17(9), p. S211, 2007.
- [8] R. J. M. Vullers, R. van Schaijk, I. Doms, C. Van Hoof, and R. Mertens, "Micropower energy harvesting," *Solid-State Electron.*, vol. 53, no. 7, pp. 684-693, 2009.
- [9] S. Roundy, "On the effectiveness of vibration-based energy harvesting," *J. Intell. Mater. Syst. Struct.*, vol. 16, no. 10, pp 809-823, 2005.
- [10] E. M. Yeatman, P. D. Mitcheson, and A. S. Holmes, "Micro-engineered devices for motion energy harvesting," in *Proc. IEEE/IEDM*, pp.375-378, 2007.
- [11] H. Liu, C. J. Tay, C. Quan, T. Kobayashi, and C. Lee, "Piezoelectric MEMS energy harvester for low-frequency vibrations with wideband operation range and steadily increased output power," *J. Microelectromech. Syst.*, vol. 20, no. 5, pp. 1131-1142, 2011.
- [12] A. Massaro, S. De Guido, I. Ingrosso, R. Cingolani, M. De Vittorio, M. Cori, A. Bertacchini, L. Larcher, and A. Passaseo, "Freestanding piezoelectric rings for high efficiency energy harvesting at low frequency," *Appl. Phys. Lett.*, vol. 98, no. 5, 2011.

- [13] S. Xu, K. D. T. Ngo, T. Nishida, G. B. Chung, and A. Sharma, "Low frequency pulsed resonant converter for energy harvesting," *IEEE Trans. Power Electron.*, vol. 22, no. 1, pp. 63-68, 2007.
- [14] Y. C. Shu and I. C. Lien, "Efficiency of energy conversion for a piezoelectric power harvesting system," *J. Micromech. Microeng.*, vol. 16, no. 11, pp. 2429-2438, Sep. 2006.
- [15] C. S. Park, D. Avirovik, M. I. Bichurin, V. M. Petrov, and S. Priya, "Tunable magnetoelectric response of dimensionally gradient laminate composites," *Appl. Phys. Lett.*, vol 100, no. 21, 2012.
- [16] L. Chen, P. Li; Y. M. Wen, and D. Wang, "Magnetoelectric transducer employing piezoelectric ceramic/ferromagnetic alloy/high-permeability FeCuNbSiB composite," *IEEE Trans. Magn.*, vol. 47, no. 10, 2011.
- [17] D. A. Wang, C. Y. Chiu, and H. T. Pham, "Electromagnetic energy harvesting from vibrations induced by Kármán vortex street," *Mechatronics*, vol. 22, no. 6, pp. 746-756, 2012.
- [18] L. Tang and Y. Yang, "A nonlinear piezoelectric energy harvester with magnetic oscillator," *Appl. Phys. Lett.*, vol. 101, no. 9, 2012.
- [19] R. Tashiro, N. Kabei, K. Katayama, Y. Ishizuka, F. Tsuboi, and K. Tsuchiya, "Development of an electrostatic generator that harnesses the motion of a living body: (use of a resonant phenomenon)," *JSME international journal. Series C, Mechanical systems, machine elements and manufacturing*, vol. 43, no. 4, pp. 916-922, 2000.
- [20] P. Miao, A. S. Holmes, E. M. Yeatman, T. C. Green, and P. D. Mitcheson, "Micro-machined variable capacitors for power generation," in *Proc. Electrostatics*, vol. 3, pp. 53-58, 2003.
- [21] C. H. Haas and M. Kraft, "Modelling and analysis of a MEMS approach to dc voltage step-up conversion," *J. Micromech. Microeng.*, vol. 14, no. 9, p. S114, 2004.
- [22] P. Lim et al., "Design of a novel highly capacitive MEMS-based vibration to electricity energy converter with suspended in-plane overlap technology," in *Proc. of APCOT'06, Singapore*, 2006.
- [23] A. M. Paracha, P. Basset, P. C. Lim, F. Marty, and T. Bourouina, "A bulk silicon-based vibration-to-electric energy converter using an in-plane overlap plate (IPOP) mechanism," in *Proc. PowerMEMS*, pp. 169-172, 2006.
- [24] A. M. Paracha, P. Basset, D. Galayko, F. Marty, and T. Bourouina, "A Silicon MEMS DC/DC Converter for autonomous vibration-to-electrical-energy scavenger," *Electron Device Letters, IEEE*, vol. 30, no. 5, pp. 481-483, 2009.

- [25] B. C. Yen and J. H. Lang, "A variable-capacitance vibration-to-electric energy harvester," *Circuits and Systems I: Regular Papers, IEEE Transactions on*, vol. 53, no. 2, pp. 288-295, 2006
- [26] B. Hoffmann, B. Folkmer, and Y. Manoli, "Fabrication, characterization and modelling of electrostatic micro-generators," *J. Micromech. Microeng.*, vol. 19, no. 9, 2009.
- [27] C. P. Le, E. Halvorsen, O. Søråsen, E. M. Yeatman, "Wideband excitation of an electrostatic vibration energy harvester with power-extracting end-stops" *Smart Mater. Struct.*, vol. 22 no. 7, 2013.
- [28] P. Miao, P. D. Mitcheson, A. S. Holmes, E. M. Yeatman, T. C. Green, and B. H. Stark, "MEMS inertial power generators for biomedical applications," *Microsyst. Technol.*, vol. 12, no. 10-11, pp. 1079-1083, 2006.
- [29] T. Takahashi, M. Suzuki, T. Nishida, Y. Yoshikawa, S. Aoyagi, S. "Vertical capacitive energy harvester positively using contact between proof mass and electret plate-Stiffness matching by spring support of plate and stiction prevention by stopper mechanism," *Micro Electro Mechanical Systems (MEMS), 28th IEEE International Conference on* (pp. 1145-1148). IEEE. 2015
- [30] P. D. Mitcheson, P. Miao, B. H. Stark, E. M. Yeatman, A. S. Holmes, and T. C. Green, "MEMS electrostatic micropower generator for low frequency operation," *Sens. Actuators A, Phys.*, vol. 115, no. 2-3, pp. 523-529. 2004.
- [31] K. Matsumoto, K. Saruwatari, and Y. Suzuki, "Vibration-powered battery-less sensor node using MEMS electret generator," in *Proc. PowerMEMS*, pp 134-137, 2011.
- [32] S. D. Nguyen and E. Halvorsen, "Nonlinear springs for bandwidth-tolerant vibration energy harvesting," *J. Microelectromech. Syst.*, vol. 20, no. 6, pp. 1225-1227, 2011.
- [33] L. G. W. Tvedt, D. S. Nguyen, and E. Halvorsen, "Nonlinear behavior of an electrostatic energy harvester under wide-and narrowband excitation," *J. Microelectromech. Syst.*, vol. 19, no. 2, pp. 305-316, 2010.
- [34] E. O. Torres and G. A. Rincón-Mora, "Electrostatic energy-harvesting and battery-charging CMOS system prototype," *IEEE Trans. Circuits Syst.*, vol. 56, no. 9, pp. 1938-1948, 2009.
- [35] P. Basset, D. Galayko, A. M. Paracha, F. Marty, A. Dudka, and T. Bourouina, "A batch-fabricated and electret-free silicon electrostatic vibration energy harvester," *J. Micromech. Microeng.*, vol. 19, no. 11, 2009.
- [36] Y. Minakawa and Y. Suzuki, "Low-resonant-frequency MEMS electret energy harvester with x-shaped high-aspect-ratio parylene spring," *Proc. PowerMEMS*, pp. 133-136, 2012.

- [37] R. Chen and Y. Suzuki, "Metal-on-nothing electrodes for reducing parasitic capacitance in electret energy harvesting devices," *Proc. PowerMEMS*, pp. 121-124, 2012.
- [38] G. Despesse, J. J. Chaillout, T. Jager, F. Cardot, and A. Hoogerwerf, "Innovative structure for mechanical energy scavenging," in *Transducers*, pp. 895-898, 2007.
- [39] E. O. Torres and G. A. Rincón-Mora, "Electrostatic energy-harvesting and battery-charging CMOS system prototype," *IEEE Trans. Circuits Syst.*, vol. 56, no. 9, pp. 1938-1948, 2009.
- [40] T. Von Buren, P. D. Mitcheson, T. C. Green, E. M. Yeatman, A. S. Holmes, and G. Troster, "Optimization of inertial micropower generators for human walking motion," *IEEE Sensors J.*, vol. 6, pp. 28-38, 2006.
- [41] D. Zhu, M. J. Tudor, and S. P. Beeby, "Strategies for increasing the operating frequency range of vibration energy harvesters: a review," *Meas. Sci. Technol.*, vol. 21, no. 2, pp. 1-29, 2010.
- [42] S. Roundy and Y. Zhang, "Toward self-tuning adaptive vibration based micro-generators," *Proc. SPIE*, pp. 373-384, 2005.
- [43] V. R. Challa, M. G. Prasad, Y. Shi, and F. T. Fisher, "A vibration energy harvesting device with bidirectional resonance frequency tunability," *Smart Mater. Struct.*, vol. 17, no. 1, 2008.
- [44] G. Piazza, R. Abdolvand, G. K. Ho, and F. Ayazi, "Voltage-tunable piezoelectrically transduced single-crystal silicon micromechanical resonators," *Sens. Actuators A, Phys.*, vol. 111, pp. 71-78, 2004.
- [45] D. Scheibner, J. Mehner, D. Reuter, U. Kotarsky, T. Gessner, and W. Dötzel, "A spectral vibration detection system based on tunable micromechanical resonators," *Sens. Actuators A, Phys.*, vol. 123, pp. 63-72, 2005.
- [46] K. B. Lee, L. Lin, and Y. H. Cho, "A closed-form approach for frequency tunable comb resonators with curved finger contour," *Sens. Actuators A, Phys.*, vol. 141, pp. 523-529, 2008.
- [47] I. Sari, T. Balkan, H. Kulah. "A wideband electromagnetic micro power generator for wireless microsystems," in *Transducers*, pp 275-278, 2007.
- [48] S. M. Shahruz, "Design of mechanical band-pass filters for energy scavenging," *J. Sound Vib.*, vol. 292, pp. 3-5, 2006.
- [49] R. Ramlan, M. J. Brennan, B. R. Mace, and I. Kovacic, "Potential benefits of a non-linear stiffness in an energy harvesting device," *Nonlinear Dyn.*, vol.59, pp. 545-58, 2010.

- [50] F. Arrieta, P. Hagedorn, A. Erturk, and D. J. Inman, "A piezoelectric bistable plate for nonlinear broadband energy harvester," *Appl. Phys. Lett.*, vol. 97, no. 10, 2010.
- [51] F. Cottone, H. Vocca, and L. Gammaitoni, "Nonlinear energy harvesting," *Phys. Rev. Lett.*, vol. 102, no. 8, 2009.
- [52] B. Ando, S. Baglio, C. Trigona, N. Dumas, L. Latorre, and P. Nouet, "Nonlinear mechanism in MEMS devices for energy harvesting application," *J. Micromech. Microeng.*, vol. 20, no.12, 2010.
- [53] G. H. Feng and J. C. Hung, "Optimal FOM designed piezoelectric microgenerator with energy harvesting in a wide vibration bandwidth" *Proc. 2nd IEEE Int. Conf. on Nano/Micro Engineered and Molecular Systems*, pp 511-4, 2007.
- [54] D. Spreemann, B. Folkmer, D. Maurath, Y. Manoli "Tunable transducer for low frequency vibrational energy scavenging" in *Proc. EurosensorsXX*, 2006.
- [55] D.S. Nguyen, E. Halvorsen, G. U. Jensen, and A. Vogl, "Fabrication and characterization of a wideband MEMS energy harvester utilizing nonlinear springs," *J. Micromech. Microeng.*, vol. 20, no. 12, 2010.
- [56] B. P. Mann and N. D. Sims, "On the performance and resonant frequency of electromagnetic induction energy harvesters," *J. Sound Vib.* vol. 329, pp. 1348-1361, 2010.
- [57] S. C. Stanton, C. C. McGehee, and B. P. Mann, "Nonlinear dynamics for broadband energy harvesting: investigation of a bistable piezoelectric inertial generator," *Physica D: Nonlinear Phenomena*, vol. 239, pp. 640-653, 2010.
- [58] S. D. Nguyen, E. Halvorsen, and I. Paprotny, "Bistable springs for wideband microelectromechanical energy harvesters," *Appl. Phys. Lett.*, vol. 102, 2013.
- [59] B. Marinkovic and H. Koser, "Smart Sand—a wide bandwidth vibration energy harvesting platform," *Appl. Phys. Lett.*, vol. 94, 2009.
- [60] M. Marzencki, M. Defosseux, and S. Basrour, "MEMS vibration energy harvesting devices with passive resonance frequency adaptation capability," *J. Microelectromech. Syst.*, vol.18, pp. 1444-53, 2010.
- [61] S. Moss, A. Barry, I. Powlesland, S. Galea, and G. P. Carman, "A low profile vibro-impacting energy harvester with symmetrical stops," *Appl. Phys. Lett.*, vol. 97, no. 23, 2010.
- [62] K. Ashraf, M. H. Md Khir, J. O. Dennis, and Z. Baharudin, "A wideband, frequency up-converting bounded vibration energy harvester for a low frequency environment," *Smart Mater. Struct.*, vol. 22, no. 2, 2013.

- [63] B. P. Mann and N. D. Sims, "Energy harvesting from the nonlinear oscillations of magnetic levitation," *J. Sound Vib.*, vol. 319, pp. 515-530, 2009.
- [64] H. Liu, C. Lee, T. Kobayashi, C. J. Tay, and C. Quan, "Investigation of a MEMS piezoelectric energy harvester system with a mechanism introduced by mechanical stoppers," *Smart Mater. Struct.*, vol. 21, no. 3, 2012.
- [65] M. Soliman, E. F. El-Saadany, E. M. Abdel-Rahman, and R. R. Mansour, "A wideband vibration-based energy harvester," *J. Micromech. Microeng.*, vol.18, no. 11, 2008
- [66] B. J. Bowers and D. P. Arnold, "Spherical rolling magnet generators for passive energy harvesting from human motion," *J. Micromech. Microeng.*, vol.19, no. 9, 2009.
- [67] M. E. Kiziroglou, C. He, and E. M. Yeatman, "Flexible substrate electrostatic energy harvester," *Electron. Lett.*, vol. 46, No 2, January, 2010.
- [68] I. Kuehne, D. Marinkovic, G. Eckstein, and H. Seidel, "A new approach for MEMS power generation based on a piezoelectric diaphragm," *Sens. Actuators A, Phys.*, vol. 142, no. 1, 2008.
- [69] G. Murillo, G. Abadal, F. Torres, J. L. Lopez, J. Giner, A. Uranga, and N. Barniol, "Harvester-on-chip: design of a proof of concept prototype," *Microelectron. Eng.*, vol. 86, pp. 1183-6, 2009.
- [70] M. Umeda, K. Nakamura, and S. Ueha, "Analysis of the transformation of mechanical impact energy to electric energy using piezoelectric vibrator," *J. Appl. Phys.*, vol. 35, pp. 3267-73, 1996.
- [71] M. Renaud, P. Fiorini1, R. van Schaijk, and C. van Hoof, "Harvesting energy from the motion of human limbs: the design and analysis of an impact-based piezoelectric generator," *Smart Mater. Struct.*, vol. 18, no. 3, 2009.
- [72] L. Gu, "Low-frequency piezoelectric energy harvesting prototype suitable for the MEMS implementation," *Microelectronics Journal*, vol. 42, pp. 277-282, 2011.
- [73] L. Gu and C. Livermore, "Impact-driven, frequency up-converting coupled vibration energy harvesting device for low frequency operation," *Smart Mater. Struct.*, vol. 20, no. 4, 2011.
- [74] Y. Zhang and C. S. Cai, "A retrofitted energy harvester for low frequency vibrations," *Smart Mater. Struct.*, vol. 21, no. 7, 2012.
- [75] G. Manla, N. M. White, and J. Tudor, "Harvesting energy from vehicle wheels," in *Transducers*, pp. 1389-1392, 2009.
- [76] D. G. Lee, G. P. Carman, D. Murphy, and C. Schulenburg, "Novel micro vibration energy harvesting device using frequency up conversion," *IEEE Transducer*, pp. 871-874, 2007.

- [77] H. Liu, C. J. Tay, C. Quan, T. Kobayashi, and C. Lee, "A scrape-through piezoelectric MEMS energy harvester with frequency broadband and up-conversion behaviors," *Microsyst. Technol.*, vol. 17, pp. 1747-1754, 2011.
- [78] S. M. Jung and K. S. Yun, "Energy-harvesting device with mechanical frequency-up conversion mechanism for increased power efficiency and wideband operation," *Appl. Phys. Lett.*, vol. 96, no. 11, 2010.
- [79] H. Kulah and K. Najafi, "Energy scavenging from low-frequency vibrations by using frequency up-conversion for wireless sensor applications," *IEEE Sensor J.*, vol. 8, no. 3, 2008.
- [80] Ö. Zorlu, E. T. Topal, and H. Kùlah, "A vibration-based electromagnetic energy harvester using mechanical frequency up-conversion method," *IEEE Sensor J.*, vol. 11, no. 2, 2011.
- [81] D.-M. Fang, X.-M. Jing, P.-H. Wang, Y. Zhou, and X.-L. Zhao, "Fabrication and dynamic analysis of the electrostatically actuated MEMS variable capacitor," *Microsyst. Technol.*, vol. 14, no. 3, pp. 397-402, 2008.
- [82] M. N. O. Sadiku, *Elements of Electromagnetics*, Oxford University Press, 2006.
- [83] N. S. Yuksek, Z. C. Feng, and M. Almasri. "Broadband electromagnetic power harvester from vibrations via frequency conversion by impact oscillations," *Appl. Phys. Lett.*, vol. 105.11 (2014): 113902.
- [84] <http://www.aulmut.com/technologies-2/plasma-processes/sputtering>
- [85] D. M. G. Leite, A. L. J. Pereira, L. da Silva, and J. H. Silva, "Nanocrystalline GaN and GaN: H films grown by RF-magnetron sputtering," *Brazil. J. Phys.*, vol. 36, no. 3B, pp. 978-981, 2006.
- [86] AZ® P4000 Thick Film Photoresist Datasheet
- [87] M.-H. Bao, *Analysis and design principles of MEMS devices*, Elsevier, 2005.
- [88] J. J. Blech, "On isothermal squeeze films," *Journal of Lubrication Technology*, vol. 105, p. 615, 1983.
- [89] A. K. Pandey, R. Pratap, and F. S. Chau, "Analytical solution of the modified Reynolds equation for squeeze film damping in perforated MEMS structures," *Sens. Actuators A, Phys.*, vol. 135, no. 2, pp. 839-848, 2007.
- [90] M. Hopcroft, T. Kramer, G. Kim, K. Takashima, Y. Higo, D. Moore, and J. Brugger, "Micromechanical testing of SU-8 cantilevers," *Fatigue Fracture Eng. Mater. Struct.*, vol. 28, no. 8, pp. 735-742, 2004.

- [91] L. Dellmann, S. Roth, C. Beuret, G.-A. Racine, H. Lorenz, M. Despont, P. Renaud, P. Vettiger, N.F. de Rooij, "Fabrication process of high aspect ratio elastic structures for piezoelectric motor applications," in *Transducers*, pp. 641-644, 1997.
- [92] S. Keller, D. Haefliger and A. Boisen, "Fabrication of thin SU-8 cantilevers: initial bending, release and time stability," *J. Micromech. Microeng.*, vol. 20, 045024, 2010.
- [93] M. Ohnmacht, V. Seidemann, S. Buttgenbach, "Microcoils and microrelays - an optimized multilayer fabrication process" *Sens. Actuators A, Phys.*, vol. 83, pp. 124-129, 2000.
- [94] C. H. Ahn, Y. J. Kim, and M. G. Allen, "A planar variable reluctance magnetic micromotor with fully integrated stator and coils," *J. Microelectromech. Sys.*, vol. 2, no. 4, p 165-73, 1993.
- [95] A. S. Holmes, H. Guodong, K. R. Pullen, "Axial-flux permanent magnet machines for micropower generation," *J. Microelectromech. Sys.*, vol. 14, no. 1, pp. 54-62, 2005.
- [96] F. Herrault, S. Yorish, T. M. Crittenden, C.-H. Ji, and M. G. Allen, "Parylene-Insulated Ultradense Microfabricated Coils," *J. Microelectromech. Sys.*, vol. 19, No. 6, 2010.

LIST OF PUBLICATIONS

Journals:

N.S. Yuksek, J.X. Zhu, Z.C. Feng, M Almasri, "Investigation of Broadband Electromagnetic Power Harvesters"

N.S. Yuksek, J.X. Zhu, Z.C. Feng, M Almasri, "Broadband Electrostatic Power Harvesting by MEMS capacitors"

S.G. Dastider, S Barizuddin, **N.S. Yuksek**, M Dweik, M Almasri, "Efficient and rapid detection of Salmonella using microfluidic impedance based sensing," Journal of Sensors (2015).

J.X. Zhu, J Lin, **N.S. Yuksek**, M Almasri, Z.C. Feng, "Dynamic phenomena and analysis of MEMS capacitive power harvester subjected to low-frequency excitations," Nonlinear Dynamics, 79.1 (2014): 673-688

N.S. Yuksek, ZC Feng, M Almasri, "Broadband electromagnetic power harvester from vibrations via frequency conversion by impact oscillations," Appl. Phys. Lett. 105, 113902 (2014)

Conferences:

J.X. Zhu, Z.C. Feng, J. Lin, **N.S. Yuksek** and M. Almasri, "Dynamic Study of MEMS Variable Capacitive Device for Power Harvesting," Proc. ASME International IDETC and CIE, 2012.

NS Yuksek, J Lin, Z Feng, M Sonje, J Zhu, M Almasri, "MEMS capacitors with dual cavity for power harvesting, SPIE Defense Security and Sensing" 23-27 April 2012 Baltimore, Maryland

J. Lin, J. X. Zhu, M. Sonje, **N.S. Yuksek**, Z. C. Feng, and M. Almasri, "Multi-cavities MEMS Capacitive Plates for Power Harvesting," Proc. PowerMEMS, Seoul, Korean, Nov. 2011.

J. Lin, M. Sonje, S. Nanduri, **N.S. Yuksek**, Z. C. Feng, and M. Almasri, "Fabrication and Modeling Analysis of the MEMS Capacitive Plates with Large Dynamic Range for Voltage Conversion and Power Harvesting," Proc. NSF Engineering Research and Innovation Conference, Atlanta, Georgia, Jan. 2011.

Patent disclosures:

N.S Yuksek, M. Almasri, “Method and Electromagnetic Inertial Micro Device for generating Electrical Power from Low Frequency Oscillations,” U.S. Patent disclosure, in process, 2013.

J. Lin, **N.S Yuksek**, Z. Feng, M. Almasri, “MEMS Multi-Cavity Capacitive Power Harvester,” U.S. Patent disclosure, in process, 2013.

VITA

Nuh Sadi Yuksek was born in Ankara, Turkey. He received the B.S. and M.S. degrees in department of physics at Middle East Technical University (METU) in 2002 and 2004, respectively. He has got an MS degree in Electrical Engineering and Computer Science department at University of California Irvine (UCI) in 2009. He received his Ph.D. degree in Electrical and Computer Engineering at the University of Missouri (MU), Columbia, MO, in 2015.

Since 2010, he has been a graduate research assistant in the Department of Electrical and Computer Engineering at the University of Missouri, Columbia working on his doctoral research focusing on electrostatic and electromagnetic MEMS energy harvesting His current research interests include microfabrication, surface micro-machining, Power MEMS, Bio-MEMS, IR Sensors, semiconductors, optics and photonics.